MULTIPARTICLE PRODUCTIONS IN PROTON–NUCLEUS COLLISIONS AT 360 GEV/C

Thesis by
Yoshihisa Iga

In Partial Fulfillment of
the Requirements for
the Degree of Doctor of Science

Tokyo Metropolitan University
Tokyo, Japan

(1986)

ACKNOWLEDGEMENTS

I would like to take this opportunity to thank the numerous people who have contributed to the realisation of this thesis.

This work could not have been performed without the work of the members of NA23 collaboration and of the staff participating in the European Hybrid Spectrometer Project. Also I would like to acknowledge the heroic efforts by Drs. L.Montanet, P.Porth and all members of our collaboration.

I would particularly like to express my gratitude to my supervisor Professor T.Yamagata for his advice and encouragement throughout my time of graduate study. I am very grateful to Drs. R.Hamatsu and H.Sumiyoshi for their frequent and fruitful discussion and support in this work. I would like to express my appreciation to Prof. I.Kita and Drs. S.Kitamura and N.Oshima for their valuable advice and encouragement.

I am indebted to Mr. S.Yamazaki and Drs. R.Hamatsu and H.Sumiyoshi for the development of the Monte Carlo event generator MCMHA. I am grateful to members of Tokyo University of Agriculture and Technology for the usage of the computer VAX-11/780.

Finally, I would like to thank my parents for their long support and encouragement.

ABSTRACT

The multiparticle production in 360 GeV/c proton-nucleus collisions has experimentally been studied. The data used in the analysis were obtained from the exposure of the hydrogen Rapid Cycling Bubble Chamber (RCBC) installed in the European Hybrid Spectrometer (EHS) to a 360 GeV/c proton beam from CERN-SPS, where small aluminium and gold pieces were mounted in the RCBC. We selected 47 events as proton-aluminium nucleus (p-Al) interactions and 192 events as proton-gold nucleus (p-Au) ones from 195000 triggers, and these 239 events in total were analysed in this work.

We found 17.7±1.5 as the mean total charged multiplicity of p-Al and 28.2±1.3 for p-Au collisions, respectively. Also the mean gray multiplicity was found to be 1.9±0.5 for p-Al and 4.6±0.4 for p-Au collisions, respectively. Total and shower multiplicity distributions were compared with the KNO scaling distributions in order to check this scaling model in proton-nucleus interactions and we found that the KNO distribution is in agreement with that of p-Al collisions but does not agree with that of p-Au collisions well.

The number of deuterons produced per event was found to be 0.17±0.10 for p-Al and 0.47±0.07 for p-Au collisions, respectively. The energy spectra of gray particles were fitted to the moving-source model. By the analysis with the two-moving-source model temperatures of two moving sources were found to be 51 and 176 MeV for p-Al collisions and 53 and 135 MeV for p-Au collisions.

The mean rapidity shifts of the leading particle from the beam rapidity were -1.9 and -2.3 for p-Al and p-Au collisions, respectively. The mean rapidities of produced particles were 2.8 for p-Al and 2.4 for p-Au collisions, respectively. Correlations between the leading rapidity shift and the multiplicity or the rapidity distribution were investigated. This study led us to the picture of multiparticle production in hadron-nucleus collisions such that the lost rapidity of the projectile produces not a few fast particles but many particles with nearly constant rapidity.

The nuclear stopping power of heavy nuclei was estimated as follows; a baryon going through the central region of heavy nucleus (for example, Au) loses 80 % of its incident energy on the average.

A Monte Carlo event generator MCMHA for high energy hadron-nucleus collisions has been developed on the basis of the multichain model. Experimental results have extensively been compared with predictions of the MCMHA. It was found that the MCMHA describes reasonably well global features of the hadron-nucleus collision data in the whole rapidity range.

CONTENTS

CHAPTER 1

INTRODUCTION

1.1 MOTIVATION FOR THE STUDY ON HADRON-NUCLEUS COLLISIONS

What we can directly see in a hadron-hadron (h-h) collision is the only information on the asymptotic state produced by an interaction.

Some information about what happens in the early stages after the collision can indirectly be obtained from a detailed study of produced particles in the final state, for example, by the study of interference effect between particles.

On the contrary hadrons in nuclear matter have an absorption length of a few fermis [1], which is smaller than radii of heavy nuclei. This fact points out that the nuclear matter can also interfere with the early stage of a multiparticle production process and that hadron-nucleus (h-A) collisions can be considered as a microscope for h-h collisions. Furthermore, the study of the space-time evolution of particle production seems to give a useful information on other kinds of high energy collisions, that is, e^+e^- and lepton-hadron collisions.

The earlier h-A experiments were performed by using emulsion techniques [2]. In emulsion experiments with no magnetic field a momentum determination of tracks is not precise enough. Therefore, analyses were limited to pseudorapidity, multiplicity distributions and correlations. However, they have been able to investigate the mean free path of excited hadron in the intermediate stage [3] and also suggest some physical picture about the space-time evolution of particle production. The latter was summarised as follows:

1. Low rapidity particles in the target fragmentation region are created in a distance shorter than nuclear radii.

2. Fast forward particles require longer time for their creation. Perhaps they are created outside the target nucleus.

The analysis using the naive cascade model [4] supports the fact that all particles are not created inside the target nucleus.

Some models [5][6-10] have been proposed in order to explain these experimental results of h-A experiments and they have been refined by successive experiments.

1.2 PRESENT STATUS OF THE STUDY ON H-A COLLISIONS

The quark-parton picture proposed for high energy particle interactions in 1960's [11] has succeeded to describe mostly static properties of hadrons. Furthermore it predicted the Ω^- particle in order to complete the baryon decouplet with spin and parity $J^P = 3/2^+$, and this particle was discovered later on in a bubble chamber experiment in 1984 [12].

This model has been developed to include dynamical properties of hadrons in the last decade. The Quantum Chromodynamics (QCD) as the basic dynamics of the quark-parton model has been successful in the jet analysis of e^+e^- collisions and in the explanation of deep inelastic lepton-nucleon scatterings [13]. One of the remarkable features of QCD is the prediction of a phase transition from nuclear matter to quark-gluon plasma (QGP) [14-16], which is supported by the study of lattice Monte Carlo calculations. In general the critical temperature and energy density are believed to be 150-250 MeV and >2 GeV/fm^3 [16]. These conditions seem to be satisfied by relativistic heavy nucleus-nucleus (A-A) collisions.

The possibility of the QGP formation in high energy A-A collisions has renewed experimental and theoretical interests in h-A interactions. This is because one may estimate the maximum baryon and energy densities attainable in A-A collisions by using the knowledge of the energy loss of projectile in high energy h-A collisions [17]. Furthermore, global analysis of high energy h-A collisions will enable us to select most probable scenario of the QGP formation in A-A collisions with the optimized conditions. Up to now, some analyses [6-10][17-18] have been done by using inclusive cross sections for p+A -> p+X at incident momentum of 100 GeV/c [19].

The analysis of ref.[17] has obtained the following results; (a) the probability that a baryon loses at least 90 % of its incident energy in traversing the central half of a lead nucleus is greater than 2/3, (b) in order to achieve the maximum baryon density in heavy ion collisions incident ions should have more than 25 GeV/nucleon, and (c) the maximum baryon density at head-on collision of heavy ions would be 5-10 times as large as in ordinary nuclear matter.

The analysis by R. C. Hwa et al [6] has shown the following; (a) the momentum-degradation length in nuclear matter for proton, Λ_p, is 17 fm (distance over which the proton's momentum decreases by 1/e), (b) the momentum-degradation of quark, Λ_q, is 160 fm and (c) the baryon stopping power is smaller than that of ref.[17]. On the other hand L.P.Csernai and J.I.Kapusta [9] showed that Λ_p = 4.9 fm from their analysis of the same data.

The analysis with the multichain model by S.Date et al [18] has presented the following;(a) the momentum-degradation length is 8±2 fm, (b) the maximum average energy deposition in 14 fm of nuclear matter is ≅30±10 GeV, (c) when $E_{cm}/A \cong 3\pm1$ GeV, where E_{cm} is a kinetic energy in the center of mass system, it is possible to reach the maximum baryon and energy densities in central collisions of heavy nuclei and (d) the maximum baryon and energy densities would be $(8\pm2)\rho_0$ and 5±3 GeV/fm^3 respectively, where ρ_0 is the normal nuclear density.

The lack of information on other particles than a leading proton is a weak point of above analyses. Thus, if we put the assumption that no secondary particle produced in the nuclear volume leaks out, most of the analyses support the formation of the baryon-rich QGP in heavy ion collisions. This fact requires more global analysis of h-A collisions in order to investigate where and how the incident energy is deposited in the nuclear matter and dissipated. Now, global analysis has begun with data of experiments which were provided with visible vertex chambers [20-22].

The data of a streamer-chamber experiment [20] of collisions of 200 GeV/c protons and anti-protons with p, Ar and Xe are available. This experiment has observed no significant differences between proton and anti-proton interactions. They have shown the multiplicity, rapidity and net charge distributions and also the long-range correlation between the forward and the backward multiplicities. Furthermore, the number of projectile collisions inside the nucleus was estimated in relation to the number of identified slow protons associated with the interaction. They investigated the dependence of multiplicity and rapidity distributions on the number of projectile collisions.

Preliminary analysis of data taken with the Fermilab Hybrid Spectrometer has been presented [21]. In this experiment interactions of 200 GeV/c π^+, K^+ and p beams with p, Mg, Ag and Au targets were investigated. Their preliminary result in h-A collisions has confirmed the previous estimate of 80-90 % energy loss in central collisions with heavy targets [17]. They also estimated the number of projectile collisions by the method similar to that of ref.[20] and investigated the correlation between the energy loss of projectile baryon and the number of collisions. Further, their investigations were extended to the problem as to where and how the energy is deposited and dissipated.

The results of the bubble chamber experiment with the same spectrometer as that of ref.[21] have been published [22]. They used 100 GeV/c p, $\bar{p}$, π^+, π^- and K^+ beams and a 320 GeV/c π^- beam, and Mg, Ag and Au as nuclear targets. In this experiment the momentum region of proton identification was extended up to 1.3 GeV/c, while in the streamer-chamber experiment [20] the corresponding region was only up to 0.6 GeV/c. They have shown clear violation of Koba-Nielsen-Olesen scaling in the multiplicity distributions for high energy h-A interactions of different A. Moreover, the correlation between the number of knocked-out protons and that of other particles was presented.

In this thesis the multiparticle production in high energy proton-nucleus collisions is experimentally studied. At the same time Monte Carlo event generator for h-A collisions is developed on the basis of the multichain model and its results are compared with experimental data. This Monte Carlo study of h-A interactions will be useful to understand the relativistic A-A collisions and to estimate the contribution of backgrounds to the QGP formation signature.

The data used in this analysis were obtained from the exposure of the European Hybrid Spectrometer equipped with the Rapid Cycling Bubble Chamber in which the foil targets of aluminium and gold were installed to 360 GeV/c protons. The overview of experimental set-up and data collection are given in chapter 2. The details of data reduction, scanning, measuring and data processing procedure, and of the event selection of proton-nucleus interactions are presented in chapter 3.

In chapter 4 the Monte Carlo event generator is described and its results are compared with other experimental data.

In chapter 5 the experimental results in proton-nucleus collisions is discussed. The multiplicity and rapidity distributions are compared with the models together with discussion. As the more global analysis, the correlations between the rapidity loss of projectile and other quantities are also studied. Chapter 6 is devoted to the conclusions of this work.

Reference to Chapter 1

[1] W. Busza, Proc. of the VI Int. Conf. on High Energy Phys. and Nucl. Structure (1975) 211

[2] For example, K. Gottfried, Proc. of the V Int. Conf. on High Energy Phys. and Nucl. Structure, Uppsala (1973); W. Czyz, Proc. of the 1978 CERN School of Physics, CERN Yellow Report CERN 78-10; and also see ref.[1]

[3] M. K. Hegab and J. Hufner, Nucl. Phys. A384 (1982) 353

[4] S. Hirabayashi, K. Kobayakawa and T. Morii, Prog. Theor. Phys. 61 (1979) 117

[5] As a review of soft hadron-hadron and hadron-nucleus collisions, K. Fialkowski and W Kittel, Rep. Prog. Phys. 46 (1983) 1283

[6] R. C. Hwa, Phys. Rev. Lett. 52 (1984) 492; R. C. Hwa and M. S. Zahir, Phys. Rev. D31 (1985) 499

[7] J. Hufner and A. Klar, Phys. Lett. 145B (1984) 167; A. Klar and J. Hufner, Phys. Rev D31 (1985) 491

[8] C. Y. Wong, Phys. Rev. Lett. 52 (1984) 1393

[9] L. P. Csernai and J. Kapusta, Phys. Rev. D29 (1984) 2664; L. P. Csernai and J. Kapusta, Phys. Rev. D31 (1985) 2795

[10] K. Kinoshita, A. Minaka and H. Sumiyoshi, Prog. Theor. Phys. 61 (1979) 165; ibid 63 (1980) 928

[11] M. Gell-Mann, Phys. Lett. 8 (1964) 214; G. Zweig, CERN Preprints CERN-TH 401 (1964) 412

[12] V. E. Barnes et al, Phys. Rev. Lett. 12 (1964) 204

[13] H. D. Politzer, Phys. Rep. 14C (1974) 129; W. Marciano and H. Pagels, Phys. Rep. 36C (1978) 137; A. J. Buras, Rev. Mod. Phys. 52 (1980) 199; A. Mueller, Phys. Rep. 73C (1981) 237

[14] L. D. McLerran and B. Svetitsky, Phys. Lett. 98B (1981) 195; J. Kuti, J. Polonyi and Szlachanyi, Phys. Lett. 98B (1981) 199; J. Engels, F. Karsch, H. Satz and I. Montvay, Phys. Lett. 101B 89

[15] M. Jacob and J. Tran Thanh Van, Eds, Phys. Rep. 88 (1982) 321

[16] "Quark Matter '84", edited by K. Kajantie, Lecture Note in Physics (Springer-Verlag)

[17] W. Busza and A. S. Goldhaber, Phys. Lett. 139B (1984) 235

[18] S. Date, M. Gyulassy and H. Sumiyoshi, Phys. Rev. D32 (1985) 619

[19] A. Barton et al, Phys. Rev. D27 (1983) 2580

[20] C. DeMarzo et al, Phys. Rev. D26 (1982) 1019; C. DeMarzo et al, Phys. Rev. D29 (1984) 2476

[21] R. J. Ledoux et al, presented at Gross Properties of Nuclei and Nuclear Excitation, International Workshop XIV, 1986, Hirschegg, Austria

[22] N. N. Biswas et al, Phys. Rev. D33 (1986) 3167

CHAPTER 2

EXPERIMENTAL SET-UP

The data to be used in the analysis of proton-nucleus interactions were obtained from the exposure of the Rapid Cycling Bubble Chamber (RCBC) with the European Hybrid Spectrometer (EHS) to a 360 GeV/c proton beam from CERN Super Proton Synchrotron (SPS). The experiment was called NA23. The experiment NA23 consisted of two separate runs; one performed in 1981 called as NA23 part A and the other in 1982 called as part B.

The foil targets, aluminium and gold, were placed in RCBC in NA23 part B in order to study hadron-nucleus interactions. The experimental set-up of NA23 part B can be seen in fig.2-1. All positions are given with reference to the center of RCBC.

The set-up consisted of three parts namely the beam line, the vertex detector RCBC and the spectrometer [1].

2.1 BEAM

The experimental set-up was placed on the H2 beam line [2] of the North Area, which transported beam particles from target

T2 to EHS (fig.2-2). A slow extracted primary proton beam was provided from the CERN SPS towards the target T2, which was made from beryllium. The primary beam had a duration of the spill of ≅2 seconds at repetition rate of one per ≅12 seconds.

In order to select particles with a certain momentum, the first vertical bending magnet was used for momentum analysis and the second was done for dispersion recombination. The second bending magnet served also as the central part of a spectrometer section for accurate momentum measurement.

The fourth stage included a section where the beam was made parallel in both horizontal and vertical planes. In this section two Cerenkov Differential counters with Achromatic Ring focus (CEDAR) were installed and offered the possibility to identify and flag particles according to their masses.

Following the focusing of the beam to a position of ≅70 m upstream of EHS, a final stage could be used to match the beam to the required conditions. In NA23 part B, the beam had a focus at ≅8.5 m downstream of RCBC in the horizontal plane. The depth of the beam in RCBC was coincided with its center having the full width of ≅6 mm. In the vertical plane the beam had the width of ≅6 cm (fwhm). The beam momentum was 360 GeV/c with momentum spread $\Delta p/p < 1$ %.

The use of the rapid cycling bubble chamber in beam H2 led to the installation of a pulsed magnet system [3] to modulate the beam spill in the primary beam branch feeding target T2 with protons. The system employed a fast kicker which deflected the beam vertically downwards, removing the proton spill from the target and thereby interrupting the production of secondaries for a number of short intervals during the spill. The kicker magnet could create a window covering the required sensitive time of the bubble chamber at an adjustable repetition rate. The interval of this window could vary between 0 and 2 ms.

In addition to the fast kicker magnet, the beam was equipped with a rotating collimator, placed upstream of T2, to take the primary proton off target T2. This collimator was rotated at a fixed frequency which was synchronised to the RCBC expansion rate.

Combining the effect of the fast kicker magnet and of the rotating collimator, it could be arranged that particles reached the RCBC virtually only during its sensitive time. Its effect was efficient to minimise the space charge effect in downstream drift chambers, especially in ISIS. Finally total beam flux was reduced to ≅500 particles/second.

2.2 THE RAPID CYCLING BUBBLE CHAMBER

The main component of the set-up is a vertex detector. In NA23 the Rapid Cycling Bubble Chamber (RCBC) was filled with liquid hydrogen (fig.2-3). The advantages of the bubble chamber were the following;

- being used as an interaction target,
- covering 4π solid angle around an interaction point,

- good efficiency for detecting charged multi-tracks,
- excellent spatial resolution, and
- useful ionisation information for the particle identification in the target fragmentation region.

In addition to these points, RCBC could have the rapid cycling of upto 30 Hertz. This rate allowed experiments typically with the sensitivity of ≅100 events/μb to be performed in a reasonable running period (< 1 month) at the SPS energy.

RCBC had a diameter of 80 cm and a depth of 40 cm. It was placed in a magnetic field of 3 T at its center, supplied by the superconducting magnet M1. The exit window of 2 mm stainless steel and the vacuum tank window of 3 mm Al/glass fiber corresponded to 14.6 % of a radiation length and 2.55 % of a collision length.

A forced hydraulic servo-system was chosen as an expansion system. Parameters about expansion system are shown in Table 2-1. Under the condition of 1.1 bar (expanded pressure) and 25K (operating temperature), a cycle time of 11 ms was required to get the bubble size of 300 μm. The bubble density was ≅10 bubbles per centimeter.

RCBC had three cameras. Events photographed in RCBC had three views with the bright field. The stereo angle between two cameras was 21°. The demagnification of RCBC optical system was ≅18.

The general characteristics of RCBC are summarised in Table 2-1.

The size of RCBC (a diameter of 80 cm) was such that slow protons and heavier ones (below 1.5 GeV/c) could be distinguished from others by ionisation information at the stage of film scanning. This function is very important to study hadron-nucleus interactions. Further it could separate fast forward going tracks with a sufficient resolution to connect with reconstructed tracks in downstream chambers.

Foil targets, aluminium and gold, were placed at the upstream side of RCBC by a cramping system. Fig.2-4 shows the cramping and foil system. The installation of nuclear targets in RCBC had the following advantages;

- determination of an interaction point with high precision.
- detection and identification of heavy fragments with low momenta.
- detection of neutral and charged strange particles.

The size of aluminium and gold foil was 5 cm x 0.6 cm x 1.6 mm and 5 cm x 0.6 cm x 0.3 mm respectively, and each foil was installed with the angle of $18^{o}30'$ with respect of the vertical plane. This setting position and size of foils were useful to identify most of slow protons with momenta of > 150 MeV/c. Fig.2-5 shows the picture of typical foil interaction in RCBC.

2.3 THE EHS SPECTROMETER

The EHS spectrometer [1] consisted of the upstream and the downstream. The latter had the first lever arm from RCBC to the magnet M2 and the second lever arm below M2. The EHS spectrometer had following functions;

- reconstruction of an incident beam,
- determination of momenta of secondary charged particles, in particular of relativistic ones for which RCBC could not have enough precision,
- particle identification of secondary charged particles, and
- detection of γ-ray and reconstruction of π^{0}'s and η's.

2.3.1 The Upstream

The upstream made of two wire chambers, U1 and U3, which were installed at ≅30 m and ≅2 m upstream of the RCBC respectively. Each of them was a multi-wire proportional chamber (MWPC) with five planes and the wire spacing was 2 mm. Two chambers had a effective area of 26 x 36 cm^2. The incident beam was reconstructed by U1 and U3 with the precision of ≅450 μm (r.m.s.).

The chambers were flushed with a mixture of argon (72%), isobutane (23%), freon (1%) and methylal (4%). The track detecting efficiency of these chambers exceeded 99.5%.

2.3.2 Magnets M1 And M2

The vertex magnet M1 surrounded the vertex detector RCBC. M1 had two circular superconducting coils of about 80 cm inner and 120 cm outer radii, which supplied the magnetic field of 3 T at the centre with the operating current of 4000 A. This field was rather similar to a pure solenoid field, the central field being very close to cylindrical symmetry.

In addition to M1, the momentum analysing magnet M2 was placed at the distance of 17 m downstream from the centre of RCBC. M2 was a C-shaped magnet with two racetrack coils, a gap width of 40 cm and pole faces of 100 cm x 200 cm, its aperture being 40 cm x 100 cm. In order to shield photo-multipliers of the intermediate gamma detecter (IGD) from the stray field of M2, an iron plate (3 m x 3 m) with a hole of 40 cm x 100 cm was placed in the upstream side of M2 at a distance of 150 cm from the centre of M2. M2 provided a field of 1.5 T at its centre with its operating current of 1000 A.

2.3.3 Wire Chambers

A multi-wire proportional chamber W2 and drift chambers, D1, D2 and D3, were installed in the first lever arm, and drift chambers, D4, D5 and D6, in the second lever arm. These wire chambers provided the measurement of impacts for the track reconstruction of fast secondary particles.

W2 was placed at the distance of ≅1.5 m downstream from the centre of RCBC. W2 consisted of six planes with the sense wire spacing of 2 mm, covering an acceptance of 1.2 x 2.15 m^2 which corresponded to an angular acceptance of 0.38 x 0.62 rad^2. Wires of each plane had the angle of 0^o, 30^o, 10.9^o, -10.9^o, -30^o and 0^o to the horizontal, respectively. W2 served to determine the position with the accuracy of ≅400 μm inside M1 fringing field, where drift chambers could not be used because of the presence of strong magnetic field. As its response speed was fast, W2 signals were also used to form the trigger system.

Drift chambers contained four planes with sensitive areas of 2.1 x 4.25 m^2 (D1-D3) and of 2.0 x 1.3 m^2 (D4-D6). Sense wires of each plane had the angles of approximately 16.7^o, 5.7^o, -5.7^o and -16.7^o with respect to the horizontal plane. These angles were chosen to satisfy the condition of the butterfly configuration [4]. The butterfly configuration was adopted in order to minimise the ambiguities in the reconstruction of multi-track impacts. For this configuration the distance between consecutive sense wires vary from plane to plane, in such a way that the distance between the sense wires along the frame were all identical. This distance was 48 mm.

The chambers were filled with mixture gas of 50% argon and 49% ethane with a small admixture of ethanol. Typical operating conditions are listed in Table 2-2. The mean drift velocity was 47 μm/ns for D1-D3 and 53 μ/ns for D4-D6. The precision of an impact reconstructed in a drift chamber was about 200 μm in the bending plane.

2.3.4 The Silica Aerogel Detector

The Silica Aerogel Cerenkov Detector (SAD) [5,6] was located about 3 m downstream from the centre of the magnet M1. It was composed of 18 identical modules, each of which had a sensitive surface of 23 x 55 cm^2 and the aerogel thickness of 14 cm on the average. Total sensitive surface of SAD was 2.3 m^2. Because of the important stray field of M1, these modules were installed behind a 20 cm thick iron shielding plate with an opening of 290 x 115 cm^2. Each of 9 modules was on the upper and lower side with respect to the beam line, respectively, and covered the aperture with the exception of an 80 cm gap designed to allow transmission into the downstream of particles with momenta of > 5 GeV/c.

The refractive index of the aerogel was 1.031 which gave a threshold momentum of 0.56 GeV/c for π, 2.0 GeV/c for K and 3.8 GeV/c for protons respectively. The SAD modules, each viewed by two 11 cm diameter photo-multipliers, gave typically a signal of 7-8 photoelectrons for a $\beta = 1$ particle. Each group of photo-multipliers was shieled by an iron box. SAD was useful for particle identification in the momentum range of 0.5-4.5 GeV/c [6].

2.3.5 ISIS

A large pictorial drift chamber ISIS 2 (Identification of Secondaries by Ionisation Sampling) [7] had its centre at 8 m downstream of RCBC, and the fiducial volume of 4 m (height) x 2 m (width) x 5 m (length) filled with Ar/20%-CO_2. It was equipped with 320 wires transverse to beam in a central horizontal plane with the distance of 1.6 cm between consecutive channels. High tension of maximally 120 kV supplied at the top and bottom electrodes with respect to the central plane.

The ISIS measured the ionisation of each track so that the particle mass might be deduced when its momentum was also known. This technique relied on the relativistic rise of the ionisation of a charged particle in a gas and has been described elsewhere [8]. The ionisation resolution of 8.3 % fwhm was close to the theoretical performance. Electrons were uniquely resolved at the 1 % level for the momenta range below 20 GeV/c, whereas for K/π separation the range was 3-30 GeV/c.

In addition to particle identification, ISIS provided two track resolution of ≅2 cm, separated tracks upto ≅100 GeV/c due to the strong dispersive power of the vertex magnet M1. The tracks reconstructed in ISIS reduced ambiguities of the track reconstructions in the spectrometer.

2.3.6 The Forward Cerenkov Detector

The Forward Cerenkov Detector (FC) was placed at about 25 m downstream of RCBC. Its position was in the second lever arm.

The effective dimension of the radiation volume of FC was 1200 cm long, 104 cm wide and 200.2 cm high. It was equipped with 14 cells, each of which composed of a concave mirror for light collection with a radius of curvature of 2 m cut as a 28.6 cm x 52.0 cm rectangle shape, and a phototube for light detection.

FC was filled with He with the temperature of ≅230 ^{o}C and the atmospheric pressure at the operation of NA23 part B. Its refractive index was ≅$(1+19\times10^{-6})$ and had the threshold momentum of 24 GeV/c for π, 85 GeV/c for K and 161 GeV/c for protons [9]. The expected number of photoelectrons was ≅6 for a $\beta = 1$ particle. FC was useful for $\pi/(Kp)$ separation in the momenta range of 30-90 GeV/c and for $p/(\pi K)$ separation in the range of 115-160 GeV/c.

2.3.7 The Transition Radiation Detector

The Transition Radiation Detector (TRD) was positioned at ≅36 m downstream of RCBC. TRD consisted of 20 units of foil stacks coupled with xenon filled proportional wire chambers. Foil stacks made from 450 sheets of mylar with the thickness of 5 μm on the average. The total effective volume was 350 cm (length) x 70 cm (width) x 170 cm (height).

The principle of particle identification by TRD relied on the fact that the yield of emitted transition radiation X-ray at the time a charged particle passed between materials with different refractive indices were proportional to the Lorentz factor of it. The X-ray emitted from mylar foils was detected by wire chambers, and at the same time wire chambers detected the dE/dx of passing charged particles. TRD was useful for particle identification in the momentum range above ≅100 GeV/c, in which signals of transition radiations exceed those of dE/dx, and was complementary to other particle identification devices.

2.3.8 Gamma Detectors

For the detection of photons and electrons there were two electromagnetic calorimeters, the Intermediate Gamma Detector (IGD) and the Forward Gamma Detector (FGD) [10].

The IGD, positioned 14 m downstream of RCBC, was consisted of 1122 lead glass blocks with a cross section of 5 cm x 5 cm and the length corresponding to 15 radiation lengths. The detection surface was 195 cm x 160 cm, with a central hole of 35 cm x 90 cm matching the gap of the magnet M2.

The FGD was placed 39 m downstream of RCBC. It was made of three sections; a converter plane, a position detector and an absorber plane. The converter and the absorber consisted of 140 lead glass blocks, between which a finger hodoscope composed of 375 scintillators was placed. The thickness of the converter corresponded to 4.7 radiation lengths, and that of the absorber did to 24 (central) and 16 (upper and lower) radiation lengths. The detection surface was 120 cm x 210 cm and covered the image of the hole in the IGD at the end of spectrometer.

The energy resolution (fwhm) was $\Delta E/E = (15/\sqrt{E} + 2)\%$ for the IGD and $(10/\sqrt{E} + 2)\%$ for FGD, with E in GeV, respectively.

The spatial precisions (r.m.s.) for IGD and FGD were 3.7 mm and 2.5 mm, respectively, in their respective energy ranges ($\cong$5 GeV and $\cong$50 GeV). In IGD it was possible to resolve two showers of equal energy down to a separation of 25 mm, with a 95 % confidence level. On the other hand, in FGD two separate showers were recognised if their separation was larger than

30 mm. This allowed one to separate the two gammas from π^0 of momenta up to 300 GeV/c.

2.4 OVER-ALL PERFORMANCES

Concerning charged tracks, RCBC gives informations of event topology and of particle identification for slow heavy particles. RCBC had generally the precision of ≅50 μm and the resolution of ≅250 μm.

The acceptance of the spectrometer is shown in fig.2-6 as a function of the longitudinal momentum. A particle with the longitudinal momenta of more than 5 GeV/c could be detected by at least two chambers (W2 and D1) and be reconstructed. Tracks with lower momenta could be determined by RCBC with sufficient accuracy. The tracks accepted with downstream chambers were reconstructed in the spectrometer and were hybridised with the corresponding tracks in RCBC if possible. As the results, the relative accuracy $\Delta p/p$ in the measured momentum could be expected to be less than 2 % in the range of 0 - 360 GeV/c. Fig.2-7 shows $\Delta p/p$ for non-hybridised tracks and for hybridised tracks as a function of momentum.

For neutral particles a large fiducial volume of RCBC provides informations of strange particles which were produced at primary interactions and decayed in RCBC visible volume. Gammas from π^0 decay could be also detected when they converted into e^+-e^- pair in RCBC. Data of gammas were combined with those from downstream gamma detectors and were used to reconstruct π^0.

2.5 THE TRIGGER

The "Minimum Bias Trigger" was implemented to take bubble chamber pictures and to read out the data from the electronic detectors when an interaction occurred. The trigger configuration is shown in fig.2-8. This trigger system consisted of four hodoscopes, T1, T2, V1 and V2, placed on the beam line upstream of RCBC, and two trigger hodoscopes, ITH and ITV, positioned at ≅12.5 m downstream of RCBC. The horizontal trigger hodoscope (ITH) was composed of 26 horizontal scintillator strips, 20 of 2 cm width and 6 of 15 cm width, and the total detection area was 40 cm (horizontal) x 130 cm (vertical). The vertical trigger hodoscope (ITV) was made of two scintillator strips of 5 cm width and of a middle finger of 0.6 cm width.

The beam was focused at about 4 m upstream of the middle finger ITV(2) of the vertical trigger hodoscope with the width of ≅0.4 cm (fwhm).

The trigger condition is summarised as the following logical expression;

$$BEAM*\{[ITH(n\geq 2) \text{ or } [ITH(n\geq 1)*\overline{ITV(2)}]\}$$

where,

$$BEAM=T1*T2*(\overline{V1+V2})$$

which required an incoming beam particle of the position matched with the focus of RCBC optical system and vetoed upstream interactions. In the trigger condition the first part accepted interactions of at least two charged particles hitting ITH, and the second was designed to pick up reactions with one fast forward going particle, required not to be a beam particle.

The minimum bias trigger was efficient for taking picture with interactions, whereas some of low multiplicity event were lost. This trigger inefficiency was observed mainly in the two-prongs events. It was negligible for proton-nucleus interactions, as most of them were of high multiplicity.

Reference to Chapter 2

[1] M. Aguilar-Benitez et al, Nucl. Instr. and Meth. 205 (1983) 79

[2] P. Coet, N. Doble and S. Reucroft, CERN Yellow Report 82-01 (1982) 163

[3] H. van Brungel and N. Siegel,
A pulsed magnet system to modulate the beam for rapid cycling bubble chambers, CERN/SPS/81-13 (ABT) (1981)

[4] F. Bruyant et al, Nucl. Instr. and Meth 176 (1980) 409

[5] P. J. Carlson et al, Nucl. Instr. and Meth. 192 (1982) 209

[6] C. Fernandez et al, Nucl. Instr. and Meth. 225 (1984) 313

[7] W. W. M. Allison et al, Nucl. Instr. and Meth. 224 (1984) 396

[8] W. W. M. Allison and J. H. Cobb, Annual Review of Nuclear Particle Science 30 (1980) 253

[9] J. Alberdi et al,
The Forward Cerenkov Calibration for the Different Experiment in EHS, CERN/EP/EHS/LEDA 84-6

[10] B. Powell et al, Nucl. Instr. and Meth. 198 (1982) 217

CHAPTER 3

DATA REDUCTION

3.1 RAW SAMPLE

During the runs of NA23 part B, a total of 195,000 triad photographs were taken together with the electronic detector data recorded in magnetic tapes. This resulted 22 rolls of pictures. Two rolls were not used for subsequent analysis because one was taken with no magnetic field for the calibration purpose and the other was taken with the beam position off the foil targets. 180,000 pictures were useful for the analysis.

3.2 SCANNING

We have performed the scanning for all pictures. In the scanning the transverse position of the interacting beam was predicted by the information of the upstream wire chambers. When there was a primary interaction corresponding to the prediction, the secondary activities were looked for. The event class was assigned to all of the frames scanned according to Table 3-1, and the information of secondary activities if any was recorded. Normal scanning was carried out at least two times, and if there was a difference between them, it was resolved by the physicist scan. The events whose primary vertices were not visible in the shade of foil targets were classified as candidates of foil interactions and event class 20 was assigned.

In order to reject the contamination of pp interactions we did the special scanning for events labeled as event class 20. In this step the followings were recorded;

1. total multiplicity,
2. number of identified protons,
3. number of thin positive tracks,
4. number of thin negative tracks,
5. number of secondary activities (V^{o},V^{+-} and γ), and
6. position of the primary vertex (x,y,z).

We classified secondary tracks outgoing from the primary vertex into gray and shower tracks. A gray track was defined as a positive particle with momentum of 0.15 ÷ 1.2 GeV/c corresponding to $\beta \cong 0.1 \div 0.8$. The rest of secondary tracks were defined as shower tracks.

3.3 MEASURING

The number of events labeled as event class 20 in the scanning was about 50 per a roll on the average, and one roll had about 9000 pictures. Fig.3-1 shows the total multiplicity and the gray multiplicity obtained in the scanning as a function of z-position of the beam prediction. It is clear that almost all events in the positive z region have multiplicities consistent with those of proton-proton interactions. Therefore we considered these as contaminations from pp interactions. According to this reason, we have decided to measure all events having the primary vertex of negative z. This selection rule has reduced the number of events to be measured by ≅ 60 %, while removing about 30 events with ≥ 2 gray tracks out of 962 events.

The measurements have been done at each laboratory. But the Tokyo group has done more than its normal share because some laboratories asked Tokyo to do their parts. We used a semi-automatic measuring machine SWEEPNIK (SNK) [1]. It was necessary to keep the measuring machine SNK stable as long as possible, because it took at least two hours to measure one view of the event with multiplicity of ≥ 50. The highest multiplicity of events measured in Tokyo was 86.

For the reconstruction of tracks in the RCBC using these measurement data, the positions of the image (film) planes with respect to the RCBC were needed. In order to determine these coordinates the fiducial marks on the windows of the RCBC in all views were measured. Fig.3-2 shows the distributions of residuals between the measured and title constant values of fiducials. These distributions have peaks at zero. The precisions of fiducial measurement by SNK are about 5.3 μm and about 5.6 μm for x- and y-direction, respectively.

In each view we have measured fiducial marks, vertex points and track points. Using fiducial measurements we have determined transformation coefficients between film planes and the RCBC. Vertex points were reconstructed in space with these coefficients. The errors of the point reconstruction were ≅170, ≅65 and ≅460 μm in space for x-, y- and z-direction, respectively. The distributions of residuals of the circle fitting for secondary tracks had means values of 71, 75 and 77 μm in space for each view.

The values related the accuracy of measurement with SNK are summarised in Table 3-2. The errors of the point reconstruction for all measurement data are also listed in this table. Concerning the accuracy of measuring devices, there is no significant difference between SNK and others.

3.4 OFF-LINE SOFTWARE

The EHS off-line software [2] consisted of two groups. The first was the pre-production group with the following subprograms:

- Calibration programs, for the determination of the RCBC optical constants.

- Survey programs, for the careful positioning of the wire chamber planes, for the determination of the relationship between the RCBC reference system and the Spectrometer system, and for the precise positioning of ISIS and the gamma detectors.

- Test programs.

The objects of these programs were to determine or to check all parameters (the so-called 'Title constants') of the experimental set-up for a given period of time.

The second was the production group with the following subprograms:

- Synchronising and formatting of all data relevant to one event.

- Reconstruction programs, including ISIS and gamma detectors.

- Analysis programs.

In the EHS software the following interfaces have been developed to match all situations with enough flexibility:

- The NORD-100 data acquisition record structure, which is readable with the FQM Hydra package.

- The input data structure to the reconstruction programs.

- The Geometry Summary Tape (GST) data structure, which is output from the reconstruction programs.

A schematic map of the program chain is given in Fig.3-3. The EHS software has been supported by two software systems; the Hydra system [3] and the PATCHY programs [4].

The HYDRA system is the memory management system and consists of many packages. One of them is the FQM/FQT package to read/write data structure on tape/disk. This I/O package is computer-independent and is extremely useful for the exchange of data between different computers.

The source codes of all programs are written in the PAM files of the PATCHY with their PATCH/DECK structure. This tool gives the programs the flexibility of the multi-version and of the additional options. Furthermore it is useful for the modification of programs.

3.4.1 The RCBC And The Spectrometer System

The RCBC reference system is a right-handed rectangular co-ordinate system (xyz) defined as follows:

- the x-y plane is the inside face of the RCBC glass window, with the origin at the centre.
- the x-axis is nearly horizontal.
- the y-axis is nearly vertical-up, so that the z-axis points towards the cameras.

On the other hand, the Spectrometer system is a right-handed rectangular co-ordinate system (XYZ) with:

- the X-axis horizontal along the "ideal beam line" precisely defined in the SPS reference system.

- the Y-axis vertical-up.

- the origin at the intercept of the X-axis with the y-z plane of the RCBC reference system.

In the first approximation the relationship between the RCBC reference system and the Spectrometer system was obtained from the geometric survey of positions of spectrometer components. The precise relationship between the RCBC reference system and the Spectrometer system has been computed by the survey programs using through-going beams. The precise positioning of the wire chamber planes with respect to the Spectrometer system has been also done by the survey programs using beam data.

The usual choice of kinematical variable is the following:

- $1/P$: the inverse of the momentum

- λ : the dip angle ($-\pi/2 < \lambda < \pi/2$)

- ϕ : the azimuthal angle ($0 \leq \phi < 2\pi$)

Finally three components of the momentum vector are calculated as follows:

- $P_x = P\cos\lambda\sin\phi$

- $P_y = P\cos\lambda\cos\phi$

- $P_z = P\sin\lambda$

3.4.2 Software Survey Of Wire Chambers

The required precision of the spectrometer comes from two aspects [5]. One is that data are to be free of any systematic errors. It requests that the uncontrolled residual fluctuations should not exceed 50-100 μm [6]. Another is the possibility within any given chamber to reconstruct the impacts as unambiguously as possible.

The co-ordinate used to describe an impact in a wire plane is defined as follows:

- X : the X position in the Spectrometer system, which wire planes are assumed to be perpendicular to.

- β : the wire inclination angle measured with respect to the Y-axis.

- ρ : the radial distance of a wire to the X-axis.

Such that the (X, ρ, β) system is right-handed. By convention, ρ is computed in the following way;

$$\rho = \rho_0 + nW$$

where n is the wire number, ρ_0 the co-ordinate of the fictitious wire "zero" and W the pitch signed (positive for the configuration where n increases along the positive ρ direction, negative otherwise). (Fig.3-4)

The precise positioning of wire chambers with respect to the Spectrometer system was performed by the program SURVEY using the data of beam tracks going through these chambers and the geometric measurement data. The program SURVEY defines two reference planes in each of the proportional chambers U1 and U3, which were placed at the upstream side of the RCBC. All other planes are located with respect to the reference planes.

We illustrate the procedure of the program SURVEY in an oversimplified case - two-dimensional problem. Consider a family of tracks whose slopes T_Y^i are defined by upstream chambers, where i is the i-th track. Further, suppose these tracks have intercept B_Y^i, which can be determined for each track by knowing the number of the wire fired in each reference plane.

If the location of another chamber is X_c, Y for i-th track can be predicted:

$$Y_p^i = T_Y^i X_c + B_Y^i$$

We also know which wire fired in the chamber at X_c, thus can calculate Y_f^i for the fired wire. The difference between the predicted and the measured value for the chamber at X_c is defined as follows:

$$\Delta\rho = \rho_p^i - \rho_f^i$$

The shift of the centre of $\Delta\rho$'s for many beam data is a measure of the correction to ρ_0 for the corresponding plane. After several iterations ρ_0 is determined. In the realistic case, that is three-dimensional, ρ_0 is defined to be the position of the wire "zero" of corresponding plane relative to the EHS Spectrometer system.

In order to remove the uncertainty due to the beam momentum or to the field mapping of magnets, it is better to do a separate run with no magnetic field. However, through beams with field-on are essential for establishing the relationship between the RCBC system and the Spectrometer system. Comparing the value of ρ_0

from field-on with the corresponding one from field-off, we can check the problem caused by the calibration of the magnets [7].

The final purpose of this program is the determination of ρ_0 for each wire chamber and also of zero drift time t_0 and drift velocity v_d for all drift chambers.

3.4.3 Survey Of RCBC

As determined the title constants of each wire chamber, it is important to fix the position of the RCBC relative to upstream chambers, that is the Spectrometer system, because tracks recorded in each reference system have to be combined.

At first, beam tracks in the RCBC were measured and reconstructed in the RCBC reference system. Each track can be described by the slopes T_y, T_z and the intercepts B_y, B_z. These parameters may be calculated for both RCBC and Spectrometer system. From the comparison of their known parameters an average translation $\vec{T}$ and an average rotation matrix R were computed which fix the transformation from the Spectrometer system to the RCBC reference system:

$$\vec{X}_{RCBC} = (R)\vec{X}_{SP} + \vec{T}$$

This survey has to be done with magnetic field-on data, because of the possible influence of the magnetic field upon the absolute position of the RCBC.

3.4.4 ISIS Calibration

As the drift velocity and gas amplification depended strongly on the gas composition, gas pressure and so on, the drift velocity, gain and attenuation constants for ISIS were calibrated for each 24 hours period (or more often when the ambient pressure changed significantly). These calibrations were performed by the program SVISIS using a few thousand reconstructed tracks in every periods. In each calibration period the drift velocity was optimised for the matching of tracks in ISIS to those in the spectrometer. The residuals to such matching had a spread of 1.6 mm (r.m.s.) in position and 0.4 mrad in angle [8].

If the momentum p of a track is known, the value of $\beta\gamma$ = p/mc can take on a few discrete values depending on the chosen mass m. The ionisation relative to minimum, I/I_0, depends only on $\beta\gamma$ and these measurements are in good agreement with theoretical calculation [9]. Therefore, in our calibration procedure this dependence was assumed. The ratio I/I_0 depended only on the gas amplification and the small exponential loss of observed pulse height due to electron attachment by residual oxygen molecules. The calibration proceeded in three steps:

1. All tracks are assumed to be pions. Though this may be untrue for ≅10% of tracks, this crude assumption gives calibration constants based on many tracks which are not in error by more than 2%. The amplification factors and attenuation constants are fitted by the least-squares method for each drift space separately.

2. In the second step tracks are chosen whose momenta and ionisation errors are such that the expected I/I_0 for a pion is more than 3.3σ from that expected for electron or kaon

and whose measured ionisation (using the calibration constants from step 1) is within 2.0σ of the pion prediction. Since the calibration is good to about 1σ at this point, this sample is clean enough to estimate better values of the amplification and attenuation constants.

3. In the final step the selection is improved with the new values and the constants are recalculated.

3.4.5 The Track Reconstruction

First those tracks which are fast enough to enter the second lever arm of the spectrometer are reconstructed by the program GEOHYB. Impacts are reconstructed in the second lever arm and are combined to produce spectrometer track elements. Track candidates coming from any one of vertices in the bubble chamber, which are pointing close to a vertex in the non-deflection plane and having a reasonable impact parameter to that vertex in the deflection plane, are used. For each track candidate, assuming that the point from which it originates is the primary vertex, predictions are made for the intercept of the track at the positions of the wire chambers in the first lever arm. For each chamber in the first lever arm the hits compatible with the prediction in each plane are selected and combined to form impacts in those chambers. If no prediction is satisfied in two consecutive chambers the track candidate is rejected.

Each candidate in the first lever arm is combined with its parent candidate in the second lever arm and a global spectrometer fit is performed which takes into account the multiple scattering and return the best track parameters at the level of the first chamber W2 in the first lever arm. For each surviving candidate the best approximation of the track parameters at each possible vertex with their errors is computed. The next step is to identify which bubble chamber track image in each view is compatible with the prediction. For each acceptable pair of track images a hybrid fit is performed which makes use of the film measurement in the views on one hand and of the results of the spectrometer fit on the other (so-called "hybridised track").

Once all fast tracks in the forward cone have been reconstructed, it is easier to reconstruct unambiguously impacts in the first lever arm chambers, discarding impacts candidates with many used wires. The track candidates in the first lever arm are obtained. For each track candidate a complete hybrid fit is performed using all information compatible with the track. The final results for all hybridised tracks found can be inconsistent and the best solution is then searched for. Any track found in both lever arms is reinjected to take part in the final decision process.

Spectrometer tracks which passed the spectrometer fit and failed the hybrid fit, or spectrometer tracks which have been discarded in the final decision are kept temporarily as "hanging tracks", which may correspond to fast secondary products.

The track images which have not been hybridised are used to reconstruct tracks only in the bubble chamber. In the presence of the magnetic field the momentum can be known. For the track whose momentum is less than 1.5 GeV/c, the mass dependent fit is applied because such a track is affected by the ionisation loss and the multiple scattering. In foil events we try the masses of proton, deuteron, triton and alpha particle for the track which is labeled as an identified proton or a possible stopping track by the scanning.

The bubble chamber tracks, whose momenta are > 2 GeV/c and reach at least up to W2 chamber by swimming-out, are combined with hanging tracks. This procedure may achieve hybrid fits for some tracks and give better track parameters to it.

3.5 EVENT SELECTION

3.5.1 Performances Of Track Reconstruction

608 events of 21 rolls were measured by laboratories and measurement data have been collected at Tokyo. 18 events were rejected because of no magnetic field. 593 events of 20 rolls were available as the inputs to the geometry reconstruction program GEOHYB. After the program GEOHYB, we have obtained 580 events on the Geometry Summary Tape (GST). 13 events failed in GEOHYB, because of CPU-time-over, memory space overflow and so on.

The overall reconstruction efficiency was ≅96 % and that for the tracks from the primary vertices was ≅97 %. We defined the reconstruction efficiency as the ratio of the number of successfully reconstructed tracks to the maximum number of tracks measured in views. Most of fast tracks (especially >5 GeV/c) can be detected by the first two wire chambers, W2 and D1. However, about 2% of the particles may interact before reaching the spectrometer through the exit wall of the RCBC. To estimate the hybridisation efficiency we investigated the number of tracks in the RCBC with the following conditions:

momentum $p > 1.0$ GeV/c,

dip angle $\mathrm{Abs}(\lambda) < 200$ mrad. and

azimuth angle $\phi < 200$ mrad.

We accepted them as the tracks which might be combined with the spectrometer ones. (35±1) % of the tracks observed in the RCBC satisfied the above conditions. We examined whether they could go through the hybrid fit or not, and have obtained the hybridisation efficiency of (88±2) % for these selected tracks.

3.5.2 Positioning Of Foil Targets

We have known only approximately the position of the foil targets relative to the RCBC (see fig.2-4) from the geometric survey. In order to determine an exact position of targets with respect to the Spectrometer system we used the spacially reconstructed vertex points. Fig.3-5 shows the distribution of the primary vertices projected onto the X-Y plane. The circles represent the events whose gray multiplicity is $\geq$ 2. These events are considered to be genuine foil interactions. Whereas the crosses are those with gray multiplicity of ≤ 1. One can see an inclination of cluster of events with gray multiplicity of ≥ 2. From the correlation between X and Y, we have corrected X as a function of Y using the following expression:

$$X' = X + 0.02Y$$

Using the corrected X, we show the projection of the primary vertex onto X-Z plane in fig.3-6. The region of foil targets was defined as follows:

1) $-0.75 \leq Z \leq 0.$ (cm)
2) $X' = X + 0.02Y$

   $2.6786(X'-0.2) + 76.126 \leq Z \leq 2.6786X' + 76.126$
3) $-5.0 \leq Y < 0.0$ for Al

   $0.0 \leq Y \leq 5.0$ for Au

The boundary in the X-Z plane is displayed by a parallelogram in this figure.

After the selection based on this region of foil targets, we had 239 events of proton-nucleus interactions. Out of 239 events, 47 events were classified as p-Al interactions and 192 events as p-Au interactions.

3.5.3 Consistency Of Samples From Different Laboratories

In Table 3-3, the summary of events measured in each laboratory is shown. Table 3-3 also presents the number of events per roll for each laboratory. As there might be small changes of beam profiles, the values of each sample are consistent with about 2.4 events/roll for p-Al interactions and with about 9.6 events/roll for p-Au interactions.

Fig.3-7 shows the means of total charged multiplicity and of gray multiplicity for each sample. These values were taken from scanning data. Concerning the total charged multiplicity, values of each sample were compatible with for p-Al and p-Au collisions respectively.

The reconstruction and hybridisation efficiencies of each sample are summarised in Table 3-4. They indicate a good consistency among samples from different laboratories.

Reference to Chapter 3

[1] K. Namatame, Master Thesis of Tokyo Univ. of Agriculture and Technology (1981); T. Shimazaki, Master Thesis of Tokyo Univ. of Agriculture and Technology (1985) - unpublished.

[2] F. Bruyant, EHS OFF-LINE SOFTWARE STATUS - STATUS REPORT, CERN/EP/EHS/PH 79-4

[3] J. Zoll et al, HYDRA Topical Manuals, CERN Program Library

[4] J. Zoll et al, PATCHY Manual, CERN Program Library

[5] F. Bruyant,
Wire Chamber Software SURVEY and Related Topics, CERN/EP/EHS/PH 78-15

[6] L. Montanet,
Systematic errors on EHS - unpublished.

[7] Y. Iga, Master Thesis of Tokyo Univ. of Agriculture and Technology (1983) - unpublished.

[8] W. W. M. Allison et al, Nucl. Instr. and Meth. 224 (1984) 396

[9] I. Lehraus et al, Nucl. Instr. and Meth. 153 (1978) 347

CHAPTER 4

THE MULTICHAIN MODEL

There have been many models [1-8] about the multiparticle production processes in high-energy hadron-nucleus collision with low-transverse-momentum. Models which have been successful to describe hadron-nucleus and nucleus-nucleus collisions are for example;

1. Multichain model [1-3],

2. Additive quark model [4-8].

As was mentioned in the introduction we will restrict ourselves here to the multichain model (MCM) [2,9]. In section 1 we will describe the concept of MCM, which we have formulated in a Monte Carlo event generator (MCMHA), and the detailed description of the Monte Carlo event generator is given in section 2. Furthermore we will compare its results with other experimental data.

4.1 BASIS OF THE MULTICHAIN MODEL

4.1.1 Kinematical Variables

Firstly, we define the co-ordinate system for the Monte Carlo simulation as follows;

- z-axis is along the incident beam line.
- xy-plane is perpendicular to the z-axis.
- the origin is at the centre of the target nucleus.

Neglecting the Fermi motion of nucleons inside nucleus, we define the kinematical variables in the laboratory system. Four-momenta of the projectile hadron, a nucleon in the target nucleus and an emitted hadron are denoted as $(E,\vec{0},P_z)$, $(m_N,\vec{0},0)$ and $(\epsilon,\vec{p}_T,p_z)$, respectively, where m_N is a nucleon mass. Using these variables, we define the light-like momentum fractions of the produced hadron as;

$$x_+ = (\epsilon+p_z)/(E+P_z), \qquad (4.1)$$

$$x_- = (\epsilon-p_z)/m_N. \qquad (4.2)$$

The rapidity, which is defined by

$$y = (1/2)\ \ln(\epsilon+p_z)/(\epsilon-p_z) \qquad (4.3)$$

has the following relation to the light-like momentum fractions, x_+ and x_-:

$$x_+ = x = m_T e^y/(E+P_z), \qquad (4.4)$$

$$x_- = m_T e^{-y}/m_N. \qquad (4.5)$$

Here, m_T is the transverse mass and is given by $m_T = \sqrt{(m^2+p_T^2)}$, where m is the mass of the emitted hadron.

4.1.2 Basic Concepts

We will explain the basic concepts of MCM, on which our Monte Carlo event generator MCMHA is based.

The basic assumptions of MCM are as follows [2,9]:

1. The transverse-momentum distribution is independent of incident energy, nuclear size and longitudinal momentum.

2. The probability that an incident hadron undergoes exactly n interactions is given by Glauber theory.

3. The reaction consists of two stages;

   - fast multiple collision stage, which determines the longitudinal-momentum distribution of the leading particle.

   - slow fragmentation stage, in which secondary hadrons are produced.

4. The fragmentation stage is independent of the number of collisions involved in the first stage.

5. Concerning the multiple collision dynamics, the longitudinal-momentum distribution depends only on the light-like momentum fraction, x (eqs. (4.1) and (4.4)).

6. Projectile and target fragmentation processes are independent each other.

This physical picture is schematically presented in fig.4-1. When a projectile hadron interacts with a nucleon in the target nucleus, a hadronic chain is stretched between the projectile and target nucleon. Considering the chain at the level of quark-parton, it is consistent with a dual parton model [3]. The projectile hadron undergoes successive collisions with target nucleons, and finally fragments into hadrons. On the other hand the created hadronic chains, whose number is equal to the number of collisions, fragment into hadrons.

It is necessary to determine dynamical properties of a hadron-nucleon collision in nucleus. Following refs.[2] and [9], we parametrise the kernel function K(x), which is a probability that the outgoing leading hadron has the light-like momentum fraction x after a collision, as;

$$K(x) = \alpha x^{\alpha-1}. \qquad (4.6)$$

The parameter α contains all the dynamical information in MCM. It means that the average fractional momentum of the leading hadron per a collision is equal to $1/(1+\alpha)$.

4.2 MONTE CARLO EVENT GENERATOR MCMHA

4.2.1 Basic Structure

Following refs. [2] and [9], we have constructed the Monte Carlo event generator MCMHA. MCMHA consists of four parts, which have the following functions (fig.4-2):

1. Determine the number ν of inelastic collisions of the incident hadron within a target nucleus A by the Glauber theory.

2. Fix the light-like momentum fraction x of the leading system and the charge transfer in an inelastic collision with a target nucleon.

3. Determine the hadron multiplicity and x's of secondary particles for the fragmentation of a chain into hadrons.

4. Include the intranuclear cascade of secondary particles inside the target nucleus. In this procedure, the formation zone concept [8, 10] is properly considered.

4.2.2 Determination Of Number Of Collisions

The probability, $P(\nu,\Delta b)$, that the incident hadron hits the target nucleus with an impact parameter between b and b+Δb and interacts ν times with nucleons in the target A is expressed by using the Glauber formula [11] as follows:

$$P(\nu,\Delta b)=$$

$$\int_{\Delta b} d^2b \binom{A}{\nu} (N_A(b)/A)^{\nu} (1-N_A(b)/A)^{A-\nu} / \sigma_{in}^{hA}(A,\Delta b) \qquad (4.7)$$

and

$$\sigma_{in}^{hA}(A,\Delta b)=\int_{\Delta b} d^2b \{1-(1-N_A(b)/A)^A\} \qquad (4.8)$$

In eqs.(4.7) and (4.8), $N_A(b)/A$ is the average probability of occurrence of an interaction between a target nucleon and a projectile hadron at impact parameter b and $N_A(b)$ is given by

$$N_A(b)=\sigma_{in}^{NN}\int dz\rho_A(z,b). \qquad (4.9)$$

Here, $\rho_A(z,b)$ is the nuclear density function expressed by the Woods-Saxon form;

$$\rho_A(r)=\bar{\rho}_A/\{1+\exp(r-R_A)/d\}. \qquad (4.10)$$

$\bar{\rho}_A$ is a normalisation constant such that

$$A=\int dr\rho_A(r) \qquad (4.11)$$

We took the parameters as follows [9];

$$R_A=1.19A^{1/3}-1.61A^{-1/3} \text{ fm} \qquad (4.12)$$

$$d = 0.54 \text{ fm}. \qquad (4.13)$$

We chose σ_{in}^{NN}=32 mb as the inelastic cross section of nucleon-nucleon interactions.

In practice, we have computed the probability of getting ν inelastic collisions within A at any impact parameter b according to eq.(4.7) by fixing the bin of b with Δb=1 fm in eq.(4.8) and by taking ν=15 as the maximum number of collisions.

4.2.3 Multiple Collision Process

In the second part, we determine the light-like momentum fraction x of the outgoing leading system after a collision and the energy $\hat{s}=(1-x)s=2m_NE(1-x)$ that is left for a chain to produce pions and to recoil a target nucleon. Following the MCM, x and $\hat{s}$ can be fixed by the kernel function K(x) (eq.(4.6));

$$K(x) = \alpha x^{\alpha-1}. \qquad (4.6)$$

α is the only one parameter apearing the model. We took α=3 according to ref.[9], because this value reproduces very well the proton spectra of p-A collision at 100 GeV/c [12]. It should be remarked that the spectrum of the leading proton, which appears as a fragment of the leading system after the final collision, is fixed by using the N-N collision data itself. Therefore, we took $\alpha=1$ only for the final collision.

For the chains produced by multiple collisions, we have to fix the total charge of each chain. We assume that the leading system interacts with a target proton (neutron) with the probability of "Z"/"A" (1-"Z"/"A"). Here, "Z" ("A") is the number of protons (nucleons) which are still left in the nucleus without suffering a collision up to previous interactions.

It is assumed that the leading system transfers its charge with the probability of $(1-r_c)$. We took $r_c=0.6$. And we took the same probability for the charge transfer of a target nucleon. In this way the net charge and x of each chain are determined.

4.2.4 The Chain Fragmentation

The average multiplicity <n> of hadrons from a chain is determined by the formula:

$$\langle n\rangle = 1.5\langle n_{ch}\rangle, \qquad (4.14)$$

with the assumption of charge independence and

$$\langle n_{ch}\rangle=0.57 + 0.584 \ln\hat{s} + 0.127 \ln^2\hat{s}, \qquad (4.15)$$

where the parametrisation is taken from ref.[13]. The total multiplicity n of this chain is generated according to the KNO distribution [14] with the mean value of <n>. All hadrons from the chain fragmentation are assumed to be pions and a recoil target nucleon.

The configuration of π^+, π^- and π^o is determined by the Orfandis-Rittenberg statistical model under the charge conservation law [15]. The model has the following assumptions;

- only two-body decays occur along the chain producing always a pion and another fireball.
- fireball can never be doubly charged (no exotic quantum number).

The chain first emits π^+ (π^-) if the primary net charge of a chain is +2 (-2). For any case, we can determine the pion configuration by the statistical model.

At the next step, the x of recoil nucleon is firstly determined and the x's of pions from the chain fragmentation are generated. The particle distribution of a single chain [2] is parametrised as

$$G(x,x_-) \propto (1-x)^{\beta}(1-x_-)^{\gamma}. \qquad (4.16)$$

We put $\beta=\gamma=3.0$. The ordering of the fragmentation of pions is determined in proportion to the remaining number of π^+, π^- and π^o.

4.2.5 The Cascade Process

We consider the intranuclear cascade processes of secondary particles produced by multiple collisions and chain fragmentations. (Hereafter, we call them the first generation particles.) Our cascade simulation is based on the following assumptions;

- The formation zone concept is properly taken into account. After a certain formation time the secondary particles are hadronised. If the secondary particle exists in the nucleus after the hadronization, it may interact with a nucleon in the nucleus.

- The cascade process is treated in one dimension, which is the direction of the incident particle.

- Only the first generation particle can interact with a nucleon in the nucleus successively but the recoil particles produced by the interaction (the second generation particles) cannot do.

- Both of elastic and inelastic interaction are treated. Only Δ production is considered as inelastic channel.

The sketch of cascade process is shown in fig.4-3 and its flow chart in fig.4-4. Four parts in the flow chart have the following functions;

1. Set initial states, which are interaction point, hadronization point, potential length (L) and unit cell length (l).

2. Check whether or not the first generation particle has enough conditions to continue the cascade process.

3. Go to the next cell and check whether it interacts with a nucleon in the nucleus.

4. Fix the interaction type and parameters of particles after the collision.

At the first step, we fix the position of the multiple collision of the projectile according to the Woods-Saxon nuclear density $\rho_A(z,b)$ (eq.(4.10)) and compute the value z_{max} of both ends of nucleus in z-direction at the impact parameter b fixed in the previous step. We get the momentum p of the first generation particle after the chain fragmentation as described in 4.2.4 and compute its formation zone l_f. We assume that the proper time of the formation zone, l_f^o, has the normal distribution with the mean value of 1 fm and the standard deviation of 0.3 fm in the rest frame of the particle [16]. Therefore the formation time, l_f, in the laboratory system is as follows;

$$l_f = l_f^o \times p/m,$$

where m is its rest mass. We can calculate the potential length L, through which the particle passes before leaving out of the nucleus. If a particle has positive potential length, it can interact with a nucleon in the nucleus. In order to investigate whether it interacts with a nucleon or not, the potential length is divided into unit cells of length l. It is proper that the unit cell length corresponds to the length in which there is a nucleon. Therefore, the unit cell length l and the cross section σ_{cell} for a unit cell are

$$l = L/A' \tag{4.17}$$

and

$$\sigma_{cell}(p_{in})=\sigma_{tot}^{hh}(p_{in})t(b), \tag{4.18}$$

where

$$A' = \int_L dz\rho_A(z,b), \tag{4.19}$$

$$t(b) = [\int_l dz\rho_A(z,b)]/A', \tag{4.20}$$

and $\sigma_{tot}^{hh}(p_{in})$ is the total cross section for the reaction hh at the incident momentum p_{in}. In practice, we calculate the values of eqs.(4.17) and (4.20) by following formula;

$$l \cong 2z_{max}/A \tag{4.21}$$

$$t(b) \cong [\int_{-zmax}^{zmax} dz\rho_A(b,z)]/A. \tag{4.22}$$

After setting the initial conditions, we check whether or not we can step further the cascade procedure for this particle. The cascade procedure is stopped if the first generation particle satisfies at least one of the following conditions;

- Outside the nucleus (i.e. $L < 0$).
- Its momentum is less than 0.07 GeV/c for pions and 0.25 GeV/c for nucleons.

At the next step, the first generation particle goes forward cell by cell checking whether there is a certain reaction or not. We consider protons and neutrons as target nucleons with the probability of Z/A and (1-Z/A), respectively. We assume the equalities of charge conjugate cross sections:

$\sigma(\pi^+p) = \sigma(\pi^-n)$ (fig.4-5a)

$\sigma(\pi^-p) = \sigma(\pi^+n)$ (fig.4-5b)

$\sigma(pp) = \sigma(nn)$ (fig.4-5c)

$\sigma(pn) = \sigma(np)$ (fig.4-5d)

The momentum dependences of cross sections are derived from the compilations of experimental data [17], which are presented in fig.4-5a, 4-5b, 4-5c and 4-5d, respectively. Since we do not have data for the π^o reactions, we get the cross section of $\pi^o p(n)$ as the average of those of $\pi^+p(n)$ and $\pi^-p(n)$.

When the first generation particle interacts with a nucleon, we have to fix the type of reaction and momenta of particles after the reaction. We also use the experimental data for determining the probability as to whether this reaction is elastic or inelastic (fig.4-6). The experimental distributions of four-momentum transfer squared t of elastic channels for various incident energies are available in the literatures [18]. We have fitted these experimental data to the following expression [17];

$$d\sigma/dt \propto \exp(-b(p_{in})t), \quad (4.23)$$

where $b(p_{in})$ is the slope parameter at the incident momentum p_{in}. The momentum dependence of $b(p_{in})$ is shown in fig.4-7a, 4-7b, 4-7c and 4-7d. We assumed that $b(p_{in})$ is same value both for elastic and inelastic reaction [17]. The momentum of particle after an interaction is determined by using the fitted slope parameters. We used the same method as that for the cross section in order to get the slope parameters of π^o incident channels.

We summarise the probabilities of inelastic channels in Table 4-1 and the decay modes of Δ in Table 4-2, respectively. In order to simplify the procedure for inelastic channels, we make two assumptions;

- The channels with charge transfer ≥ 2 are forbidden.
- Δ decays isotropically in its rest system.

With the above procedure we can fix the momenta of the first and the second generation particles, which are a recoil nucleon and particles decaying from Δ, and we continue the procedure for the first generation particle by going to the next cell.

This cascade process is applied to all the secondary particles from the chain fragmentation. So the kinematical variables of all particles from h-A collisions are completely fixed on the basis of the formation zone concept.

4.3 COMPARISON WITH OTHER EXPERIMENTAL DATA

4.3.1 Comparison With Pp Interactions

In order to confirm the adequacy of MCMHA, we try first to compare MCMHA with experimental data of pp interactions, which are the simplest p-A interactions. The rapidity distribution of shower particles for pp collisions at 360 GeV/c is shown in fig.4-8 with the result of MCMHA. These experimental data come from the experiment NA23 part A. MCMHA explains the global feature of experimental data satisfactorily.

Concerning the multiplicity distribution, mean charged multiplicity of 360 GeV/c pp interactions is 9.06 [19], while 8.6 by MCMHA.

We thus confirm the consistency between the experimental data and MCMHA results for 360 GeV/c pp interactions.

4.3.2 Comparison With Streamer-Chamber Experiment At 200 GeV/c

Experimental results for 200 GeV/c proton-nucleus (p, Ar and Xe) collisions [19] have been obtained from the experiment with a streamer-chamber, which is a visible vertex chamber similar to a bubble chamber. In fig.4-9(a) and (b) the rapidity distributions of shower particles are displayed for p-Ar and p-Xe collisions, respectively. Histograms in these figures represent the results of MCMHA. Comparing both results, we can find that MCMHA describes a global feature of experimental results in the whole rapidity range for both p-Ar and p-Xe collisions.

In order to avoid the influences from particle misidentification and particle selection, we investigate the rapidity ratio of p-Xe to p-p collisions (fig.4-10). This quantity is useful to see the effect of intranuclear cascade. In fig.4-10, the results of MCMHA with and without the cascade process are represented by the histogram and solid curve, respectively. MCMHA without the cascade process shows a slight increase but there is a discrepancy with experimental results in the region of $y < 2$, while MCMHA with the cascade process describes a sudden increase in the same region.

4.3.3 Comparison With Bubble Chamber Experiment At 100 GeV/c

The multiplicity distribution of shower particles is shown in fig.4-11 for 100 GeV/c p-Au collisions with the bubble chamber [20]. The solid line in this figure represents the result of MCMHA including the cascade process. MCMHA describes a global feature of the multiplicity distribution for 100 GeV/c p-Au collisions very well.

On the other hand the result of MCMHA without the cascade process is shown by a dotted line. Also the dot-dashed line is the KNO scaling curve [14] for this distribution. When we compare the experimental data with the KNO scaling curve, we recognise that there is a larger discrepancy between them, particularly in the region of < 20 prongs. Comparing the two cases of MCMHA, that is, with and without the cascade process, the latter is in disagreement with experimental data, especially in the high multiplicity region of larger than 10 prongs.

Concerning the multiplicity and rapidity distributions, we can confirm the consistency of MCMHA including the cascade process with the experimental data.

Reference to Chapter 4

[1] A. Capella and A. Krzwicki, Phys. Lett. 67B (1977) 84

[2] K. Kinoshita, A. Minaka and H. Sumiyoshi, Prog. Theor. Phys. 61 (1979) 165; ibid 63 (1980) 928

[3] A. Capella and J. Tran Thanh Van, Z. Phys. C 10 (1981) 248

[4] V. V. Anisovich, Yu. M. Shbelshy and V. M. Shekhter, Nucl. Phys. B133 (1978) 477

[5] A. Białas and E. Białas, Phys. Rev. D20 (1979) 2854

[6] A. Białas and W. Czyz, Nucl. Phys. 194 (1982) 21

[7] F. Takagi, Prog. Theor. Phys. 65 (1981) 1350; Phys. Rev. D27 (1983) 1461

[8] N. N. Nikolaev, Sov. J. Part. 12 (1981) 63

[9] S. Daté, M. Gyulassy and H. Sumiyoshi, Phys. Rev. D32 (1985) 619

[10] O. V. Kancheli, JETP Lett. 18 (1973) 274

[11] R. J. Glauber, in "Lecture in Theoretical Physics", edited by W.E.Brittin and L.G.Dunham (Interscience, New York, 1959) Vol.1, p315

[12] A. Barton et al, Phys. Rev. D27 (1983) 2580

[13] G. Matthiae, Proc. High Energy Phys. Conf. Brighton (1983) p714

[14] P. Slattery, Phys. Rev. Lett. 29 (1971) 1624

[15] S. J. Orfandis and V. Rittenberg, Nucl. Phys. B59 (1973) 570

[16] A. Białas, CERN preprint TH-3765 (1983)

[17] S. Yamazaki, Master Thesis of Tokyo Metropolitan Univ. (1986)

[18] For pp and pn interactions, Particle Data Group, NN and ND Interactions [Above 0.5 GeV/c] - A Compilation
For π^+- and π^--p interactions, J. Deahl et al, Phys. Rev. 124 (1961) 1987 ; C. D. Wood et al, Phys. Rev. Lett. 6 (1961) 481 ; S. Kellman et al, Phys. Rev. 129 (1963) 365 ; J. A. Helland et al Phys. Rev. 134 (1964) 1062 ; J. A. Helland et al, Phys. Rev. 134 (1964) 1079 ; P. M. Ogden et al, Phys. Rev. 137 (1965) 1115 ; W. Troka et al, Phys. Rev. 144 (1966) 1115 ; C. T. Coffin et al, Phys. Rev. 159 (1967) 1169 ; S. L. Baker et al, Nucl. Phys. B18 (1970) 29 ; G. E. Kalmus et al, Phys. Rev. D4 (1971) 676 ; M. G. Bowler et al, Nucl. Phys. B37 (1972) 133 ; M. G. Albrow et al, Nucl. Phys. 37 (1972) 594

[19] J. L. Bailly et al, Z. Physik C23 (1984) 205

[20] C. De Marzo et al, Phys. Rev. D26 (1982) 1019

[21] N. N. Biswas et al, Phys. Rev. D33 (1986) 3167

CHAPTER 5

PROTON-NUCLEUS COLLISIONS

5.1 THE BACKGROUND AND CROSS SECTION

5.1.1 Background Estimations

The main background of foil interactions was the contamination from proton-proton interactions. This mostly came from two sources; i.e. the ambiguity on the determination of primary vertices, especially in z, and the ambiguity on the positioning of foil targets.

The errors of vertex reconstruction were $\Delta x \cong 110$, $\Delta y \cong 60$ and $\Delta z \cong 400$ μm. The influences from the errors in x and y were minor, however the error in z affected the determination of the foil region. Due to these reasons we have to define the region of foil targets thicker than real ones. The defined foil region had the thickness of 2 mm (x-direction) though the real thickness of Al and Au was 1.6 mm and 0.3 mm, respectively.

In order to estimate the contaminations from pp interactions, we needed the scanning data of not only foil interactions but also normal pp interactions. Therefore we had to limit the data sample to three rolls (roll number is 57, 59 and 67), whose scan data have been obtained in Tokyo. The beam profile of the pp interactions (Event class = 0) in y-z plane is displayed in fig.5-1. It is clear from fig.5-1 that only about 20 % of beam protons hit the foil targets. The number of normal pp interactions, whose (y,z)-positions are inside the target region and x-positions of primary vertices are inside the scan fiducial volume, are listed in Table 5-1 roll by roll in order to see the possible change of beam profile.

The scan fiducial volume was 65 cm along the x-axis in the scanning convention. Assuming the uniform distribution of pp events along the x-axis within the scan fiducial volume, we have investigated the contaminations from pp interactions to foil interactions. The results are also presented in Table 5-1. The contaminations to foil events thus obtained were ≅2.3 % for p-Al interactions and ≅12.5 % for p-Au interactions, respectively. The total number of pp interactions which were contaminated in the sample of foil interactions used in the current analysis was estimated to be 1.07 ± 1.03 and 24.0 ± 4.9 events for p-Al and p-Au collisions, respectively when the beam profile was assumed to have remained unchanged during the run.

5.1.2 The Cross Sections

We have estimated the total cross sections of p-Al and p-Au collisions to confirm the consistency with results of other experiments. In order to obtain the sample of pure foil interactions we used the foil interactions satisfying the following condition:

$-0.75 \leq z \leq -0.10.$

We inferred that the contaminations of this sample were ≅1.2 % and ≅6.9 % for p-Al and p-Au interactions, respectively.

The interaction cross section can be written as

$$\sigma_i = \frac{N_i}{n_i t_i (A/M_i) \rho_i} \qquad (5.1)$$

where,

N_i = the number of interactions in the i-target,

n_i = the number of beam protons which hit the i-target,

t_i = the effective thickness of the i-target,

A = the Avogadro's number,

M_i = the atomic weight of the i-target and

ρ_i = the density of the i-target,

for i = Al or Au.

In order to derive the number of incident beams n_i in eq.(5.1) which passed through the i-target, we have used the following equation:

$$\sigma_i^p(\geq 4\text{prongs}) = \frac{N_i^p}{n_i L A \rho_H} \qquad (5.2)$$

where,

$\sigma_i^p(\geq 4\text{prongs})$ is the pp interaction cross section with charged multiplicity $\geq$ 4 obtained by our experiment (30.7 mb) [1] at 360 GeV/c.

N_i^p is the number of pp interactions with charged multiplicity

$\geq$ 4, with (y,z)-position of the beam inside the i-target region and with x-position of vertex inside the scan fiducial volume,

L is the fiducial length along the x-axis (65 cm) and

ρ_H is the density of liquid hydrogen (0.063 g/cm^3).

The number of events with charged multiplicity of $\geq$ 4 was used in order to avoid the trigger inefficiency for the lower multiplicity events [1]. The number of pp interactions with multiplicity $\geq$ 4, N_i^p, is listed in Table 5-2.

Using the corrected number of foil interactions and the number of pp interactions with multiplicity $\geq$ 4, we have obtained the cross sections of p-Al and p-Au interactions as:

$$\sigma_{Al} = 400 \pm 120 \text{ mb and}$$

$$\sigma_{Au} = 1500 \pm 300 \text{ mb.}$$

The errors are only the statistical ones.

These results are compared in fig.5-2 with measurements of other experiments [2][3][4], which were done with 280 GeV/c, 300 GeV/c and 200 GeV/c incident protons respectively. Despite of large errors, the cross sections obtained from this sample are in good agreement with others.

The mean number of inelastic collisions $\bar{\nu}$ in the p-nucleus interactions is given by

$$\bar{\nu} = A\sigma_p/\sigma_A \qquad (5.3)$$

where A is the mass number of the target nucleus, and σ_p and σ_A are the cross sections on proton and nucleus, respectively. Using σ_p = 32.8 mb obtained by the experiment NA23 part A [1] we have obtained the mean number of collisions $\bar{\nu}$ for p-Al and p-Au interactions:

$\bar{\nu}_{Al} = 2.2 \pm 0.7$ and

$\bar{\nu}_{Au} = 4.3 \pm 0.9$.

5.2 MULTIPLICITY DISTRIBUTIONS

In the following n_g denotes the number of identified gray particles in the scanning (see section 3.2). This number is not identical to the number of gray tracks measured in emulsion experiments, however it characterizes the events in a similar way [4][5]. We used the values from scanning data not from Geometry Summary Tape (GST), because of the reconstruction losses. An n_s indicates the number of shower particles. The number of positive and negative shower particles comes from GST.

5.2.1 Total Charged Multiplicity Distributions

The total charged multiplicity distributions of p-Al and p-Au interactions are shown in fig.5-3. The dot-dashed lines represent Koba-Nielson-Olesen (KNO) distribution [6] for the observed mean multiplicity $\langle n\rangle$. The parametrisation was obtained by a phenomenological fit to the multiplicity distributions of pp interactions at different energies [7]:

$$\Psi(z)=\langle n\rangle\sigma_n/\sigma_{inel}$$
$$=(3.79z + 33.7z^3 - 6.64z^5 + 0.332z^7)\exp(-3.04z)$$

(5.4)

where $z=n/\langle n\rangle$, σ_n is the topological cross section and $\sigma_{inel}=\Sigma\sigma_n$. Dotted lines in fig.5-3 show the results of the Monte Carlo event generator MCMHA.

The mean charged multiplicities are:

17.7 ± 1.5 for p-Al and

28.2 ± 1.3 for p-Au collisions.

The MCMHA predicted mean multiplicities of 15.9 for p-Al and 26.7 for p-Au collisions, respectively. The KNO distribution agrees with the total charged multiplicity distribution of p-Al events, but the agreement is poor for p-Au events. On the other hand MCMHA describes total charged multiplicity distributions for both p-Al and p-Au interactions.

5.2.2 Gray Multiplicity Distributions

Fig.5-4 shows the gray multiplicity distributions of p-Al and p-Au interactions. The dashed lines in fig.5-4 were calculated by the model of Hegab and Hufner [8]. The histograms represent the results of MCMHA. The mean gray multiplicities are:

1.9 ± 0.5 for p-Al and

4.6 ± 0.4 for p-Au collisions.

The mean gray multiplicities predicted by the model of Hegab and Hufner are:

1.69 for p-Al and

4.63 for p-Au interactions.

The model of Hegab and Hufner describes well these experimental results. MCMHA is in better agreement with both distributions of p-Al and p-Au interactions.

5.2.3 Shower Multiplicity Distributions

In fig.5-5(a),(b) the multiplicity distributions are shown for all shower particles, in fig.5-5(c),(d) for positive shower particles and in fig.5-5(e),(f) for negative shower particles. The dot-dashed lines represent KNO distributions and the dotted lines are results of MCMHA. The predictions with the model of Kiang et al [9], which proposed the universal KNO scaling at each impact parameter, are shown with the solid line in fig.5-5(a),(b). The mean shower multiplicity $\langle n_s \rangle$ is as follows:

15.7 ± 1.3 for p-Al and

23.6 ± 1.1 for p-Au collisions.

The KNO distribution is consistent with all distributions of shower particles for p-Al interactions. However, it does not give a good agreement with those for p-Au interactions, especially those of all and positive shower particles. MCMHA explains the behaviour of the multiplicity distributions better than the KNO distribution. On the other hand the model of modified KNO scaling [9] reproduces the shower multiplicity of both p-Al and p-Au collisions in the whole region.

Table 5-3 summarises the averaged multiplicity $\langle n \rangle$ and the dispersion $D=[\langle (n - \langle n \rangle)^2 \rangle]^{1/2}$ of multiplicity distributions for p-Al and p-Au interactions.

Fig.5-6 shows the dispersion D as a function of $\langle n \rangle$ for negative shower particles. The straight lines show the Wroblewski relation [10] for pp interactions:

$$D = 2D_- = 0.576(\langle n_s\rangle - 1) \qquad (5.5)$$

$$n_s = 2n_- + 2 \qquad (5.6)$$

We can find that experimental data for both nuclear and elementary targets are in good agreement with the relation of pp interactions.

Fig.5-7 shows the ratio $R_A = \langle n_s\rangle/\langle n\rangle_{pp}$ as a function of $\bar{\nu}_A$, where $\langle n\rangle_{pp}$ is the mean charged multiplicity of pp interactions which is obtained to be $\langle n\rangle_{pp} = 9.06 \pm 0.09$ for 360 GeV/c pp collisions [1]. A straight line $R_A = (1/2)(\bar{\nu}_A + 1)$ is also shown in the figure for comparison. We have found that the relation between R_A and $\bar{\nu}_A$ is linear, which was also reported by other experiments [4][11].

5.2.4 Comparison Of Experimental Results With MCMHA.

The mean multiplicity $\langle n\rangle$ and the dispersion D obtained by MCMHA are also listed in Table 5-3 with experimental results. In general, MCMHA describes well the multiplicity distributions of this experiment. Particularly, the total charged and gray multiplicity distributions of MCMHA agree well with experimental distributions. MCMHA properly represents the behaviour of experimental data in high multiplicity region. However, in the low multiplicity region of total charged and shower multiplicity distributions MCMHA exhibits a little difference from experimental data. We can find that MCMHA is generally in agreement with experimental results better for p-Au than for p-Al collisions.

5.3 GRAY PARTICLES

5.3.1 Gray Particle Identification

Gray particles are considered to be protons knocked-out by an incident hadron and/or secondary particles, which are produced by primary collisions between the incident hadron and a nucleon in the nucleus. Furthermore the excited debris of target nucleus are produced after the projectile passed through and they evaporate gray or black particles until they reach to the ground state.

We classified the reconstructed gray tracks into the following types:

type I: stopping gray tracks in RCBC with momenta computed from the curvatures of fitted circles,

type II: non-stopping gray tracks in RCBC, and

type III: stopping gray tracks in RCBC without momenta from curvatures because of very short tracks (two-point tracks).

Gray particles classified as type I can be identified by the relation between range and momentum. Fig.5-8(a) displays the momentum calculated by its curvature and the range for the gray particles of type I with the momentum resolution of $\Delta p/p < 0.20$. In fig.5-8(a) two broken lines represent range-momentum relation in the liquid hydrogen for proton and deuteron, respectively. We can find two clusterings of data points around broken lines in this figure. In order to make this fact clearer, the projection of data points onto the axis perpendicular to the broken line is shown in fig.5-8(b). This histogram was fitted to the superposition of two Gaussian distributions. As a result, the scatter plot was divided into three regions. We have recognised the tracks belonging to the left region as protons, the middle one as deuterons and the right one as heavier particles which are tritons and alpha particles. This separation was expressed as follows:

$R > 648P^{3.628}$ for proton,

$648P^{3.628} > R > 99P^{3.628}$ for deuteron and

$R < 99P^{3.628}$ for triton or alpha,

where R is the range in the unit of cm and P is the momentum calculated by curvature in GeV/c.

Concerning gray particles of type II, we did not find any good measures on particle identification. However, these gray particles had the average momentum of ≅500 MeV/c. If these particles are deuterons, most of them must stop in RCBC because they have the ranges of 10-20 cm. Therefore, we have identified gray particles of type II as protons.

Only the range was known for the gray particles of type III. We assumed those tracks to be protons. If its momentum was less than 150 MeV/c, we have identified it as deuteron.

According to the above criteria, we have done the identification of all gray particles. The results are listed in Table 5-4. While the number of produced deuterons per event is ≅0.17 ± 0.10 and ≅0.47 ± 0.07 for p-Al and p-Au collisions, respectively, the ratios of the number of identified deuterons to that of all gray particles were ≅12 % and ≅14 % for p-Al and p-Au collisions respectively. This fact is very interesting. It suggests that there is an independent process on the number of collisions in the production mechanism of gray particles for various nuclei. On the other hand, the ratios of heavier particles are 4 % and 8 % for p-Al and p-Au interactions respectively. One may say that heavier particles are produced more likely in p-Au collisions than in p-Al collisions.

5.3.2 Angular Distributions

We can obtain some information on gray particle production mechanism from its angular distributions. Fig.5-9(a) shows the gray particle density as a function of θ for p-Al and p-Au interactions, where θ is the laboratory angle between beam and the gray particle. The same plot of the deuteron density for p-Au collisions is shown in fig.5-9(b). The dip near $\cos\theta = 0$ of the deuteron distribution should be considered experimental in origin. The gray particles emitted in the angular region near $\cos\theta = 0$ do not appear out of the shade of foil targets and can not be reconstructed. Therefore we should consider that they have a large uncertainty in this region.

It seems that the distributions in fig.5-9(a) consist of two components for each target nucleus. One of them is the nuclear evaporation products produced isotropically and the other is the recoil products produced predominantly forward in laboratory. From fig.5-9(b) one can see that deuterons are produced isotropically, while there is an excess of the gray particles produced forward.

5.3.3 Momentum Distributions

Fig.5-10(a) and (b) represent the momentum distributions of gray particles for p-Al and p-Au interactions, respectively. The results from MCMHA are also shown in these figures with histogram. The average momentum of gray particles is ≅430 MeV/c and ≅440 MeV/c for p-Al and p-Au events respectively, and that of MCMHA is ≅440 MeV/c and ≅450 MeV/c for p-Al and p-Au events, respectively.

The momentum distributions seem roughly independent of the nuclear target. The distribution obtained from MCMHA explains well the global feature of the experimental data although there is a little discrepancy in the low momentum region of < 0.2 GeV/c. This discrepancy mainly seems to be due to the detection loss by the shade of targets and to the uncertainty of the correction in MCMHA for targets. Indeed most of particles in this low momentum region are two-point tracks and they have many uncertainties.

5.3.4 Energy Spectrum

The invariant energy spectra are shown in fig.5-11(a) and (b) for p-Al and p-Au collisions. We analysed them using a moving-source model [12][13]. In this model gray particles were assumed to be isotropically emitted from a moving source. We assumed that these spectra are approximately represented at all angles by the following expression:

$$\frac{dN}{pdT} = N_o \exp(-T/E_o) \qquad (5.7)$$

where T is the kinematic energy in laboratory system and E_o is the slope parameter, which corresponds to the temperature of the moving source. The dot-dashed lines in fig.5-11 show the fit to data by the single-moving-source model of the equation (5.7). The slope parameters obtained in this case are the follows:

E_o = 85 ± 8 MeV for p-Al and

E_o = 65 ± 3 MeV for p-Au collisions.

One can see the difference between the fitted line and data in the region of T > 500 MeV, while the single-moving-source model is in good agreement with experimental data in T < 300 MeV. Assuming two moving sources we made a fit to data in the whole range with the following equation:

$$\frac{dN}{pdT} = N_o^s \exp(-T/E_o^s) + N_o^f \exp(-T/E_o^f) \qquad (5.8)$$

where E_o^s and E_o^f are the slope parameters of each moving source and the superscripts "s" and "f" correspond to the "slow" and "fast" sources. The two-moving-source model fits are expressed by solid lines in the figures and the dashed lines show the fit to the component of the "fast" source with the slope parameter E_o^f. The slope parameters obtained in this case have the following values:

E_o^s = 51 ± 24 MeV,

E_o^f = 176 ± 133 MeV for p-Al

and

E_o^s = 53 ± 8 MeV,

E_o^f = 135 ± 40 MeV for p-Au collisions.

Table 5-5 summarises the fitting to experimental data by the moving-source model. It is very interesting to see that each slope parameter coincides with the value obtained from the low energy region [14], where the slope parameters at an incident momentum of 4 GeV/c were determined to be:

$$E_o^s = 57 \text{ MeV},$$
$$E_o^f = 117 \text{ MeV} \qquad \text{for p-Al}$$

and

$$E_o^s = 52 \text{ MeV},$$
$$E_o^f = 116 \text{ MeV} \qquad \text{for p-Pb interactions.}$$

The independence of the slope parameters on target nuclei seems to correspond to the fact that the ratio of the produced deuterons to the produced gray particles is almost independent on kinds of target. Furthermore, the better fitting by the two-moving-source model confirms the hypothesis obtained from the angular distributions that there are two components in gray particles.

5.4 SHOWER PARTICLE ANALYSIS

In the following analysis we have added a condition that the incident beam should successfully be hybridised. As a result, number of events is;

46 events for p-Al and

179 events for p-Au interactions.

5.4.1 Leading Particles

It is one of main objects to estimate the baryon stopping power of nuclear matter. It seems to be useful to investigate the degradation of an incident proton momentum in the nucleus. We define the variable X as the total momentum divided by the incident beam momentum. This X is a little different from the Feynman x. Fig.5-12 (a) and (b) show the X distribution for p-Al and p-Au collisions. In these figures the horizontal-axis represents the leading number n, which expresses the particle with the n'th highest momentum and the vertical-axis the mean value of X of the particle with the leading number n. The squares and crosses correspond to the events in which the fastest particle is positive and negative, respectively, and a histogram represents all events. One can see that the X of the fastest particle is different from those of others. On the other hand the mean values of X of the particles other than the fastest one are rather alike.

"Leading particle" is defined as the fastest positive particle and assumed to be protons in the following analysis. The rapidity shift from the beam rapidity for leading particles is shown in fig.5-13 (a) and (b) on p-Al and p-Au collisions, respectively. Histograms in the figures represent predictions by MCMHA. The solid histograms correspond to the particles which satisfy the definition of the "leading particle", while the dashed histograms show contributions from protons. The rapidity shifts of most of leading particles are upto -4 and their mean values are about -1.9 and -2.3 for p-Al and p-Au interactions, respectively. The mean values of MCMHA are -1.9 and -2.1 for p-Al and p-Au collisions, respectively. These features are in good agreement with the results of MCMHA.

5.4.2 Rapidity Distributions

In the laboratory system the rapidity is defined as

$$y = (1/2)\ln(E+p_L)/(E-p_L). \qquad (5.9)$$

The rapidity distributions were measured in the full rapidity range from -2 to 8. The rapidity density $\rho(y)$ is defined as follows;

$$\rho(y) = \frac{1}{N_{ev}} \frac{dN}{dy} \qquad (5.10)$$

where N_{ev} is the number of events and N the number of particles in the rapidity interval. The rapidity density distributions for all shower particles, for positive and negative shower particles in p-Al and p-Au collisions are shown in figs.5-14 (a)-(f).

The histograms in the figures correspond to predictions of MCMHA in which the cascade process is included. For all shower particles, the predictions of MCMHA agree with the measured distributions. The dip near $y = 0$ is a reflection of the one-dimensional treatment of the cascade process.

In order to avoid the effect of particle misidentification for the rapidity distributions, we investigated the rapidity ratio R(y) defined by

$$R(y) = \rho_A(y)/\rho_p(y), \qquad (5.11)$$

where $\rho_A(y)$ and $\rho_p(y)$ are the rapidity density distributions for p-A (A=Al,Au) and p-p collisions, respectively. In R(y) the particle misidentification seems to be canceled because it is approximately the same in p-p as in p-A interactions.

Fig.5-15 shows the ratio R(y) as a function of y for p-Al and p-Au interactions. The $\rho_p(y)$ came from the results of experiment NA23 part A. The common features of the presented ratio R(y) are as follows:

- Very large numbers in the target fragmentation region of $y < 1$. This is the evidence for the intranuclear cascade [4][5].

- Very slow decrease with increasing y in the rapidity region of $1 < y < 5$. This central plateau ($2 < y < 4$) for p-Au collisions is higher than for p-Al collisions. Its experimental ratio $R_{Au}(y)/R_{Al}(y)$ was 1.16 ± 0.40.

- In the projectile fragmentation region of $y > 5$, the ratio R(y) falls below unity and R(y) of p-Au falls faster than that of p-Al.

The histograms in the figures show the corresponding MCMHA predictions. The experimental results are in good agreement with the predictions of MCMHA, except near of y=0. The solid line shows the result of the Monte Carlo event generator FRITIOF [15] by Lund group, which is a model for low p_t hadronic collisions based on the notion of a hadron as a vortex line in a colour superconducting medium. Comparing the result of FRITIOF with experimental result, we can see the good agreement between them in the region of $y > 2$, while there is a significant difference in the region of $y < 1.5$.

One can see the central plateau in the region of $y > 2$. Therefore, the cascade process seems to become important in the region of $y < 2$ for both p-Al and p-Au collisions.

5.4.3 Invariant Cross Sections

Fig.5-16 (a) displays the invariant cross section $(x/\pi)d\sigma/dx$ of leading particles as a function of x for p-Al and p-Au interactions, respectively. At the same time we plotted the inclusive invariant differential cross sections for p+Al->p+X and p+Pb->p+X, which is an incident momentum of 100 GeV/c at the transverse momentum of 0.3 GeV/c [16].

Fig.5-16 (b) shows the invariant cross section of positive shower particles in the same way as above. Also the inclusive invariant differential cross sections for $p+Al \rightarrow \pi^{+}+X$ and $p+Pb \rightarrow \pi^{+}+X$ are shown in the figure [16].

In these figures, both experimental results indicate similar behaviour although these incident momenta are different.

5.4.4 Leading Rapidity Shift Correlations

Bubble chamber experiments allow us global analyses of p-A collisions. Therefore, we have studied correlations between the leading rapidity shift and other physical quantities.

Mean rapidity of other shower particles than the leading particle is shown in fig.5-17(a) and (b) as a function of the leading rapidity shift, Δy_B, for p-Al and p-Au collisions, respectively. In the same way, mean rapidity of other particles, including gray particles, is shown in fig.5-18(a) and (b). A histogram in each figure represents the result of MCMHA.

Experimental results about the rapidity correlations for both p-Al and p-Au collisions are summarised as follows:

- In the region near $\Delta y_B = 0$, mean rapidity of other (shower) particles shows the rapid increase of ≅0.0 to ≅2-3.

- In the region of $|\Delta y_B|<4$, mean rapidity of other (shower) particles is approximately constant.

- In the region of $|\Delta y_B|>4$, the larger the leading rapidity shift is the smaller mean rapidity of other (shower) particles is. The decrease of mean rapidity of other particles is faster than that of other shower particles.

Further, we can find that experimental results are in good agreement with MCMHA for both p-Al and p-Au collisions. About p-Au collisions, however, a small discrepancy between the experimental results and MCMHA can be seen in the region of $|\Delta y_B|>4$. In general the experimental values are smaller than MCMHA ones in this region.

Next, we show the multiplicity correlations in fig.5-19 and 5-20. Fig.5-19(a) and (b) display the mean shower multiplicity as a function of the leading rapidity shift, Δy_B, for p-Al and p-Au interactions, respectively. Similarly, fig.5-20(a) and (b) show the mean total multiplicity as a function of Δy_B for p-Al and p-Au collisions, respectively.

Concerning the multiplicity correlation, we can summarise the experimental results as follows:

- In $|\Delta y_B|<3$, the larger the leading rapidity shift is the larger the mean values of both shower and total multiplicity are.

- In $|\Delta y_B|>4$, the mean multiplicity shows a sudden decrease.

Comparing the shower multiplicity with the total multiplicity, we can find the followings;

- In the region of $|\Delta y_B|<3$, the mean total multiplicity is more than the mean shower multiplicity by ≅1.0 and ≅2.5 for p-Al and p-Au collisions, respectively. These values are smaller than mean values of each gray multiplicity.

- In the region of $|\Delta y_B|>4$, the mean total multiplicity is more than the mean shower multiplicity by ≅3 and ≅5 for p-Al and p-Au collisions, respectively.

Histograms in these figures represent the corresponding MCMHA results. MCMHA describes each multiplicity correlation very well.

According to both the rapidity and the multiplicity correlations, we are led to the following physical picture of multiparticle production in hadron-nucleus collisions;

- Most of the lost rapidity of an incident proton is spent by the particle production.

- The rapidity of each particle produced in h-A collisions is constant on the average independent of the lost rapidity.

Moreover, it seems that the mean gray multiplicity is linear for the leading rapidity shift and that we can use the gray multiplicity as the measures of the leading rapidity loss and also of the number of collisions.

5.5 NUCLEAR STOPPING POWER

The estimation of nuclear stopping power is one of the most interesting subjects for hadron-nucleus collisions. As mentioned in section 5.4.1, the degradation of an incident momentum in the nucleus is a good measure to investigate it. Thus we estimate the nuclear stopping power, especially for heavy nuclei, by using the X (see section 5.4.1).

In order to investigate the dependence of the nuclear stopping power upon the number of projectile collisions we estimate the number of collisions with relation to gray multiplicity, n_g, by MCMHA. Concerning p-Au collisions, the sample is divided to three subgroups as the following;

i) n_g = 0-1 $\bar{\nu} = 1.5 \pm 0.3$

ii) n_g = 2-5 $\bar{\nu} = 3.0 \pm 0.7$

iii) n_g >6 $\bar{\nu} = 5.4 \pm 1.5$

Fig.5-21 shows the mean of X of the fastest particle by a cross for each subgroup. The fastest particles can be positive or negative. On the other hand, selecting the events in which the fastest particle is positive the means of their X's are plotted in fig.5-21 by circles.

In the case of $\bar{\nu}$ = 1.5 the means of X are 0.26 and 0.29 for the case of all fastest particles and the case of positive fastest particles, respectively. There is a little difference between them. In the case of $\bar{\nu}$ = 3.0 and 5.4 there is no difference between both of them. Also one can find no difference between of $\bar{\nu}$ = 3.0 and 5.4. The mean X of $\bar{\nu}$ = 3.0 and 5.4 are 0.21 and 0.21 for all fastest particles, and 0.23 and 0.22 for positive fastest particles. These experimental results are consistent with those of R. J. Ledoux et al [17]. This fact suggests that a baryon traversing the central region of Au nucleus loses 80 % of its incident energy on the average.

Reference to Chapter 5

[1] J. L. Bailly et al, Z. Physik C23 (1984) 205

[2] A. S. Carrol et al, Phys. Lett. 80B (1979) 319

[3] S. A. Azimov et al, Phys. Rev. D23 (1981) 2512

[4] C. De Marzo et al, Phys. Rev. D26 (1982) 1019

[5] C. De Marzo et al, Phys. Rev. D29 (1984) 2476

[6] Z. Koba, N. B. Nielsen and P. Olesen, Nucl. Phys. B40 (1970) 317

[7] P. Slattery, Phys. Rev. Lett. 29 (1971) 1624

[8] M. K. Hegab and J. Hufner, Nucl. Phys. A384 (1982) 353

[9] D. Kiang, H. Ling, K. Young and C. S. Lam, Phys. Rev. 31 (1985) 31

[10] A. Wroblewski, Acta Phys. Pol. B4 (1973) 857

[11] J. E. Elias et al, Phys. Rev. D22 (1980) 13

[12] M. Meng Ta-Chung and E. Moeller, Phys. Rev. Lett. 41 (1978) 1352; I. G. Bogatskaya, C. B. Chiu, M. I. Gorenstein and G. M. Zinovjev, Phys. Rev. C22 (1980) 1992

[13] T.-A. Shibata et al, Nucl. Phys. 408 (1983) 525

[14] H. En'yo et al, Phys. Lett. 159B (1985) 1

[15] B. Andersson, G. Gustafson and B. Nilsson-Almqvist, Lund preprint LU-TP 86-3, 1986; B. Nilsson-Almoqvist and E. Stenlund, Lund preprint LUIP 8507/LU-TP 85-7, 1985

[16] D. S. Barton et al, Phys. Rev. D27 (1983) 2580

[17] R. J. Ledoux et al, presented at Gross Properties of Nuclei and Nuclear Excitation, International Workshop XIV, Hirschegg Austria, 1986

CHAPTER 6

SUMMARY AND CONCLUSIONS

In this thesis several aspects of multiparticle production of proton-nucleus collisions were described. The observed experimental results were compared with some models, especially the multichain model. Furthermore, the details of the Monte Carlo event generator MCMHA were presented, which is based on the multichain model and includes the intranuclear cascade process.

The data used in this analysis came from the CERN experiment NA23 part B. This was performed by using the Rapid Cycling Bubble Chamber (RCBC) with the European Hybrid Spectrometer (EHS) at CERN North Area with 360 GeV/c proton beams. Targets, aluminium and gold foils, were installed in the RCBC, which was filled with liquid hydrogen. Total 195000 events were triggered and 608 events selected as foil event candidates were measured and they were available as inputs to the geometry reconstruction program GEOHYB. Finally we have obtained 47 events as p-Al interactions and 192 events as p-Au interactions for the physics analysis.

The cross sections of p-Al and p-Au inelastic collisions at 360 GeV/c were investigated on the basis of the cross section of 360 GeV/c p-p collisions. They have been estimated to be (400±120) mb for p-Al and (1500±300) mb for p-Au collisions, respectively, and these values were consistent with those of other experiments.

We found 17.7±1.5 as the mean total charged multiplicity of p-Al and 28.2±1.3 for p-Au collisions. Also the mean gray multiplicity were found to be 1.9±0.5 for p-Al and 4.6±0.4 for p-Au collisions. Total and shower multiplicity distributions were compared with the KNO scaling distribution. The KNO scaling distribution described the multiplicity distributions for p-Al collisions, but some discrepancies were seen in p-Au collisions. The comparison between the shower multiplicity distribution and the model which assumed the universal KNO scaling at each impact parameter was done and good agreements were shown.

Gray particles were identified as a proton/deuteron/heavier particle using the information from reconstructed tracks. The number of deuterons produced per event was found to be 0.17±0.10 for p-Al and 0.47±0.07 for p-Au collisions, while ratio of the number of produced deuterons to all gray particles was about 10 % for both p-Al and p-Au collisions. Two components could be seen in the angular distribution of gray particles. One of them was the nuclear evaporation products produced isotropically, and the other was the recoil products predominantly produced forward. deuterons were produced isotropically.

The analysis of the energy spectrum of gray particles was performed on the basis of the moving-source model. With the two-moving-source model the temperatures of two moving sources were respectively found to be 51 and 176 MeV for p-Al and to be 53 and 135 MeV for p-Au collisions. The temperatures of two moving sources were independent on the target nucleus and on the incident energy.

The leading particle was defined as the fastest positive particle. The mean rapidity shifts of the leading particles from the beam rapidity were found to be -1.9 and -2.3 for p-Al and p-Au collisions, respectively. The mean rapidities of produced particles were 2.8 for p-Al and 2.4 for p-Au collisions respectively. The sudden increases in the rapidity density ratios of shower particles in p-A to p-p collisions have been observed in the target fragmentation region.

The correlations between the leading rapidity shift, Δy_B, and the rapidity of other particles were studied. It was found that in the region of $|\Delta y_B|<4$ the mean rapidity of other particles was nearly constant, while in the region of $|\Delta y_B|>4$ it slowly decreased. The correlations between the leading rapidity shift and the multiplicity were also investigated. In the region of $|\Delta y_B|<3$ the mean multiplicity increased with incresing $|\Delta y_B|$, while in the region of $|\Delta y_B|>4$ the mean multiplicity showed a sudden decrease.

These experimental results lead us to the following picture for multiparticle production in hadron-nucleus collisions:

- The mechanism of gray particle production consists of two processes. One of them is a slow moving source and in this process gray particles are produced isotropically like a nuclear evapolation. The other is a fast moving source and in this process most of gray particles are predominantly produced forward like a knocked-out proton and they are energetic.

- The intranuclear cascade is important in the rapidity region of $y<1$.

- Most of the lost rapidity of an incident proton is spent by particle production. The lost rapidity produces not a few fast particles but many particles with nearly constant rapidity.

The nuclear stopping power was estimated. A baryon traversing the central region of heavy nucleus (for example, Au) loses 80 % of its incident energy on the average.

MCMHA explained global features of hadron-nucleus collisions very well. This fact suggests that the multichain model and the existence of intranuclear cascade are appropriate for hadron-nucleus collisions. The improvement of MCMHA is required in order to understand the multiparticle production in hadron-nucleus collisions in more detail in the future.

Table captions

Table 2-1 RCBC basic parameters and operating conditions.

Table 2-2 Summary of drift chamber operating conditions.

Table 3-1 NA23B scanning convention.
(Event class and vertex/track type)

Table 3-2 Summary of measurement accuracy.

Table 3-3 Summary of events measured, on GST and in the foil region.

Table 3-4 Summary of reconstruction and hybridisation efficiencies.

Table 4-1 Summary of inelastic channels in cascade process of MCMHA. The probability of each channel was calculated under the assumption that the double charge exchange channels were forbidden.

Table 4-2 Summary of Δ decay modes. The probability of decay modes used in MCMHA are shown.

Table 5-1 Summary of background estimation. These three rolls were scanned in Tokyo.

Table 5-2 Summary of cross section estimation. In this analysis the target region is $-0.75 \leq z \leq -0.10$ for the z-direction.

Table 5-3 Summary of experimental multiplicity distributions and predictions from MCMHA.

Table 5-4 Summary of gray particle identifications. Values in parenthesis present ratios of proton/deuteron/heavier particle to gray particles. See text about the condition of particle identifications.

Table 5-5 Summary of Moving-source model fittng. Variables E_o, E_o^s and E_o^f are defined in text.

Figure captions

Fig.2-1 The European Hybrid Spectrometer (EHS) set-up for NA23 Part B. The position of each detector is represent as the distance from the centre of the Rapid Cycling Bubble Chamber (RCBC) in units of meter.

Fig.2-2 H2 beam line.

Fig.2-3 Schematic picture of Rapid Cycling Bubble Chamber (RCBC). Center region is the active volume.

Fig.2-4 Schematic view of foil targets and foil clamping system. Foil targets have the inclination of $18^{o}30$ against beam line.

Fig.2-5 Typical foil interaction picture.

Fig.2-6 Acceptance of EHS downstream lever arms as a function of longitudinal momentum, P_L. The acceptances of D1, D3 and D6 are presented.

Fig.2-7 Relative accuracy in function of momentum. (a)Non-hybridised tracks and (b)hybridised tracks.

Fig.2-8 Sketch of trigger configuration. See text for the detailed description of the interaction trigger logic.

Fig.3-1 Total and gray multiplicities in scanning as a function of z-coordinate from prediction. Open circles show mean total multiplicities and the histogram mean gray multiplicities. The region between two dotted lines is recognised as foil target. The horizontal dot-dashed line corresponds to mean total multiplicity (9.06) of 360 GeV/c p-p interactions.

Fig.3-2. Residual distributions of fiducial mark measurements. (a), (b) and (c) for X-component in view 1, 2 and 3, and (d), (e) and (f) for Y-component in view 1, 2 and 3.

Fig.3-3 EHS off-line software chain map.

Fig.3-4 Schematic view of EHS wire chamber co-ordinate system.

Fig.3-5 The scatter plot of X and Y coordinates of the reconstructed primary verteces. Open circles present the interaction points with $n_g>1$ and dots are the events with $n_g=0,1$.

Fig.3-6 The scatter plot of X' and Z coordinates of the reconstructed primary verteces. The horizontal axis expresses the corrected X (X': see test in detail). The symbols are the same as ones of fig.3-5. The target region is surrounded with solid lines.

Fig.3-7 Laboratory dependence of scanning for total and gray multiplicities. BO:Bombay, SE:Serpokhov, TO:Tokyo and VI:Vienna. x:p-Al and o:p-Au collisions. Dot-dashed lines show means of them.

Fig.4-1 Schematic picture of proton-nucleus collisions on the basis of the multichain model.

Fig.4-2 Basic structure of event generator MCMHA.

Fig.4-3 Sketch of cascade process in MCMHA. l_f is a formation length and l and L are the length of an unit cell and potential length. See the text about their definitions.

Fig.4-4 Flow chart of cascade process in MCMHA. This process is applied for all fragmented hadrons and recoil nucleon.

Fig.4-5 Total and elastic cross sections used in the cascade process of MCMHA as a function of incident momentum. (a)π^+p (π^-n), (b)π^-p (π^+n), (c)p-p (n-n) and (d)p-n (n-p).

Fig.4-6 Schematic picture of cascade interactions in MCMHA, which are elastic and inelastic scattering. Only delta production channel is treated as the inelastic channel in MCMHA.

Fig.4-7 Slope parameter used in the cascade process of MCMHA as a function of incident momentum. These values are used in both elastic and inelastic channels. (a)π^+p (π^-n), (b)π^-p (π^+n), (c)p-p (n-n) and (d)p-n (n-p).

Fig.4-8 Rapidity density distribution for 360 GeV/c p-p collisions. Histogram is the prediction of MCMHA.

Fig.4-9 Rapidity density distributions of shower particles for (a) 200 GeV/c p-Ar and (b)p-Xe collisions [20]. Histograms show the predictions of MCMHA.

Fig.4-10 Ratios of rapidity density to p-p for (a)p-Ar and (b)p-Xe interaction [20]. Histograms represent the predictions of MCMHA including the cascade process and solid curves are those of MCMHA excluding the cascade process.

Fig.4-11 Multiplicity distribution of shower particles for 100 GeV/c p-Au collisions [21]. Solid, dotted and dot-dashed lines are the predictions of MCMHA with and without the cascade process and the KNO scaling distribution, respectively.

Fig.5-1 Beam profile in YZ-plane at RCBC position. A solid rectangle presents the foil region.

Fig.5-2 Cross sections of proton-nucleus interactions. Crosses present the cross section obtained by Carrol et al.[2], diamonds by Azimov et al.[3], circles by De Marzo et al.[4] and squares by this experiment. The dotted line corresponds to α=0.718 in $\sigma_A \propto A^{\alpha}$ [2].

Fig.5-3 Total charged multiplicity distribution for (a)p-Al and (b)p-Au. Dot-dashed lines correspond to KNO scaling curves and dotted lines express the results of MCMHA.

Fig.5-4 Normalised gray multiplicity distributions for (a)p-Al and (b)p-Au collisions. Dashed lines represent the predictions of Hegab and Hufner model [8]. Histograms correspond to results of MCMHA.

Fig.5-5 Multiplicity distributions of all shower, positive shower and negative shower particles. (a) and (b) correspond to all shower particles of p-Al and p-Au, (c) and (d) to positive shower particles of p-Al and p-Au, and (e) and (f) to negative shower particles of p-Al and p-Au, respectively. Dot-dashed lines are KNO scaling curves and dotted lines show the predictions of MCMHA. Solid lines in (a) and (b) present the predictions by the model of Kiang et al.[9].

Fig.5-6 Dispersion D_- of negative particles as a function of the mean multiplicity $\langle n_- \rangle$. The straight line shows the Wroblewski relation [10].

Fig.5-7 Relation between R_A and $\bar{\nu}_A$. The straight line corresponds to $R_A=0.5(\bar{\nu}_A+1)$.

Fig.5-8 (a)The scatter plot of momentum and range of gray particles with $\Delta p/p < 20$ %. Broken lines show the range-momentum relation for proton (left) and deuteron (right).

(b)The distribution of a projection of points along the broken line in (a). This histogram is fitted with the superposition of two Gaussian distributions (dashed lines).

Fig.5-9 (a) Angular distribution of gray particles for p-Al (cross) and p-Au (square) collisions.

(b) Angular distribution of identified deuterons for p-Au collisions.

Fig.5-10 Momentum distributions of gray particles for (a)p-Al and (b)p-Au collisions. Histograms show the predictions of MCMHA.

Fig.5-11 Energy spectrum of gray particles for (a)p-Al and (b)p-Au collisions. Dot-dashed lines show the fitted lines to the single-moving-source model, Solid lines correspond to the two-moving-source model and dashed line to its fast component.

Fig.5-12 Distributions of mean X as a function of the leading number for (a)p-Al and (b)p-Au collisions. Histogram shows the mean of X of all events. The mean X of events which the fastest particle is positive is shown with squares and the other is done with cross.

Fig.5-13 The distribution of leading rapidity shift for (a)p-Al and (b)p-Au collisions. Histograms represent the predictions of MCMHA and histogram with dashed lines the component of projectile proton in them.

Fig.5-14 Distributions of rapidity density, $\rho(y)$, of all shower particles (a)(b), positive shower (c)(d) and negative shower particles (e)(f). Histograms express the predictions from MCMHA.

Fig.5-15 Distributions of rapidity density ratio, R(y), for (a)p-Al and (b)p-Au collisions. Solid lines correspond to the predictions of Lund Monte Carlo FRITIOF [15] and histograms to those of MCMHA.

Fig.5-16 Invariant cross section of (a)leading and (b)positive shower particle as a function of x. Diamonds are ones for p-Al and crosses for p-Au collisions. In (a) the inclusive cross sections of p+Al->p+X (squares) and of p+Pb->p+X (circles) [16] are also shown. In (b) the inclusive cross sections of p+Al->π^++X (squares) and of p+Pb->π^++X (circles) are shown.

Fig.5-17 Correlations between the leading rapidity shift and the mean rapidity of other shower particles for (a)p-Al and (b)p-Au collisions. Histograms are the predictions of MCMHA.

Fig.5-18 Correlations between the leading rapidity shift and the mean rapidity of other particles for (a)p-Al and (b)p-Au collisions. Histograms show the predictions of MCMHA.

Fig.5-19 Correlations between the leading rapidity shift and the mean multiplicity of shower particles for (a)p-Al and (b)p-Au collisions. Histograms present the predictions of MCMHA.

Fig.5-20 Correlations between the leading rapidity shift and the mean multiplicity of charged particles for (a)p-Al and (b)p-Au collisions. Histograms are the predictions of MCMHA.

Fig.5-21 Averaged X of the fastest particle as a function of the mean number of collisions for p-Au collisions. The mean number of collisions is estimated by the relation with the number of gray particles. (see text) Crosses are those for all events and squares are for the events whose fastest particle is positive.

Table 2-1 RCBC Characteristics

Diameter	80 cm
Depth	40 cm
Static pressure	5.0 bar
Vapour pressure at 25K	3.2 bar
Expanded pressure	1.1 bar
Flash delay	1.0÷1.5 ms
Width of expansion pulse	11 ms
Precision with respect to chamber fiducial mark	
- in the bending plane	50 μm
- in the dip plane	150 μm
Optical resolution	< 300 μm
Exit angle for chamber body	
- in the bending plane	$\pm 30^{\circ}$
- in the dip plane	$\pm 13.5^{\circ}$
Material in the beam exit	
- radiation length	14.6 %
- collision length	2.55%

Table 2-2 Drift Chamber Operating Condition Summary

	D1, D2, D3	D4, D5, D6
Supplied voltage at sense wire	- 3.0 kV	- 2.7 kV
Supplied voltage at field wire	1.4 kV	1.6 kV
Meam Drift velocity	47 μm/ns	53 μm/ns
Maximum drift time	≅500 ns	
Precision	≅200 μm	

Table 3-1 NA23 Scanning Convention

Event Class	Descriptions
0	Default ("normal" event with Hydrogen)
1	Elastic event
10	Default, but being a possible secondary of a "wallon" in predicted y region
11	Elastic, but being a possible secondary of a "wallon" in predicted y region
20	Interaction on foil in all views
91	No prediction
92	Window interaction (wallon) in predicted y region, but no visible event
93	Interaction beyond line joining fiducials 104 and 105
94	No interaction on predicted beam
95	No beam corresponding to prediction
96	Bad visibility of event
97	More than one view missing or with no flash

Table 3-1 NA23 Scanning Convention (continue)

Vertex/Track Type	Description
1 (B)	Primary vertex
2 (V)	Neutral decay but not identified γ
4 (S)	Heavily ionizing possible stopping
5 (D)	Charged decay
6 (N)	Neutral interaction
7 (I)	Charged interaction
8 (G)	Clear γ
10 (E)	Clearly identified electron leaving primary vertex and event topology
12 (P)	Identified proton stop
14 (R)	π decay at rest, end point of π
15 (X)	Vertex with confused origin and multiplicity

Table 3-2 Summary of Measurement Accuracy

	View 1	View 2	View 3
Residuals of fiducial meas. (r.m.s.) X	5.4 μm	5.2 μm	5.4 μm
Y	6.1	5.6	5.0
Track residuals	70.6±25.1	75.4±27.4	77.2±29.2
Error of point reconstruction	X	Y	Z
SNK	168±69 μm	66±22 μm	460±167 μm
All meas. data	112±52	59±20	407±160

Table 3-3 Summary of Number Events

Lab.	Rolls	Measured	on GST	Foil	event/roll
TO (MO) (MA)	57,59,67 64,69 54,58	118	117	Al: 17 Au: 54	2.4±0.6 7.7±1.1
SE (MW)	50,53,55 56,62,65 66	251	240	Al: 18 Au: 82	2.6±0.6 11.7±1.6
BO (PA)	63 51,52	162	162	Al: 7 Au: 35	2.3±0.9 11.7±2.0
VI	60,61,68	62	61	Al: 5 Au: 21	1.7±0.6 7.0±1.5
Total	50 -> 69	593	580	Al: 47 Au: 192	2.4±0.3 9.6±0.7

Table 3-4 Reconstruction and Hybridisation Efficiency

Laboratory	Reconstruction	Hybridisation
Tokyo	0.99 ± 0.01	0.89 ± 0.03
Serpukhov	0.97 ± 0.00	0.86 ± 0.02
Vienna	0.96 ± 0.02	0.91 ± 0.05
Bombay	0.97 ± 0.01	0.89 ± 0.03
Total	0.97 ± 0.004	0.88 ± 0.02

Table 4-1 Inelastic channels

Inelastic Channel		Probability
π^{+} p --->	π^{+} Δ^{+}	0.40
	π^{o} Δ^{++}	0.60
π^{-} p --->	π^{-} Δ^{+}	0.67
	π^{o} Δ^{o}	0.33
π^{+} n --->	π^{+} Δ^{o}	0.67
	π^{o} Δ^{+}	0.33
π^{-} n --->	π^{-} Δ^{o}	0.40
	π^{o} Δ^{-}	0.60
π^{o} p --->	π^{o} Δ^{+}	0.11
	π^{-} Δ^{++}	0.47
	π^{+} Δ^{o}	0.42
π^{o} n --->	π^{o} Δ^{o}	0.11
	π^{+} Δ^{-}	0.47
	π^{-} Δ^{+}	0.42
p p --->	p Δ^{+}	0.25
	n Δ^{++}	0.75
p n --->	p Δ^{o}	0.50
	n Δ^{+}	0.50
n n --->	n Δ^{o}	0.25
	p Δ^{-}	0.75

Table 4-2 Δ Decay Mode

Decay mode	Probability
$\Delta^+ \rightarrow \pi^o p$	2/3
$\pi^+ n$	1/3
$\Delta^o \rightarrow \pi^o n$	2/3
$\pi^- p$	1/3
$\Delta^{++} \rightarrow \pi^+ p$	
$\Delta^- \rightarrow \pi^- n$	

Table 5-1 Background Estimation Summary

Roll	Number of pp events in foil region: Al	Au
57	163	416
59	143	326
67	201	564
Total	507	1306

Roll	Numner of foil events: Al (corrected)	Au (corrected)
57	5 (4.92)	7 (5.92)
59	3 (2.93)	9 (8.16)
67	3 (2.90)	11 (9.54)
Total	11 (10.8)	27 (23.6)

Table 5-2 Cross Section Estimation Summary

Roll	Number of pp events in foil region ($-0.75 \leq z \leq -0.10$) Al: All	Al: ≥ 4	Au: All	Au: ≥ 4
57	79	77	164	158
59	58	53	131	122
67	79	74	258	249
Total	216	204	553	529

Roll	Numner of foil events ($-0.75 \leq z \leq -0.10$) Al (corrected)		Au (corrected)	
57	5	(4.95)	5	(4.57)
59	3	(2.96)	7	(6.66)
67	3	(2.95)	9	(8.33)
Total	11	(10.9)	21	(19.6)
Cross Section	400 ± 120 mb		1500 ± 300 mb	

Table 5-3 Summary of Multiplicity Distributions

			Experimental results	MCMHA
Total charged	Al	<n>	17.7 ± 1.5	15.9
		D	10.6 ± 1.3	10.6
	Au	<n>	28.2 ± 1.3	26.7
		D	18.5 ± 1.1	17.8
Gray	Al	<n>	1.9 ± 0.5	2.0
		D	3.2 ± 0.9	2.4
	Au	<n>	4.6 ± 0.4	5.1
		D	5.1 ± 0.5	5.6
Shower	Al	<n>	15.7 ± 1.3	13.9
		D	9.1 ± 0.8	8.8
	Au	<n>	23.6 ± 1.1	21.7
		D	15.1 ± 1.0	13.4
Positive Shower	Al	<n>	9.3 ± 0.7	7.1
		D	5.1 ± 0.5	4.6
	Au	<n>	14.2 ± 0.7	10.8
		D	9.0 ± 0.4	7.0
Negative Shower	Al	<n>	6.8 ± 0.6	6.3
		D	4.4 ± 0.4	4.3
	Au	<n>	8.9 ± 0.4	10.4
		D	5.4 ± 0.3	7.0

Table 5-4 Gray Particle Identification Summary

Identified track	p-Al	p-Au
Proton		
Type I	0.40 ± 0.11/ev.	0.90 ± 0.11/ev.
Type II	0.74 ± 0.23	1.36 ± 0.17
Type III	0.09 ± 0.05	0.35 ± 0.05
Total	1.23 ± 0.32 (0.84)	2.61 ± 0.27 (0.78)
Deuteron	0.17 ± 0.10 (0.12)	0.47 ± 0.07 (0.14)
Triton/Alpha	0.06 ± 0.05 (0.04)	0.26 ± 0.05 (0.08)
Total Gray (GST)	1.47 ± 0.41	3.34 ± 0.32

Table 5-5 Invariant Energy Spectrum

Single-moving-source fiting		
	p-Al	p-Au
E_o	84.9 ± 7.9 MeV	65.0 ± 3.2 MeV
χ^2/NDF	5.05/9	32.2/14

Two-moving-source fitting		
	p-Al	p-Au
E_o^s	51.1 ± 23.8 MeV	52.7 ± 7.6 MeV
E_o^f	175.9 ± 112.9 MeV	135.0 ± 40.3 MeV
χ^2/NDF	1.76/7	18.4/12

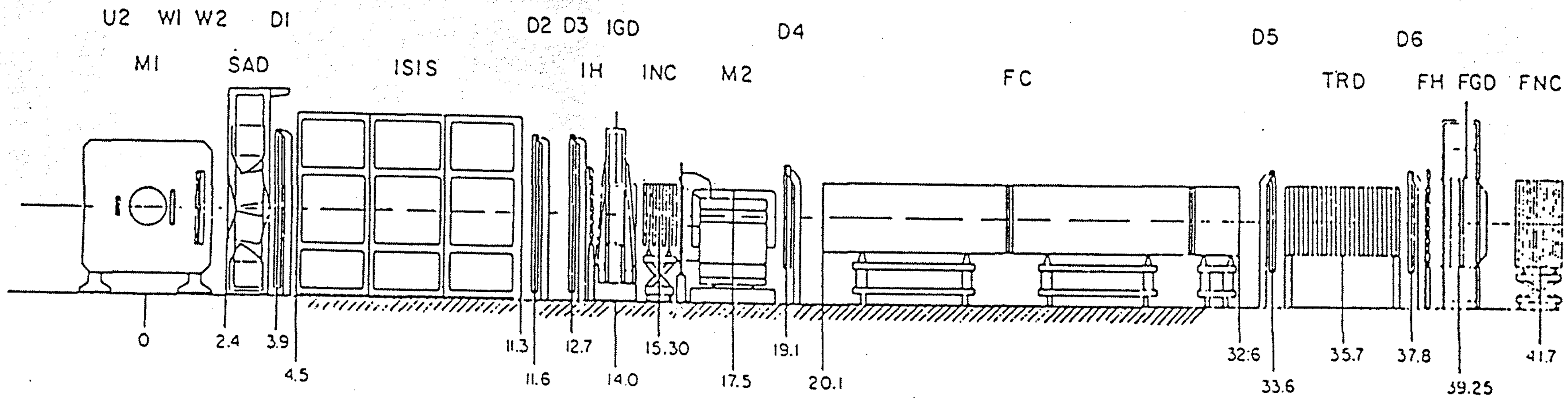
U2
W1
W2
D1
M1
SAD
ISIS
D2
D3
IGD
IH
INC
M2
D4
FC
D5
TRD
D6
FH
FGD
FNC
0
2.4
3.9
4.5
11.3
11.6
12.7
14.0
15.30
17.5
19.1
20.1
32.6
33.6
35.7
37.8
39.25
41.7

Fig.2–1

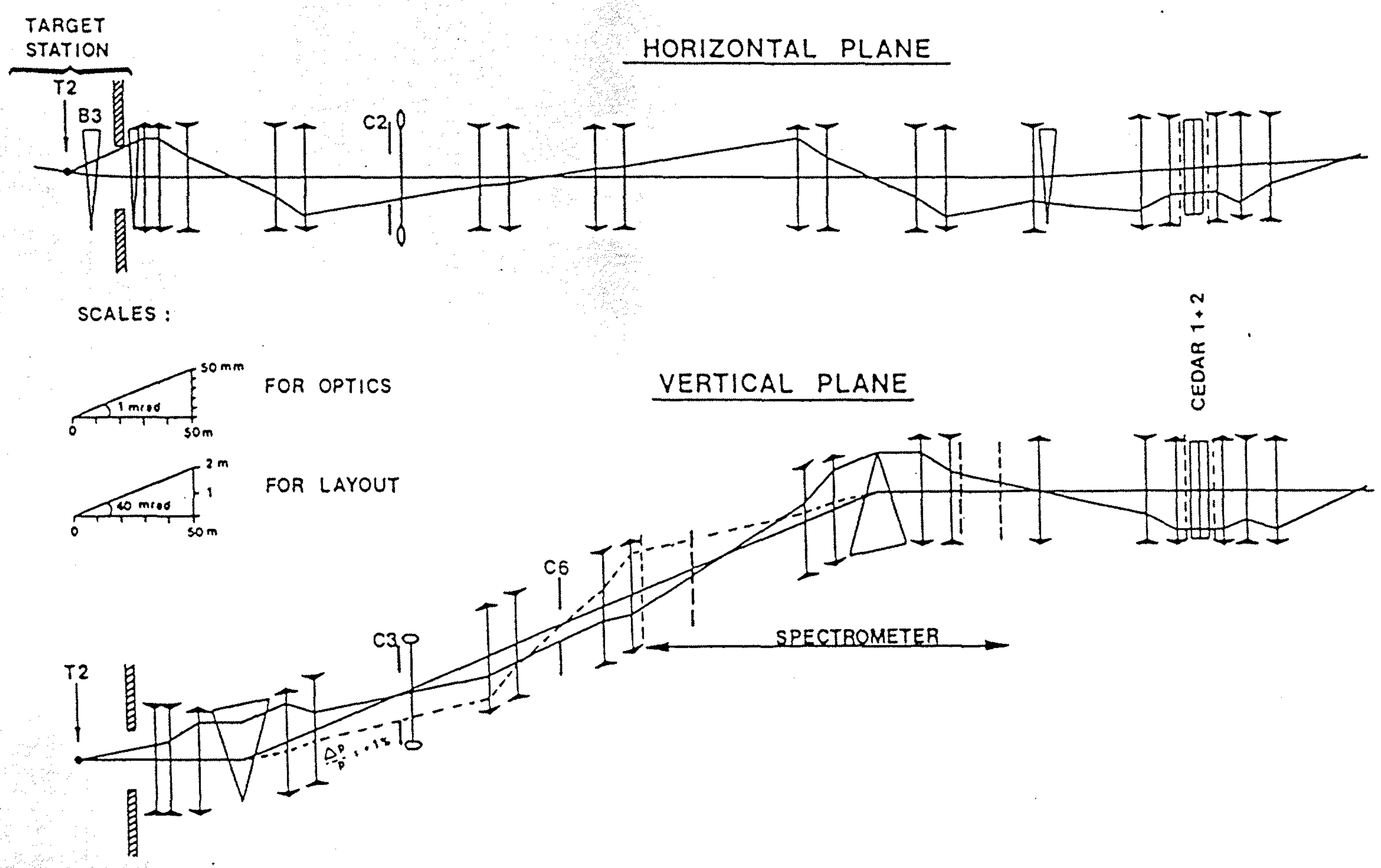
TARGET STATION
HORIZONTAL PLANE
T2
B3
C2
SCALES :
50 mm
1 mrad
0
50m
FOR OPTICS
2 m
1
40 mrad
0
50 m
FOR LAYOUT
VERTICAL PLANE
CEDAR 1+2
C6
C3
T2
SPECTROMETER

Fig.2-2

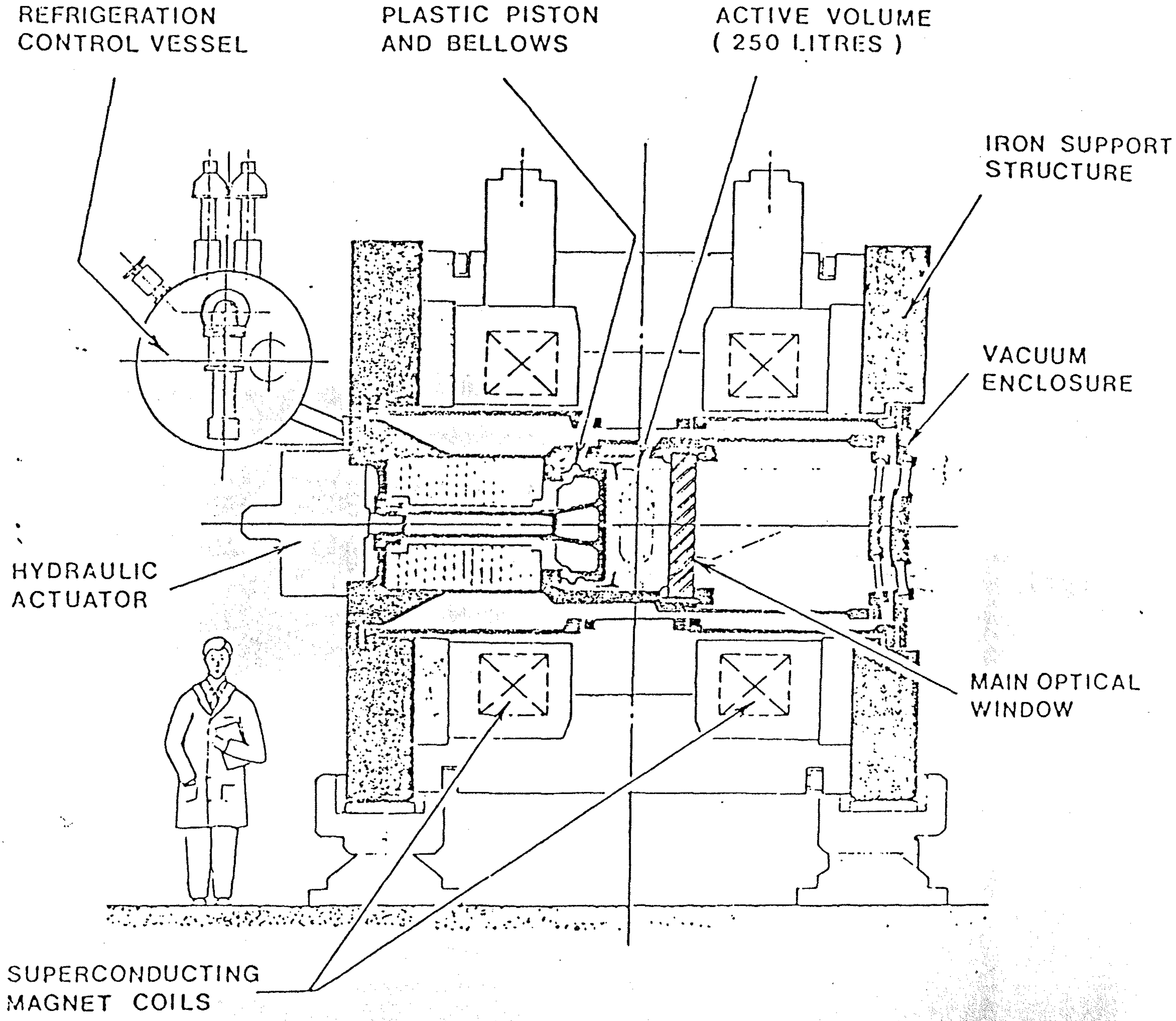
REFRIGERATION
CONTROL VESSEL
PLASTIC PISTON
AND BELLOWS
ACTIVE VOLUME
(250 LITRES)
IRON SUPPORT
STRUCTURE
VACUUM
ENCLOSURE
HYDRAULIC
ACTUATOR
MAIN OPTICAL
WINDOW
SUPERCONDUCTING
MAGNET COILS

Fig.2-3

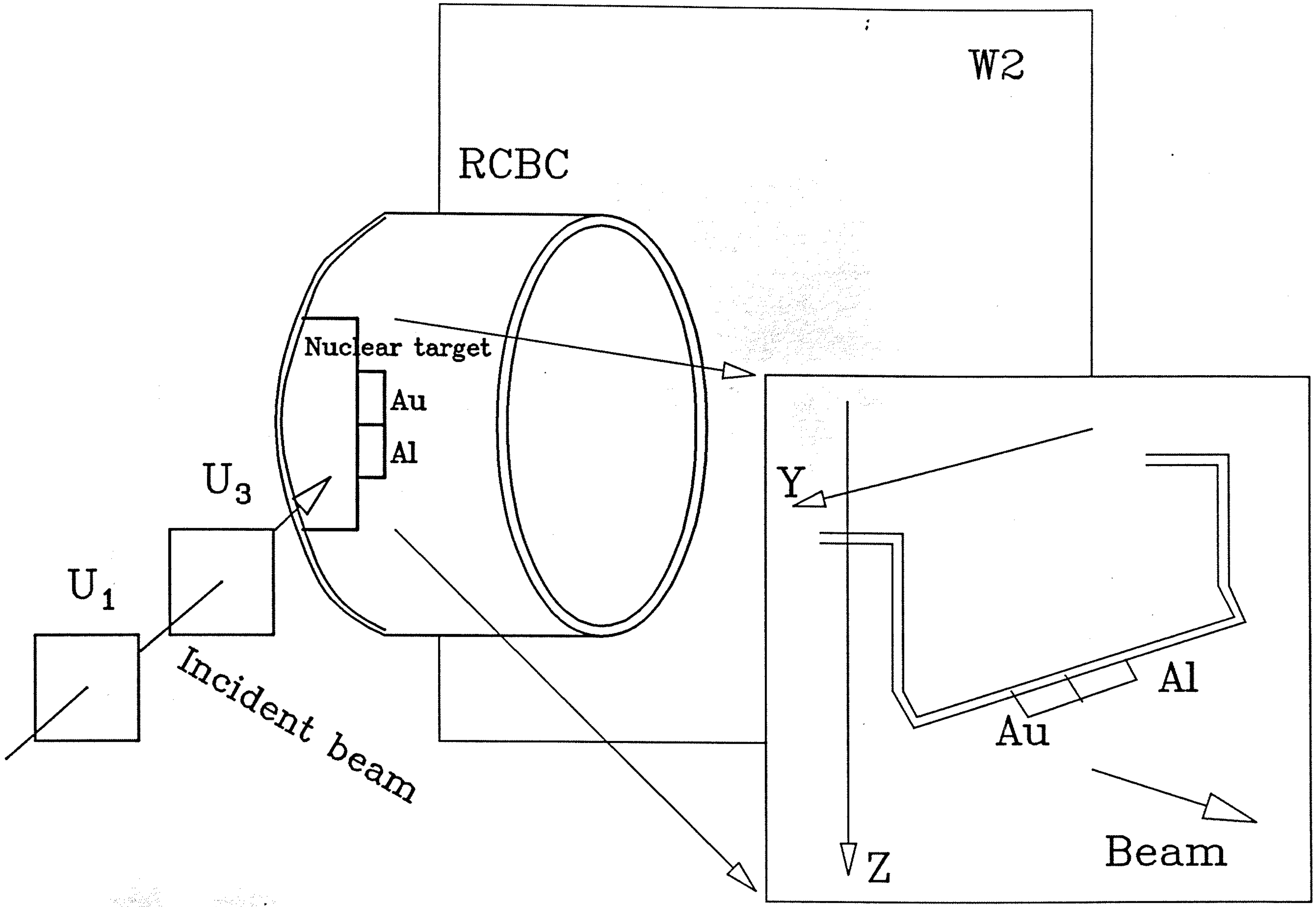

Fig.2–4

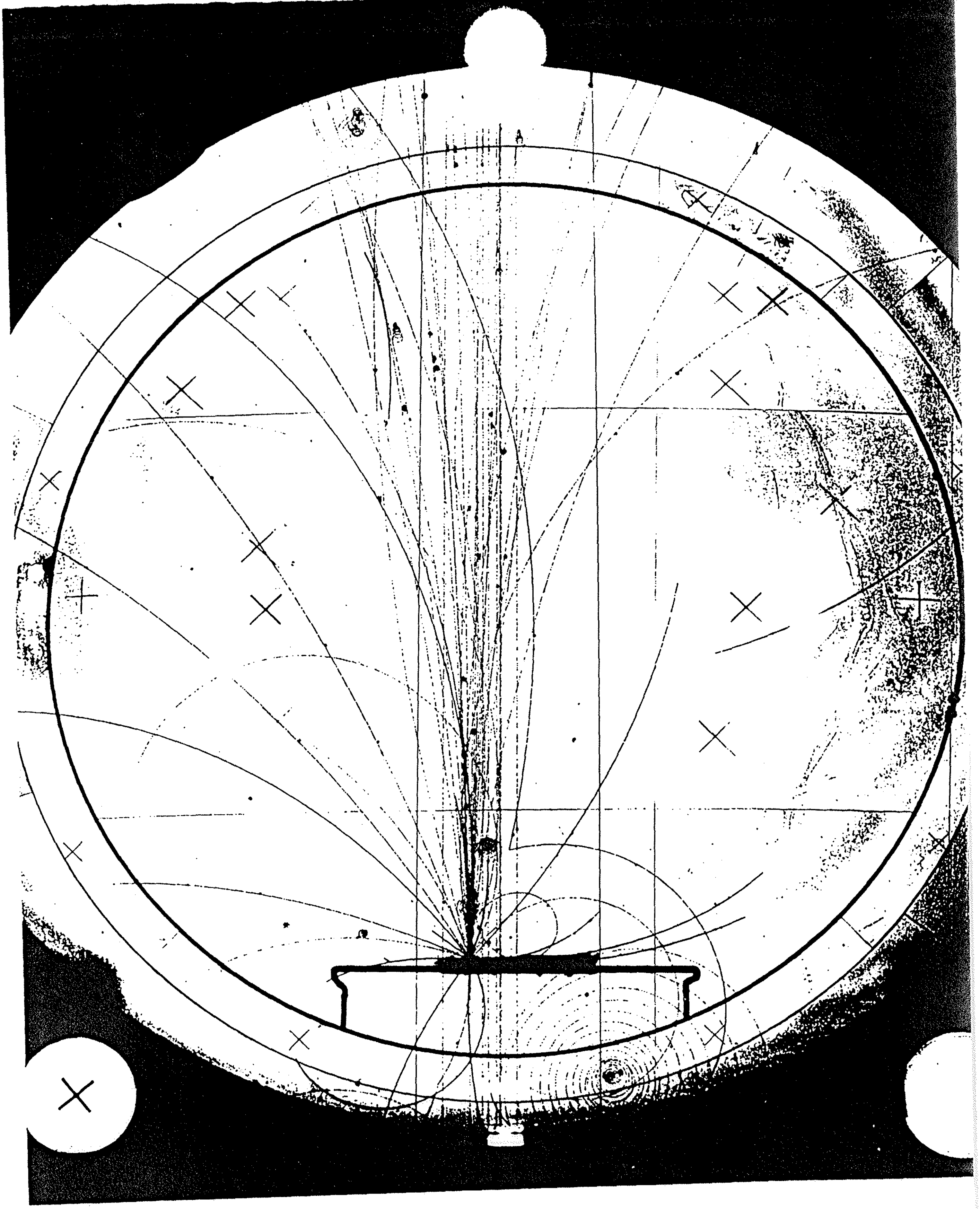

Fig.2−5

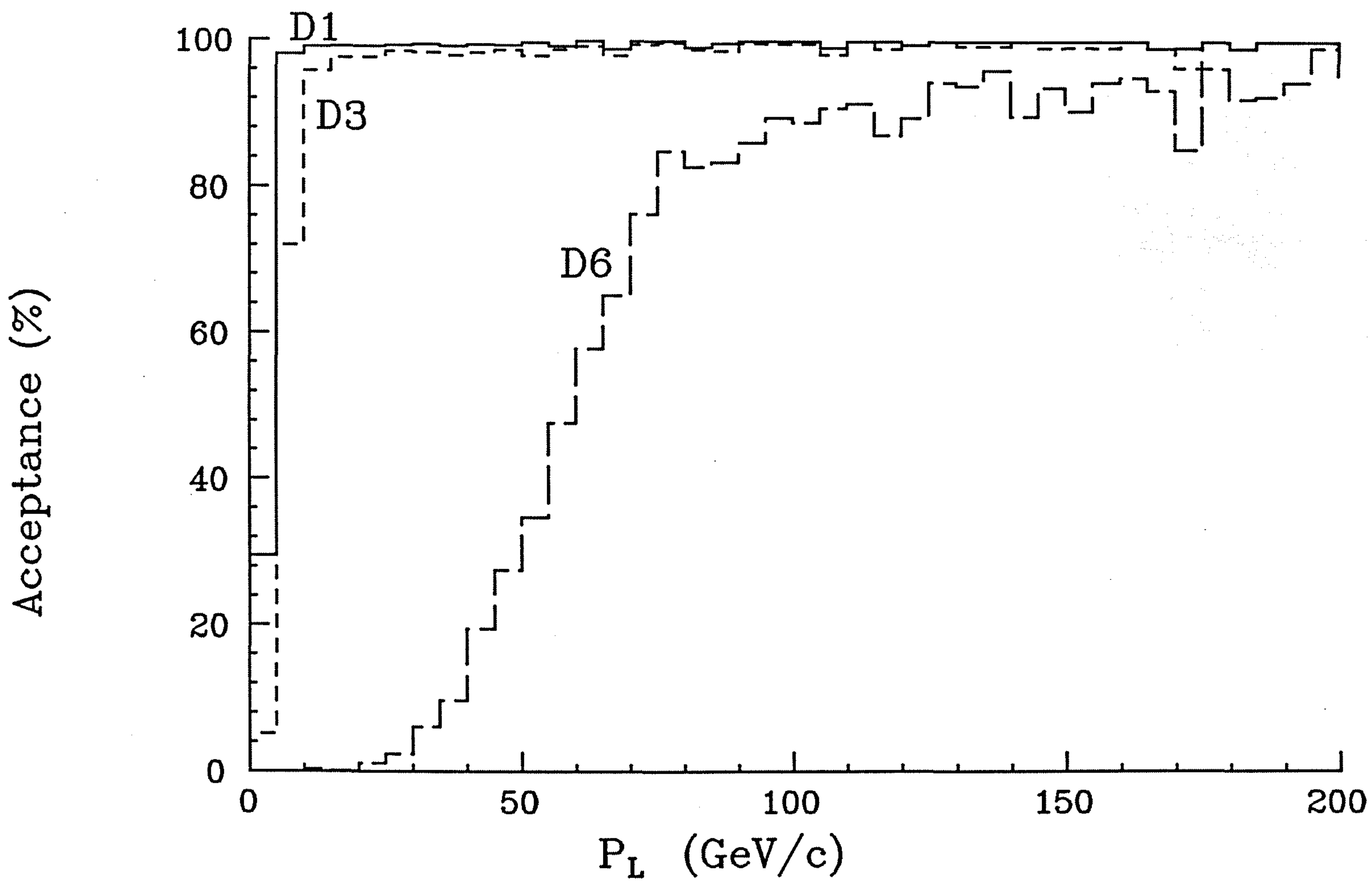

Fig.2–6

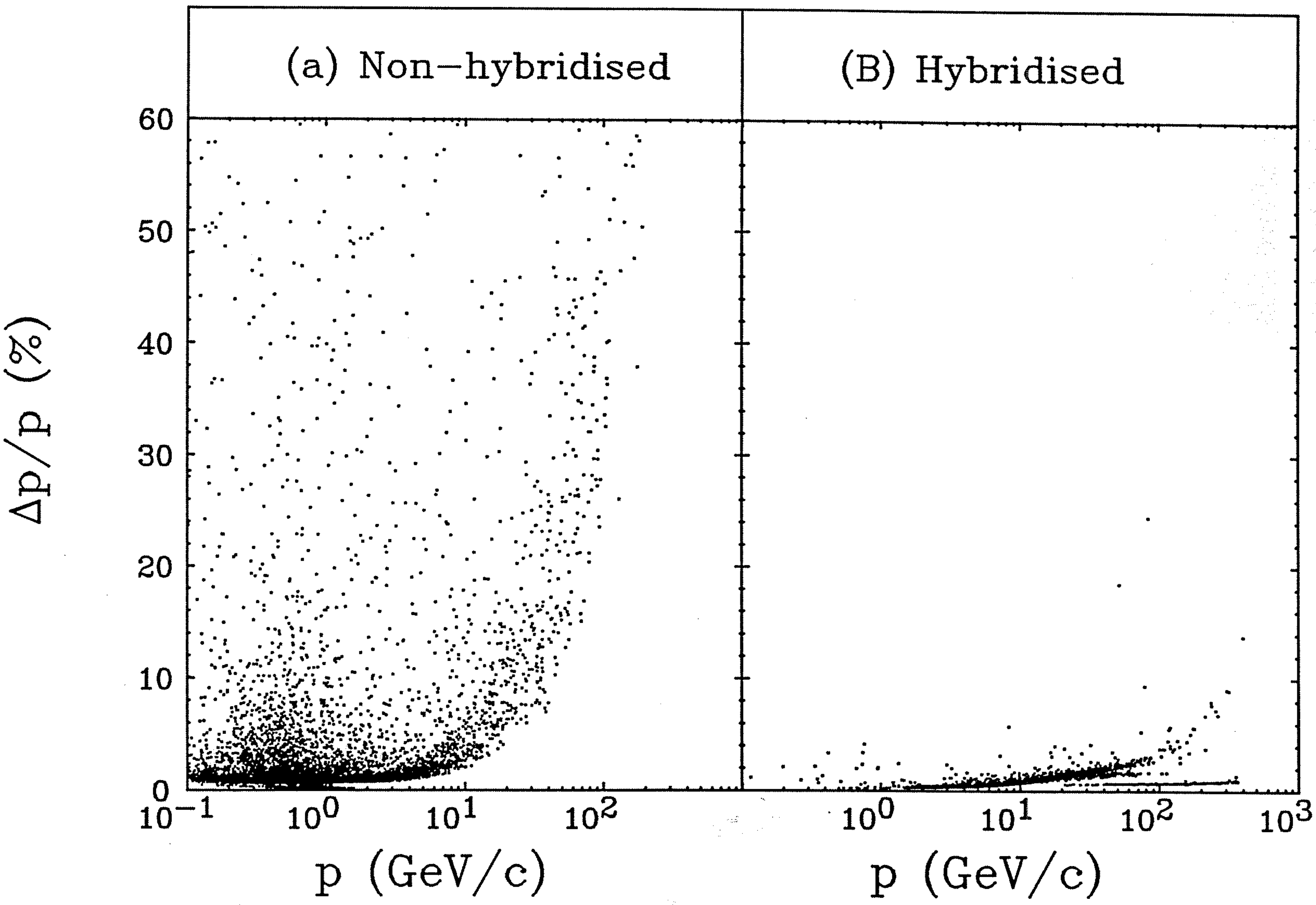
(a) Non-hybridised
(B) Hybridised
Δp/p (%)
60
50
40
30
20
10
0
10−1
10^0
10^1
10^2
10^3
p (GeV/c)
p (GeV/c)
Fig.2−7

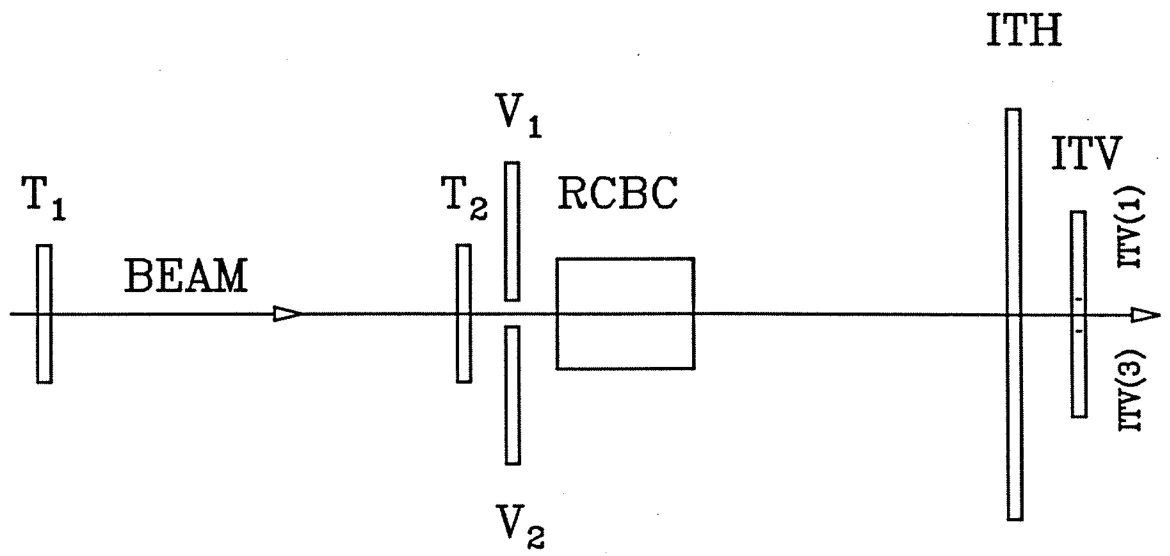

Fig.2–8

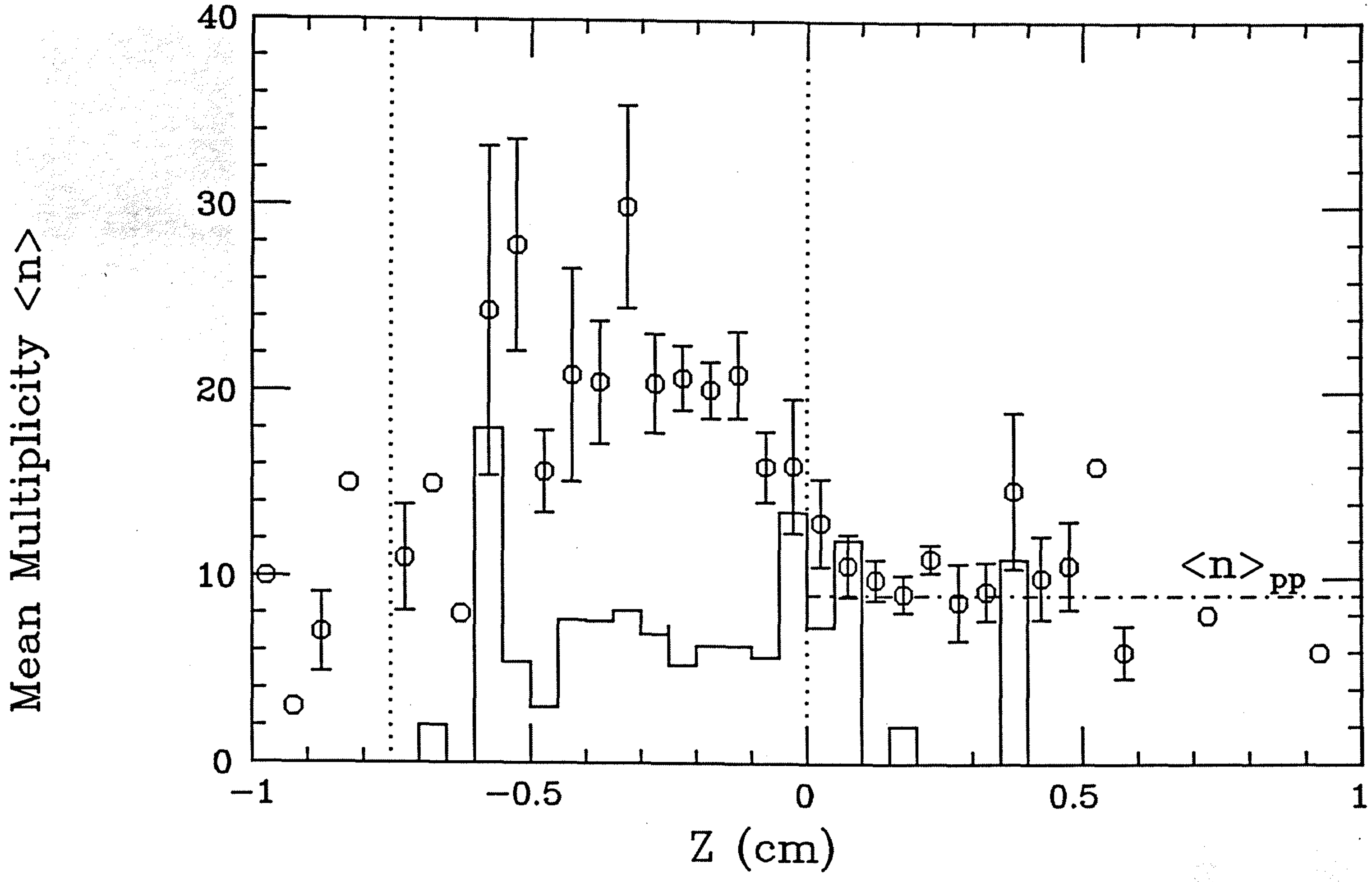

Fig.3−1

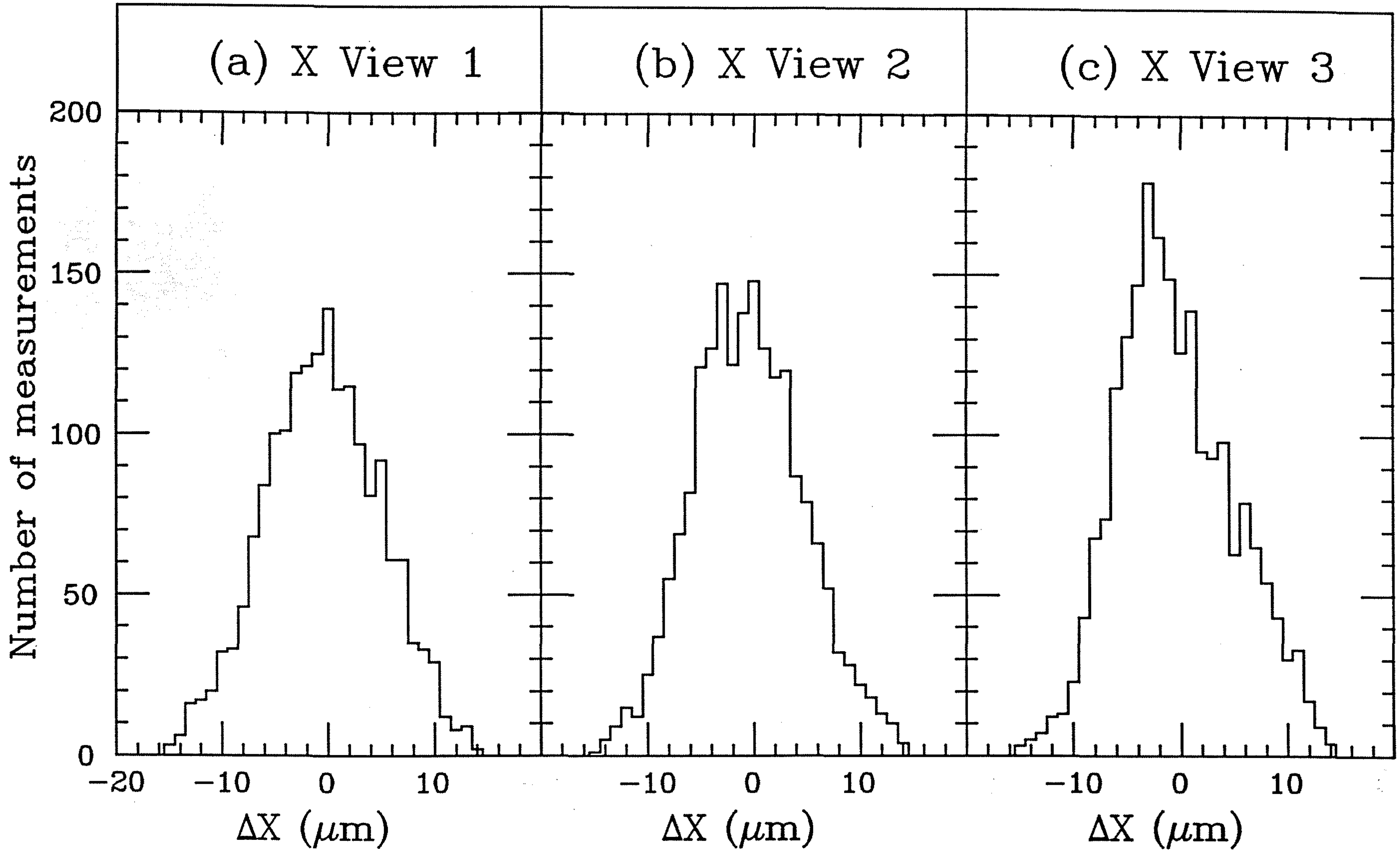
(a) X View 1
(b) X View 2
(c) X View 3
Number of measurements
200
150
100
50
0
−20
−10
0
10
ΔX (μm)

Fig.3−2

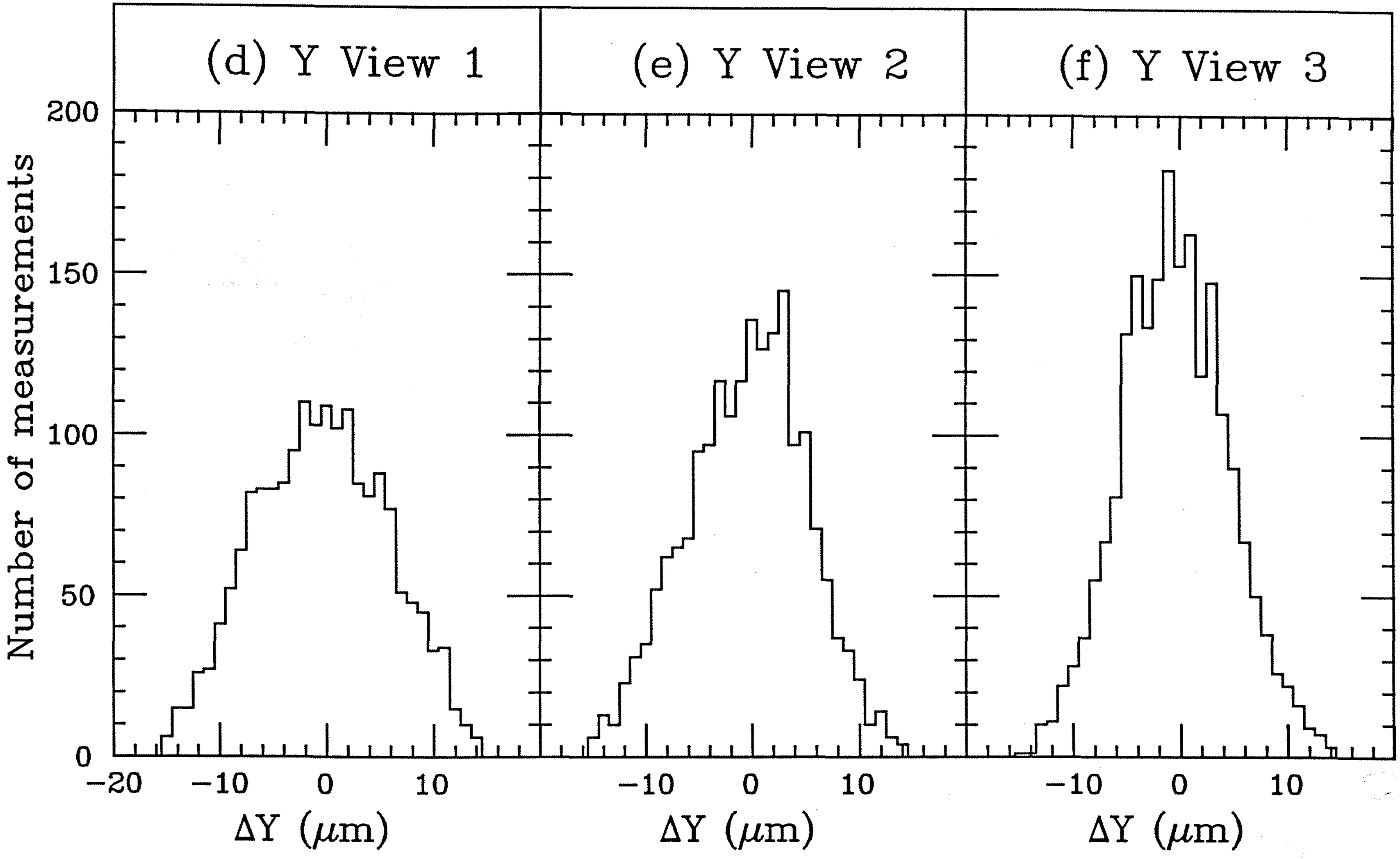
(d) Y View 1
(e) Y View 2
(f) Y View 3
Number of measurements
200
150
100
50
0
−20
−10
0
10
ΔY (μm)

Fig.3−2

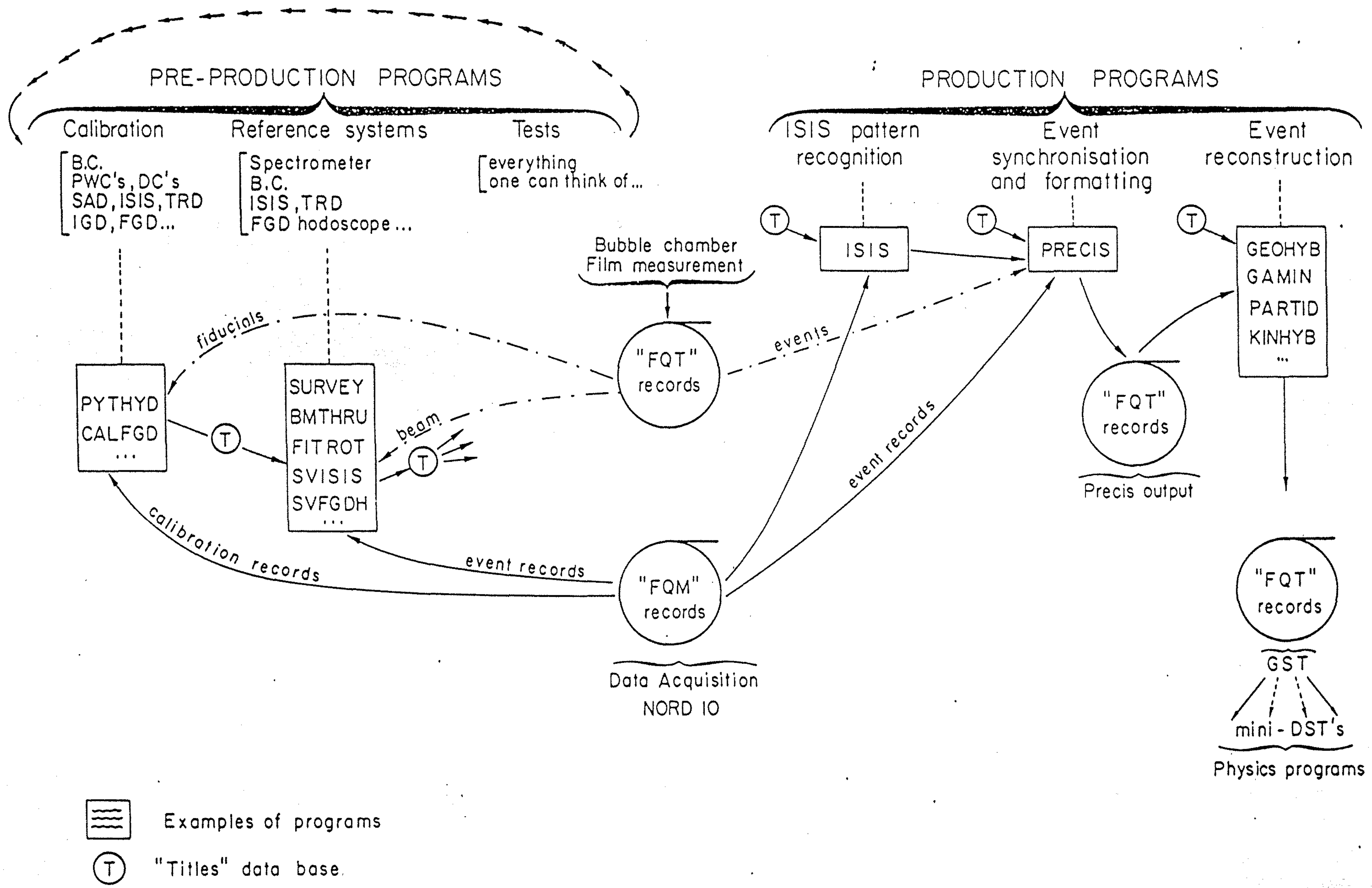
PRE-PRODUCTION PROGRAMS
Calibration
B.C.
PWC's, DC's
SAD, ISIS, TRD
IGD, FGD...
Reference systems
Spectrometer
B.C.
ISIS, TRD
FGD hodoscope ...
Tests
everything
one can think of...
PRODUCTION PROGRAMS
ISIS pattern recognition
Event synchronisation and formatting
Event reconstruction
ISIS
PRECIS
GEOHYB
GAMIN
PARTID
KINHYB
...
Bubble chamber
Film measurement
"FQT" records
fiducials
events
PYTHYD
CALFGD
...
SURVEY
BMTHRU
FITROT
SVISIS
SVFGDH
...
beam
"FQT" records
Precis output
event records
calibration records
event records
"FQM" records
Data Acquisition
NORD 10
"FQT" records
GST
mini-DST's
Physics programs
Examples of programs
"Titles" data base

Fig.3—3

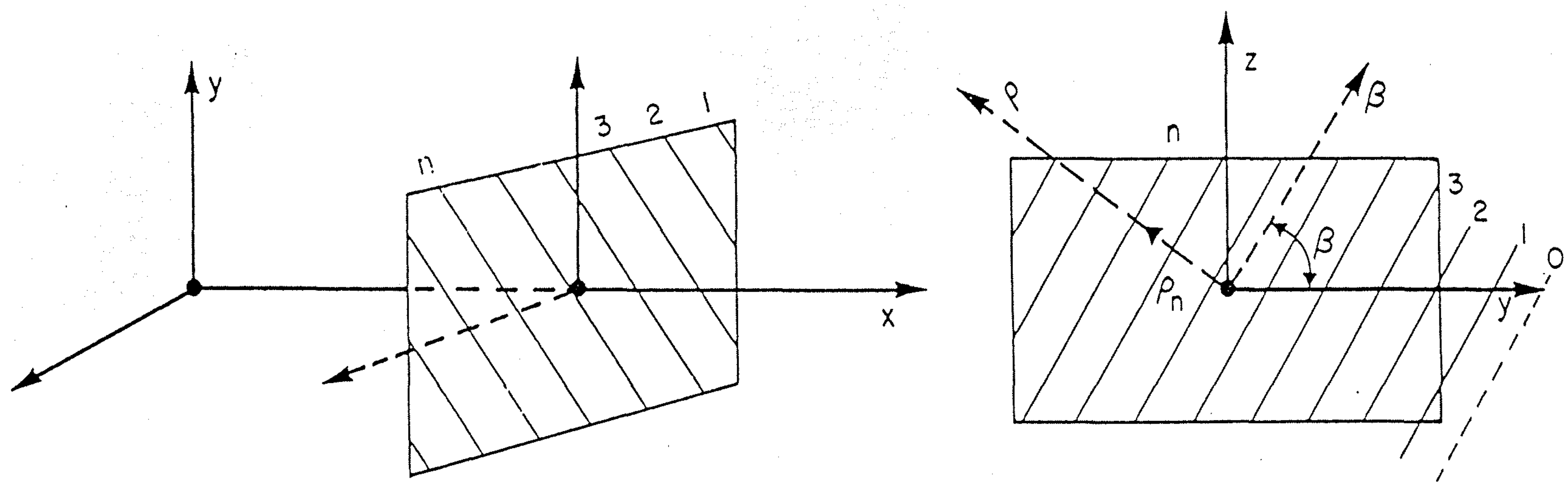

Fig.3—4

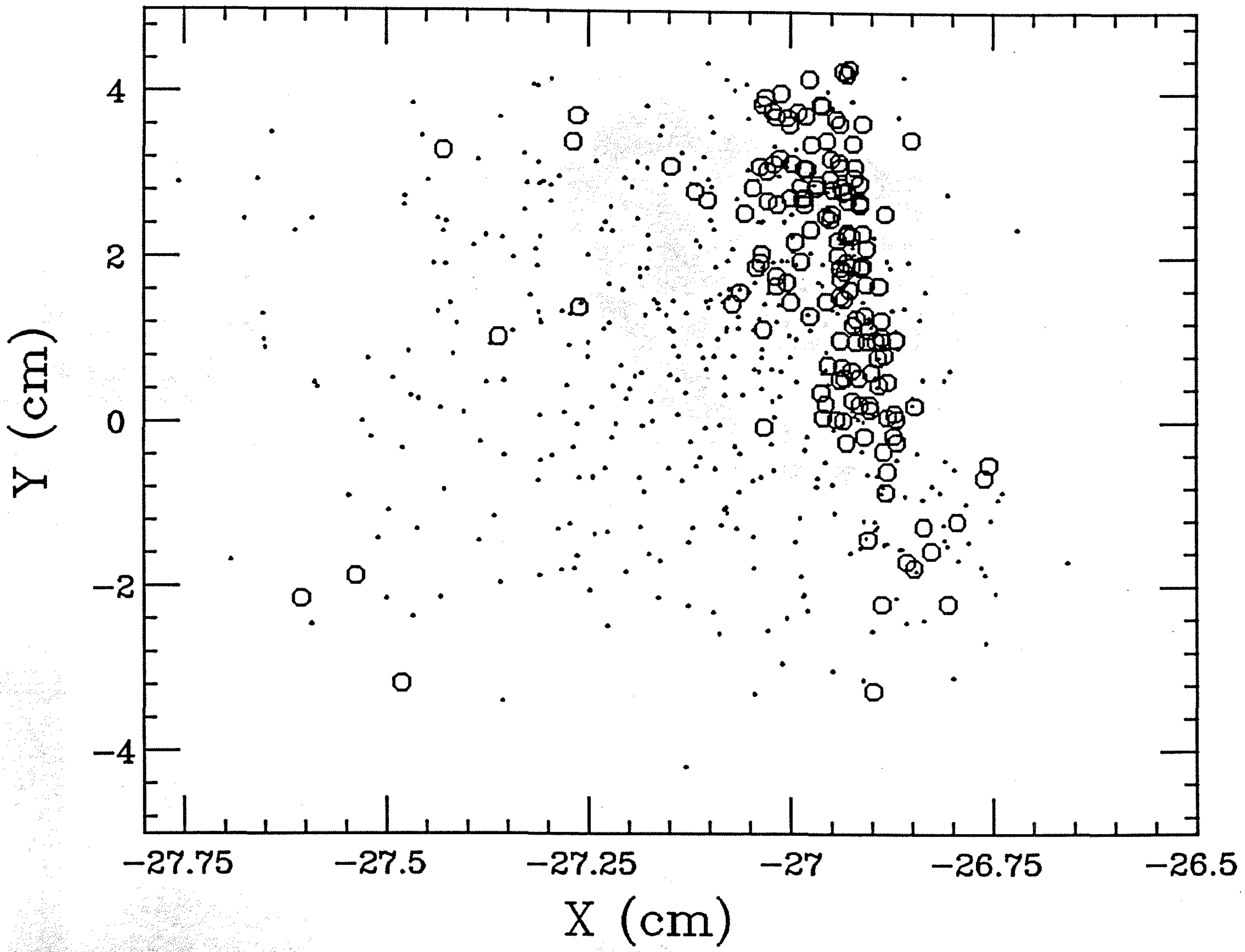

Fig.3−5

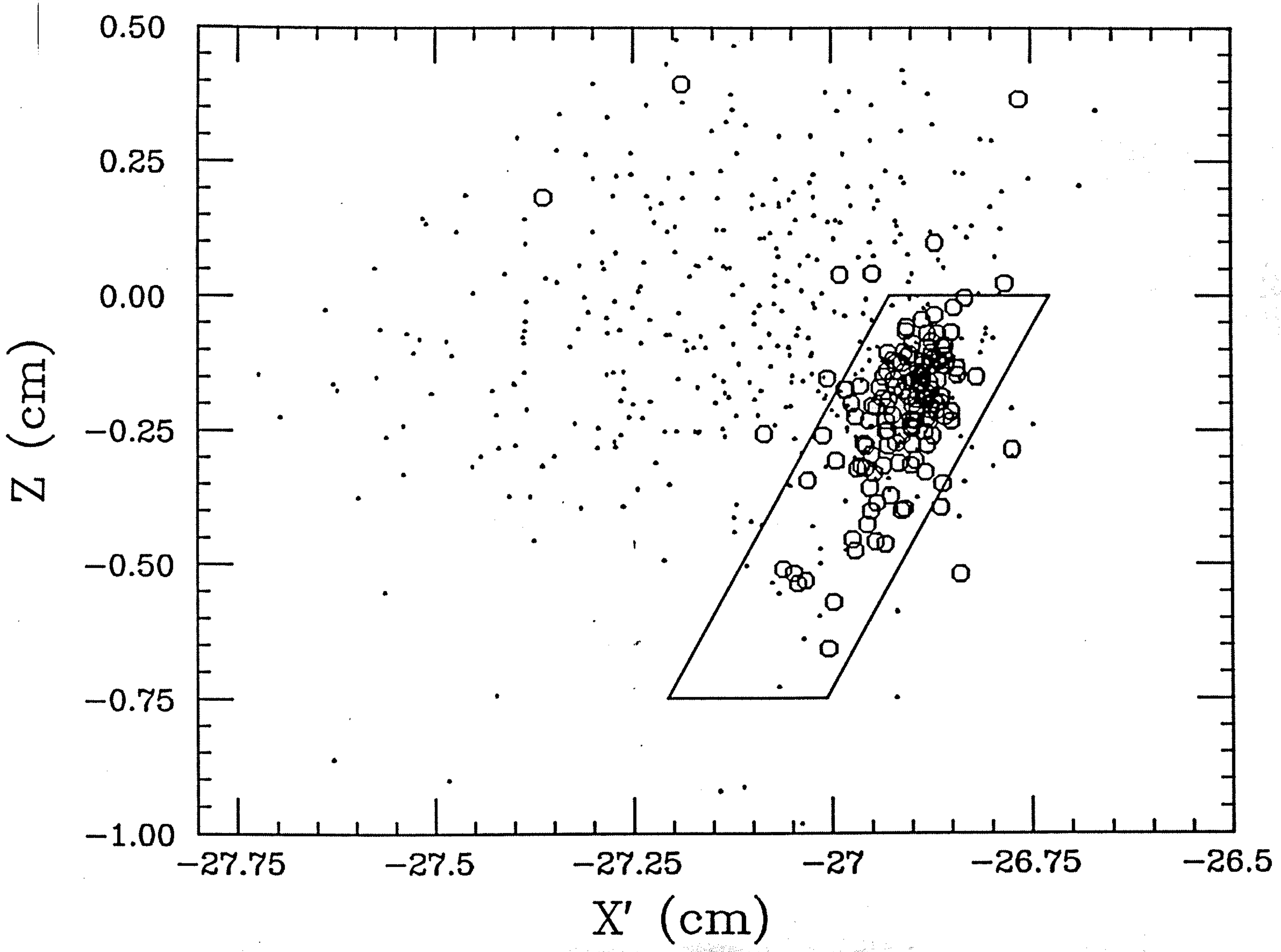

Fig.3−6

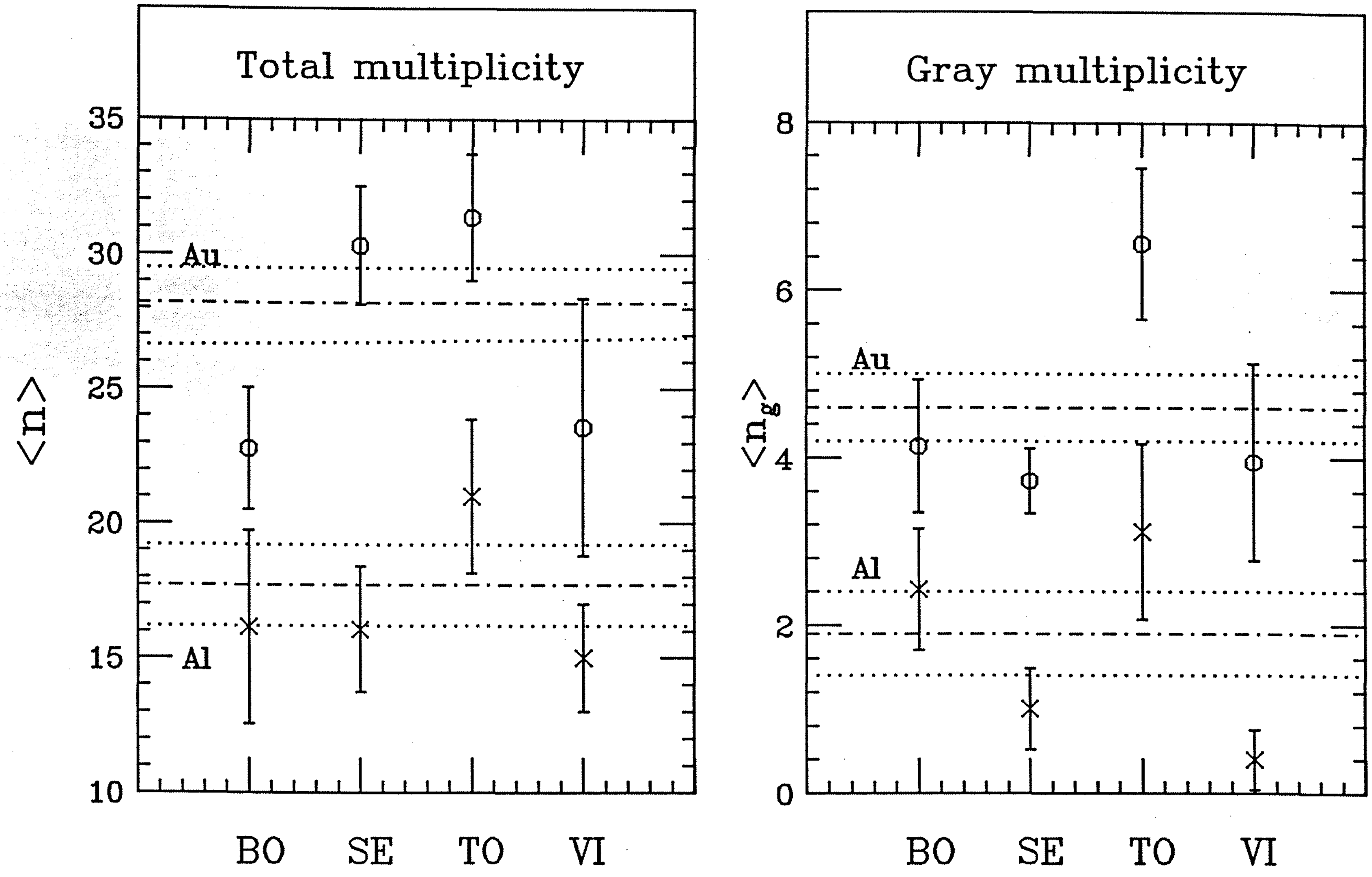
Total multiplicity
Gray multiplicity
<n>
$\langle n_g \rangle$
35
30
25
20
15
10
8
6
4
2
0
Au
Al
BO
SE
TO
VI

Fig.3—7

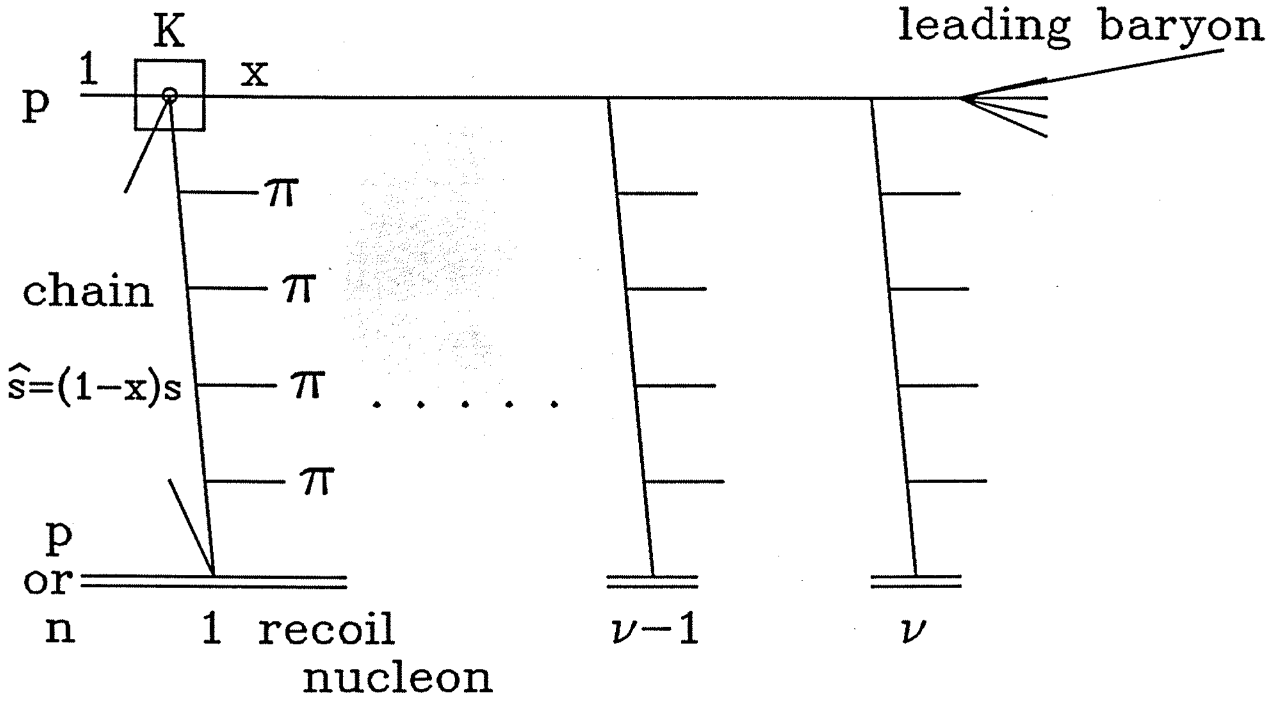

K
p
1
x
leading baryon
π
chain
π
ŝ=(1−x)s
π
π
p
or
n
1 recoil
nucleon
ν−1
ν

Fig.4−1

MCM event generator flow chart

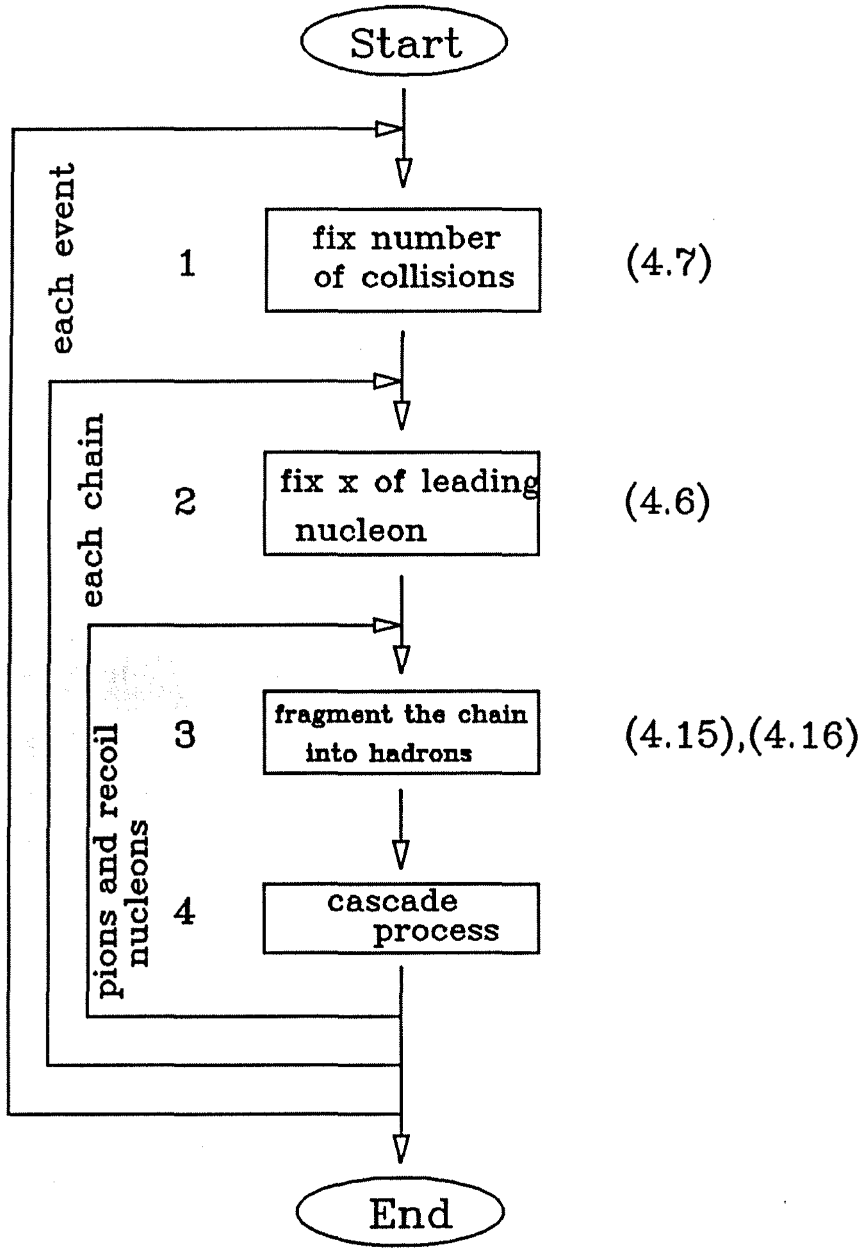

Fig.4−2

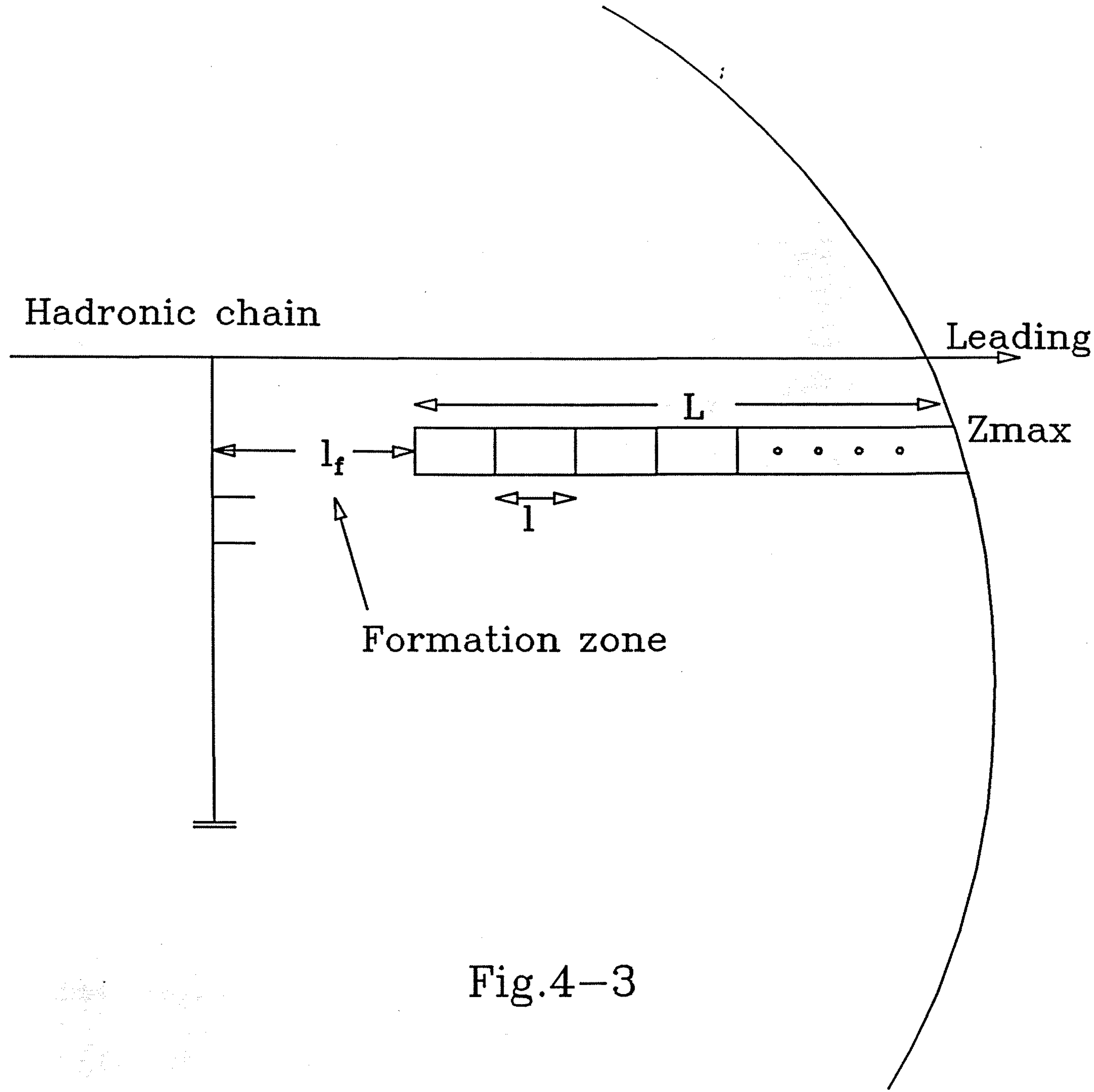

Fig.4—3

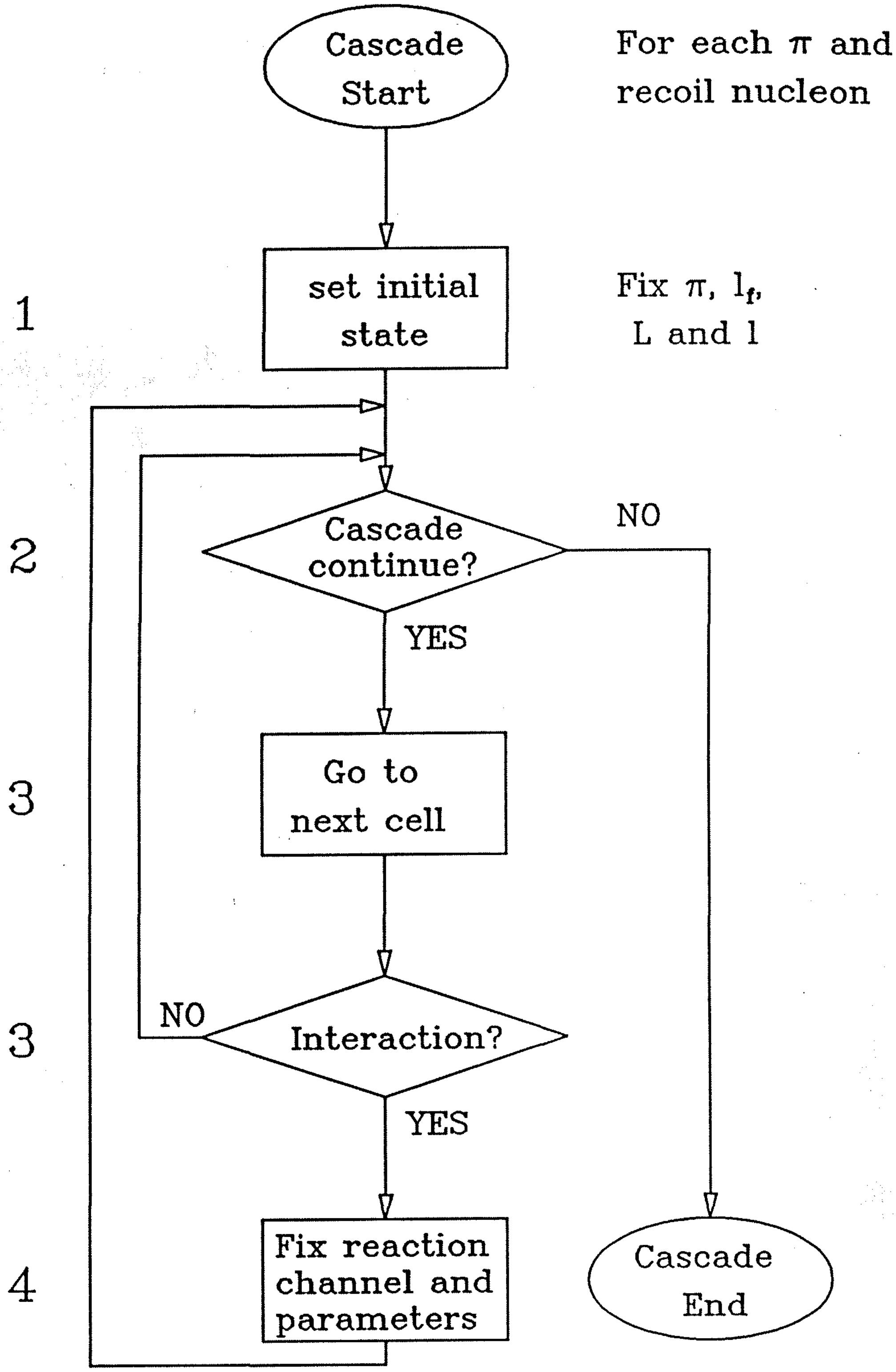
Cascade Start
For each π and recoil nucleon
1
set initial state
Fix π, l_f, L and l
2
Cascade continue?
NO
YES
3
Go to next cell
3
NO
Interaction?
YES
4
Fix reaction channel and parameters
Cascade End

Fig.4–4

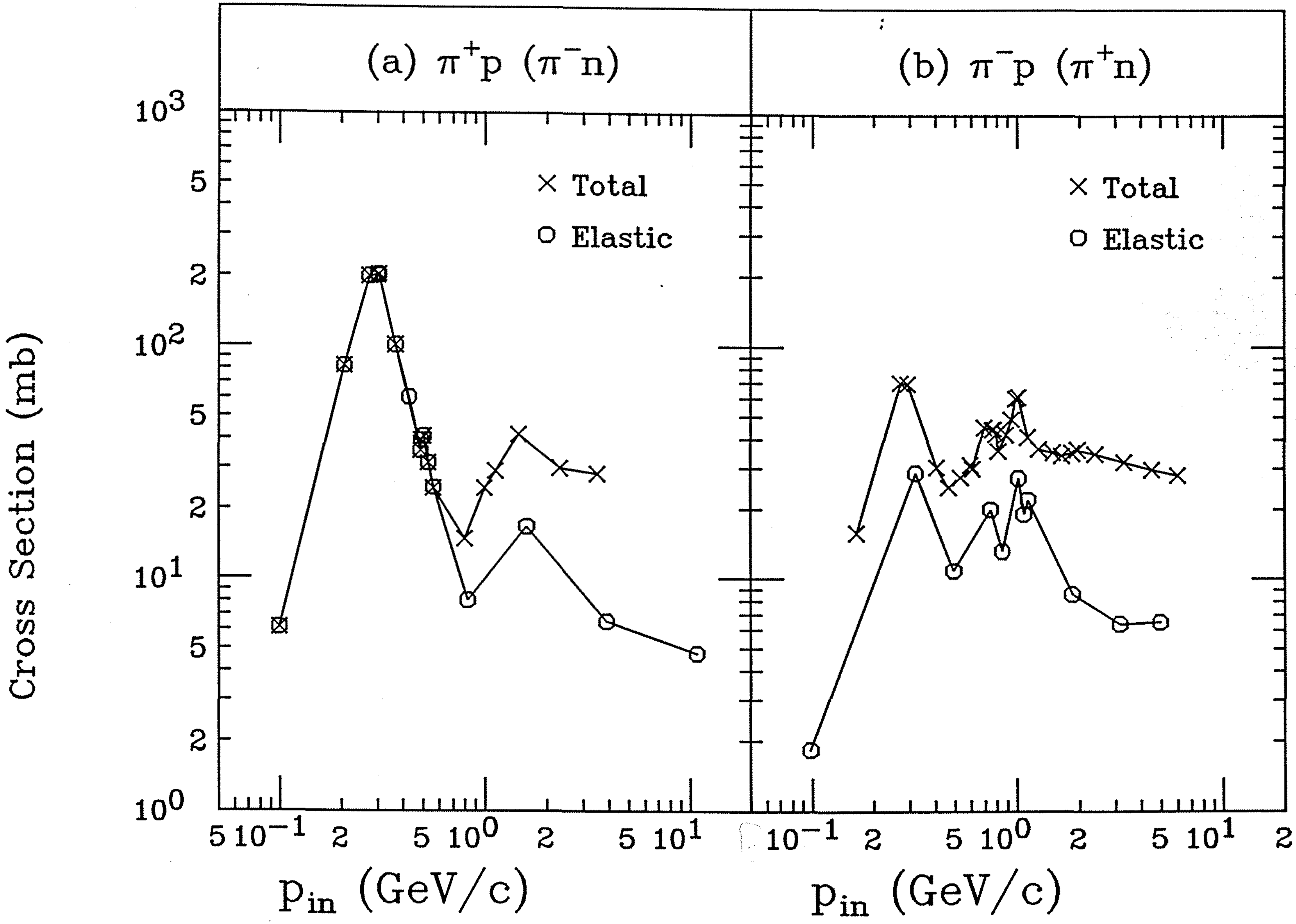

Fig.4–5

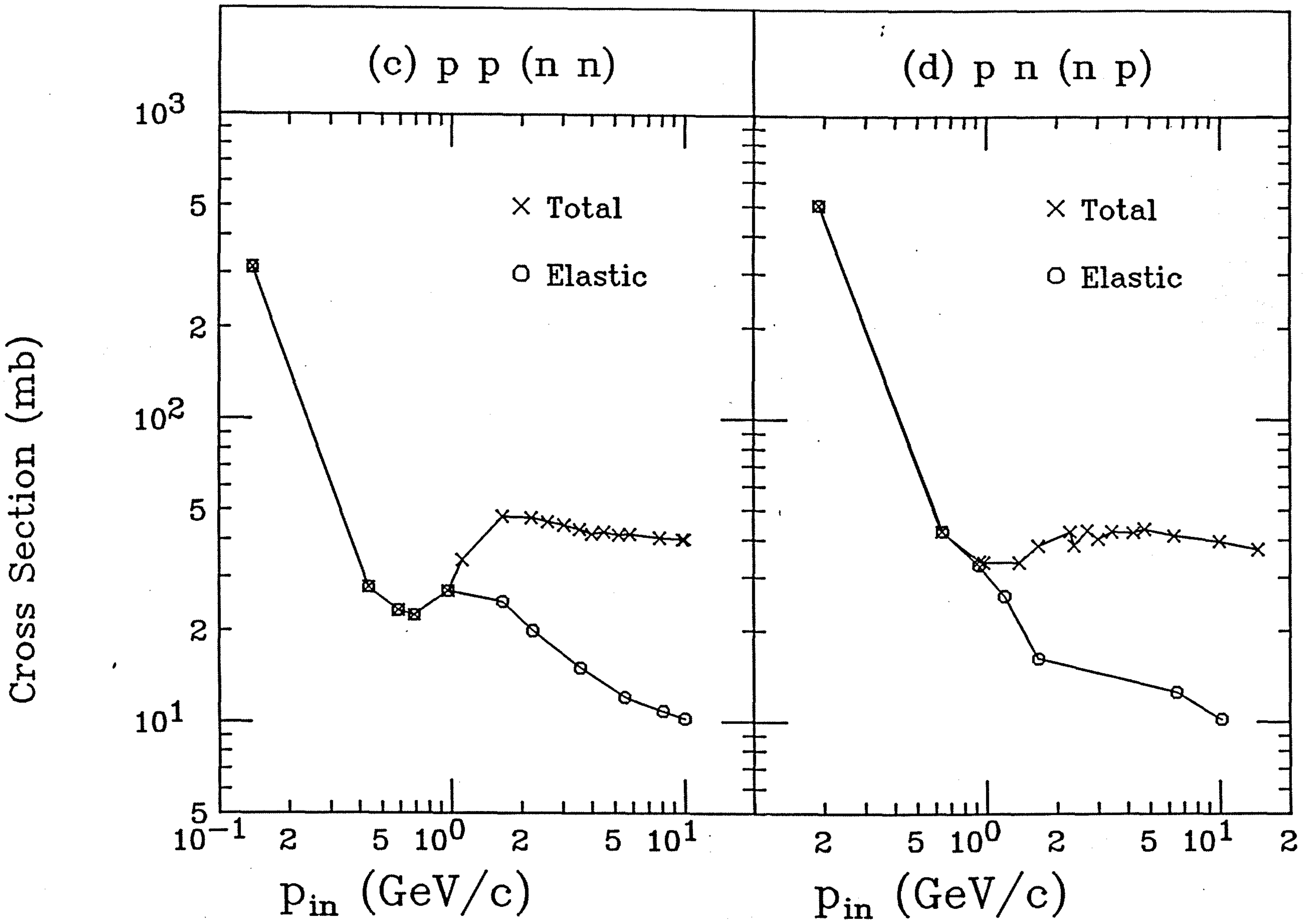
(c) p p (n n)
(d) p n (n p)
× Total
○ Elastic
× Total
○ Elastic
Cross Section (mb)
10³
5
2
10²
5
2
10¹
5
10⁻¹
2
5
10⁰
2
5
10¹
2
5
10⁰
2
5
10¹
2
pin (GeV/c)
pin (GeV/c)

Fig.4—5

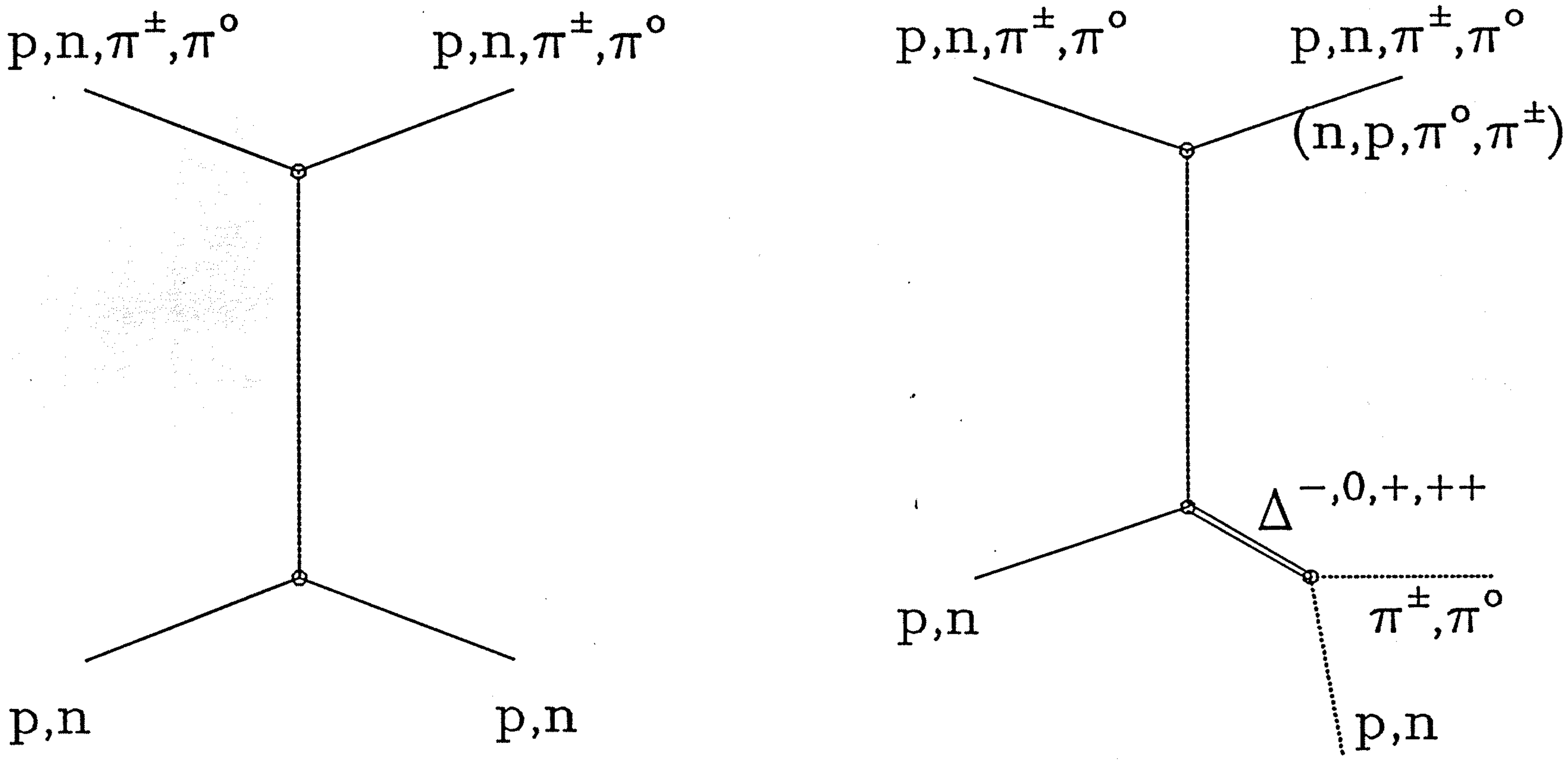

(a) Elastic (b) Inelastic

Fig.4−6

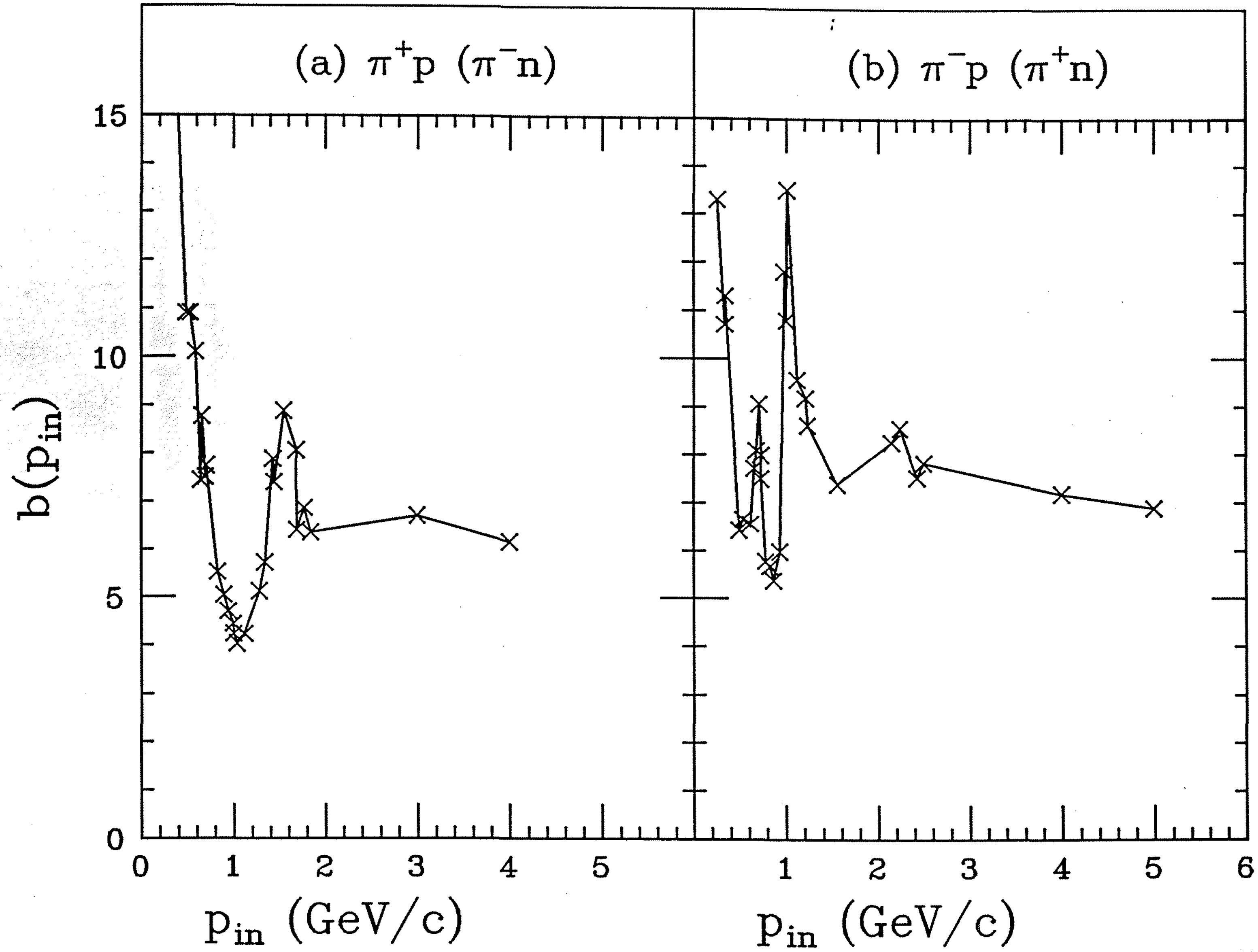

Fig.4—7

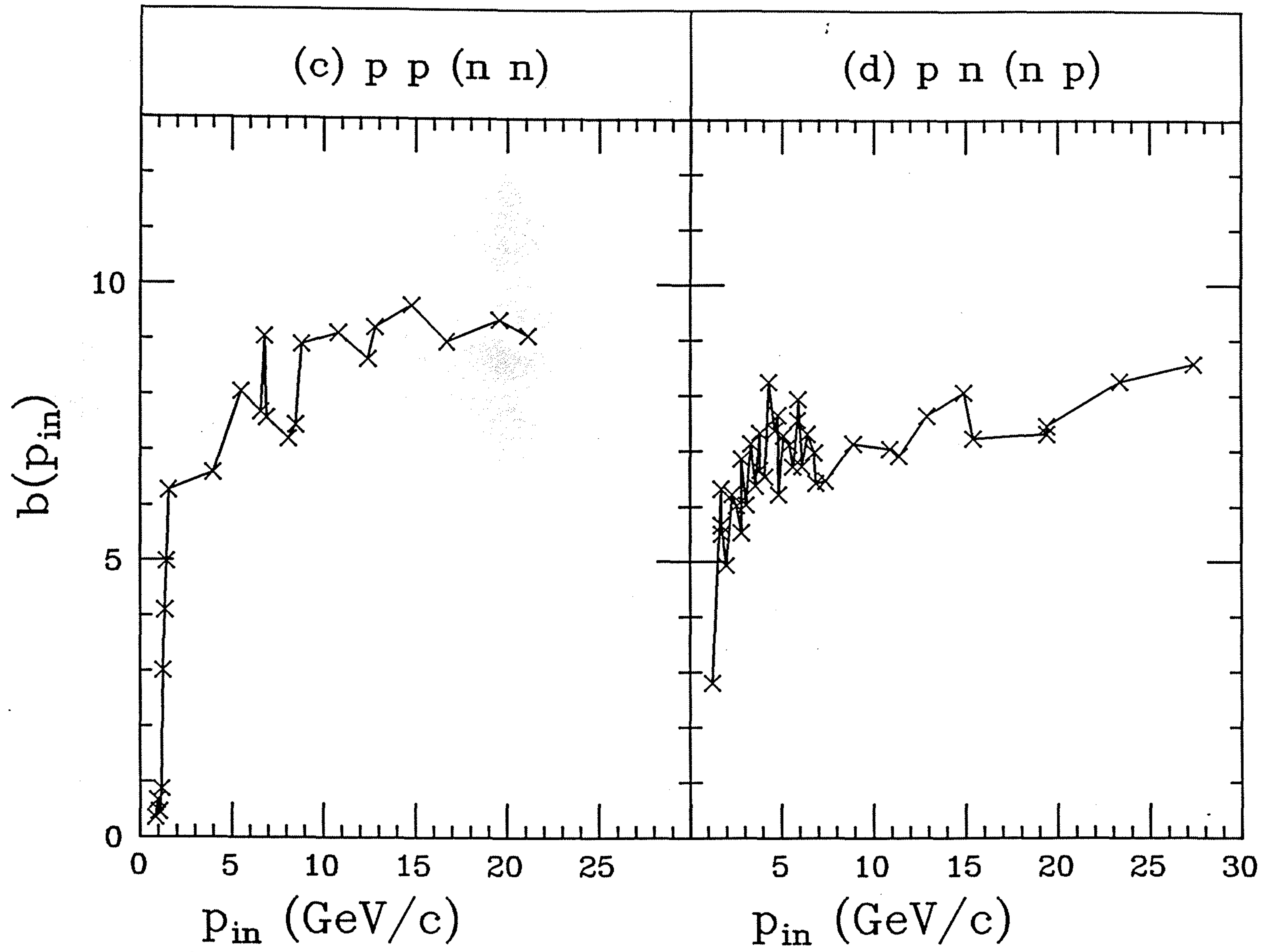

Fig.4–7

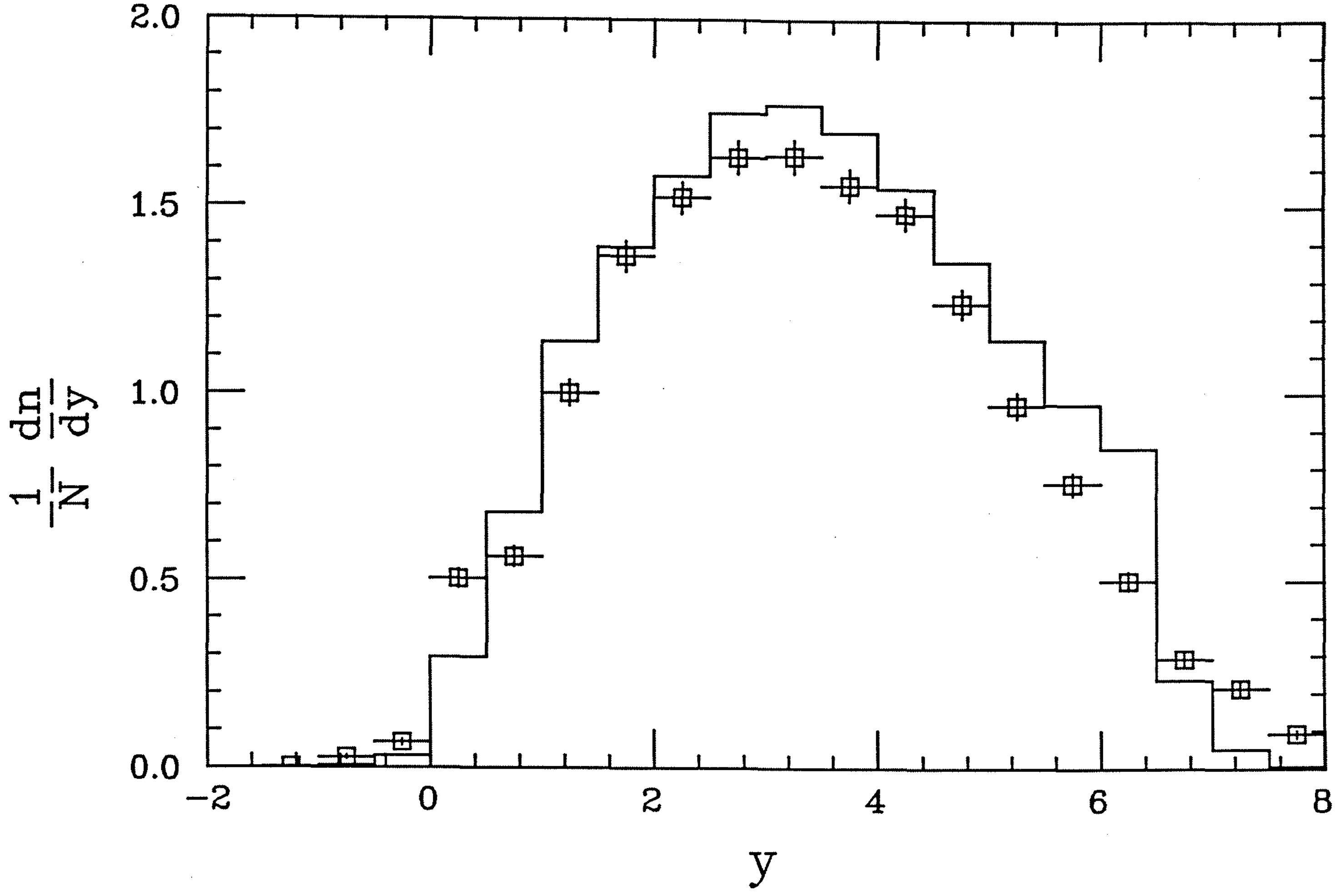

Fig.4−8

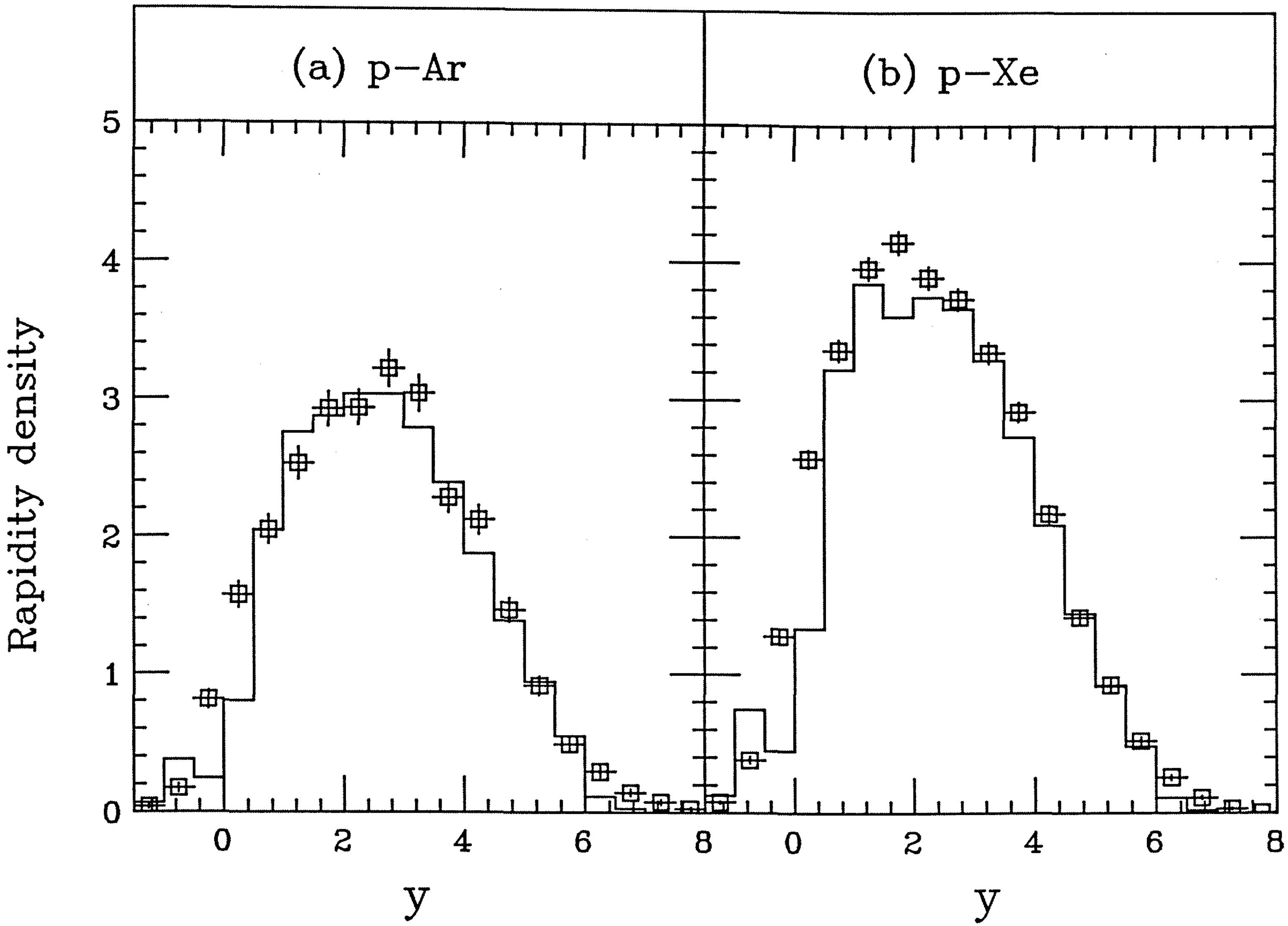

Fig.4−9

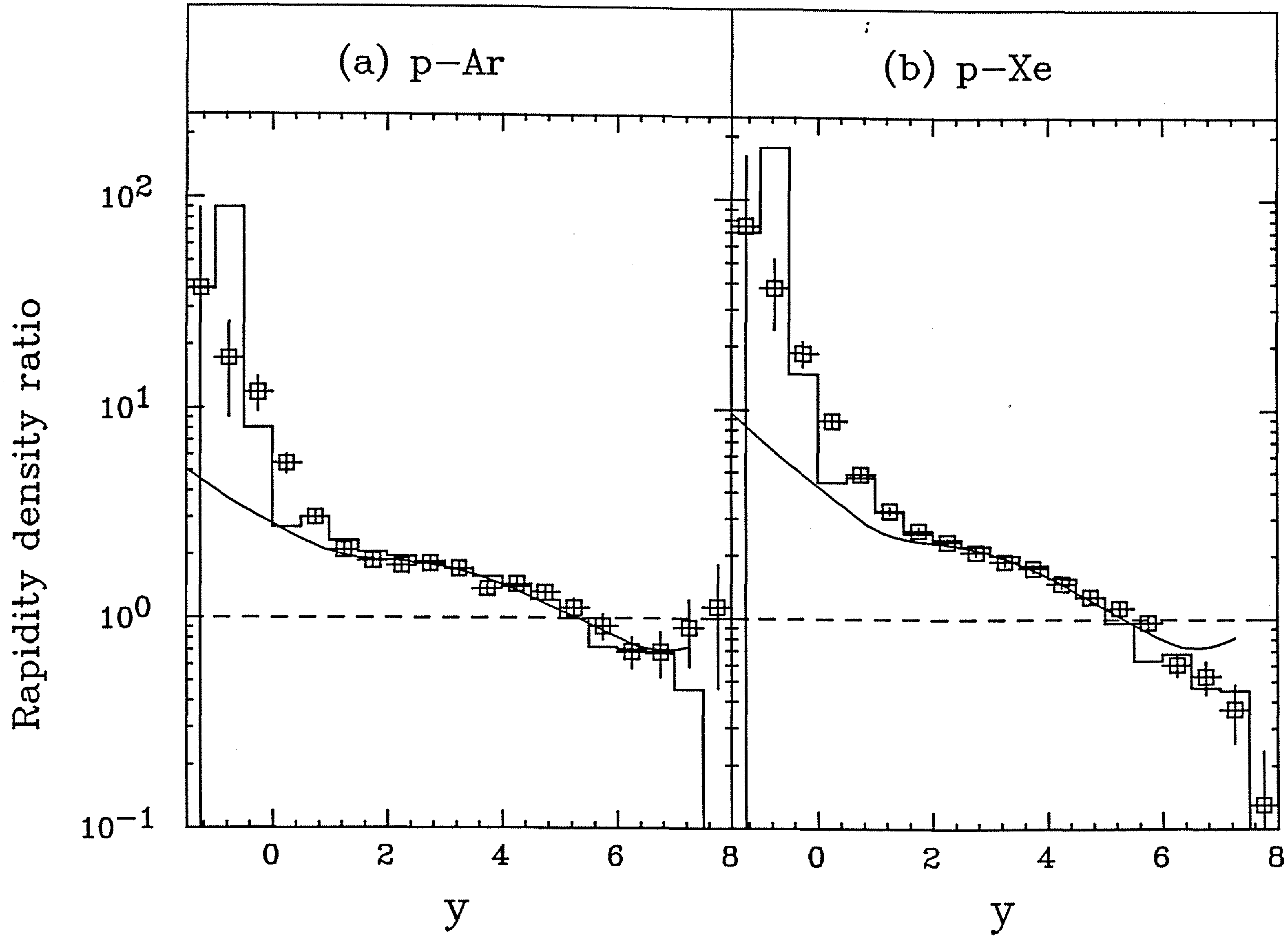
(a) p−Ar
(b) p−Xe
Rapidity density ratio
10^2
10^1
10^0
10^−1
0
2
4
6
8
0
2
4
6
8
y
y

Fig.4−10

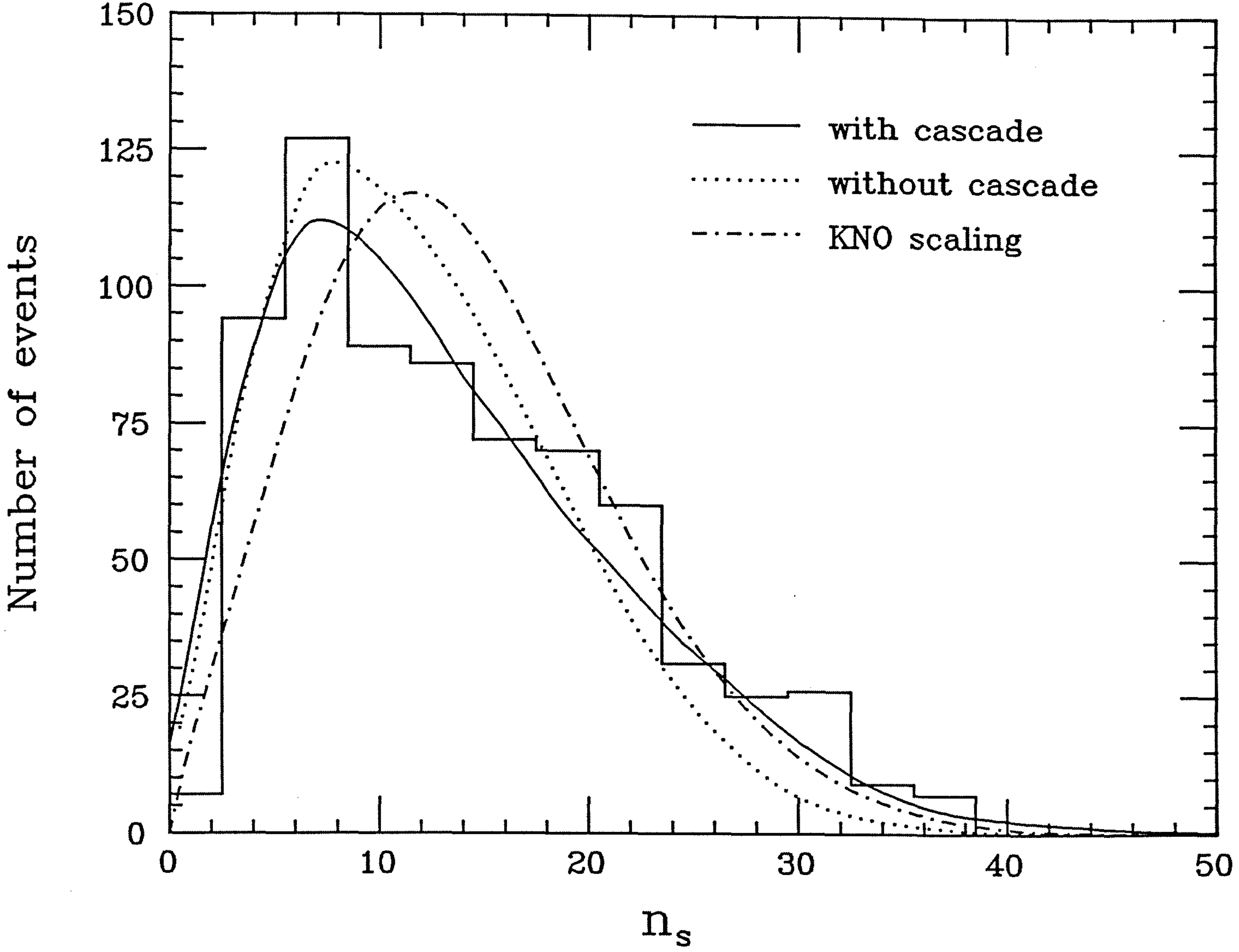

150
125
100
75
50
25
0
Number of events
with cascade
without cascade
KNO scaling
0
10
20
30
40
50
n_s

Fig.4−11

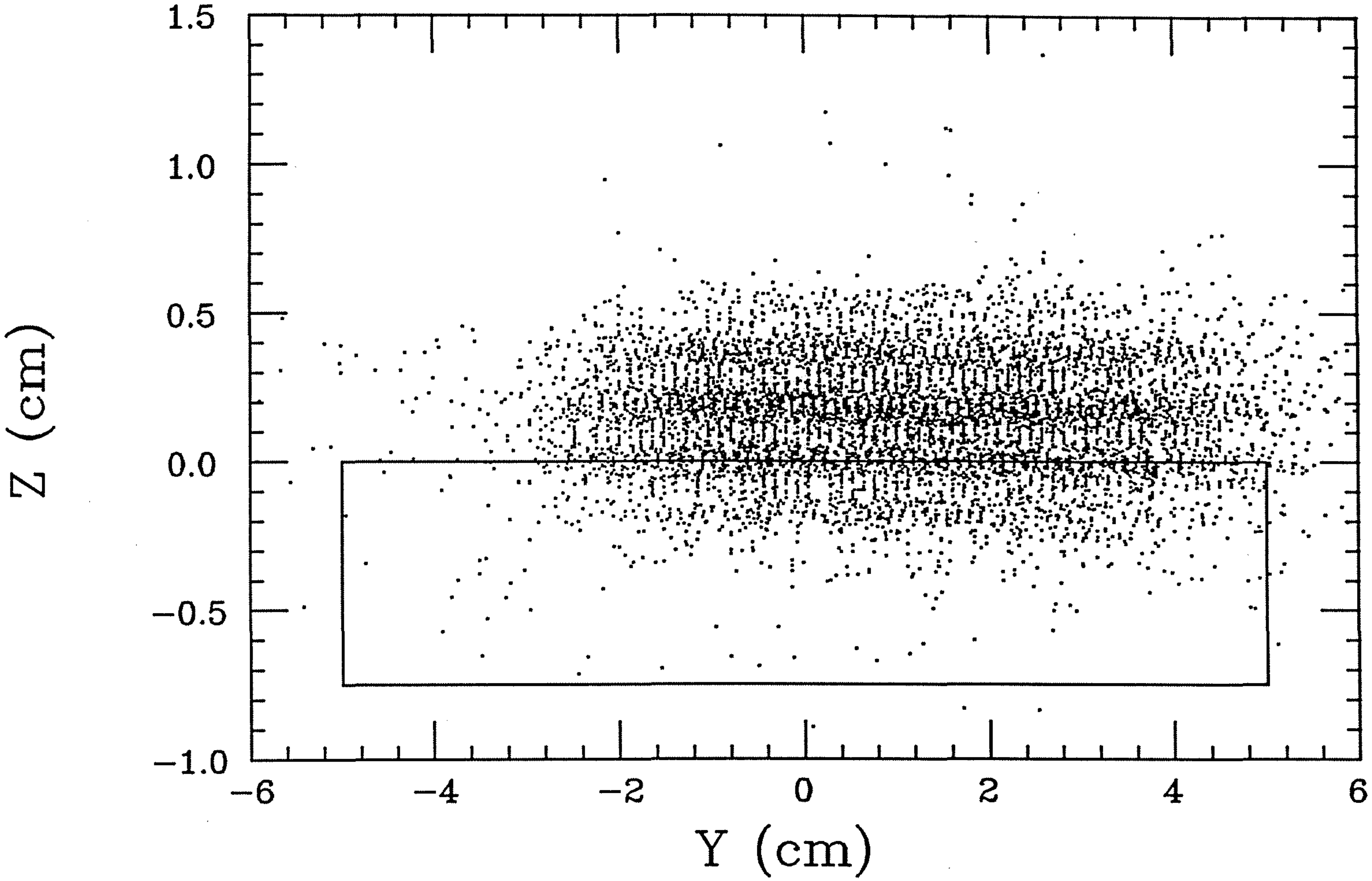

Fig.5−1

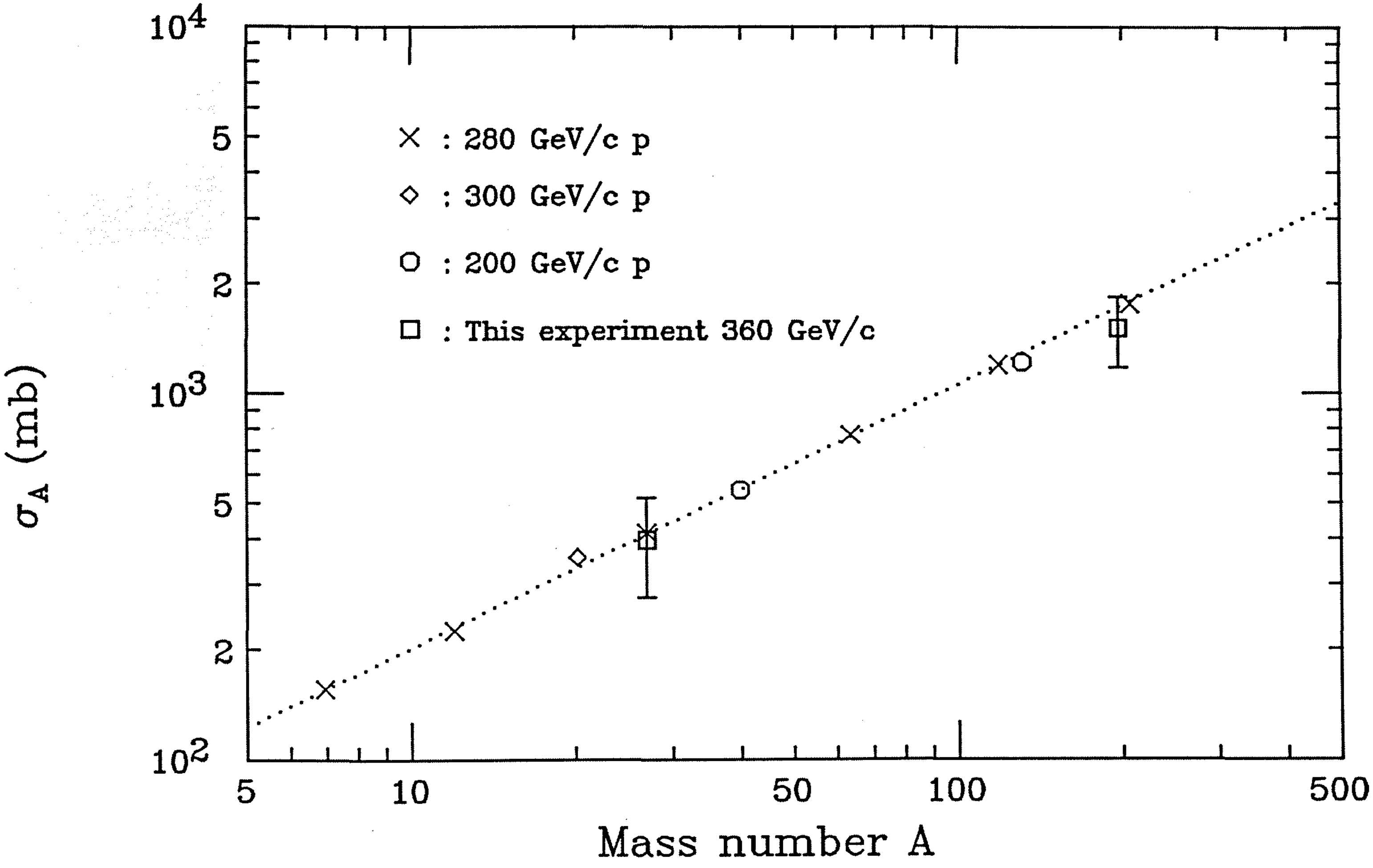

× : 280 GeV/c p
◇ : 300 GeV/c p
○ : 200 GeV/c p
□ : This experiment 360 GeV/c
σ_A (mb)
Mass number A

Fig.5−2

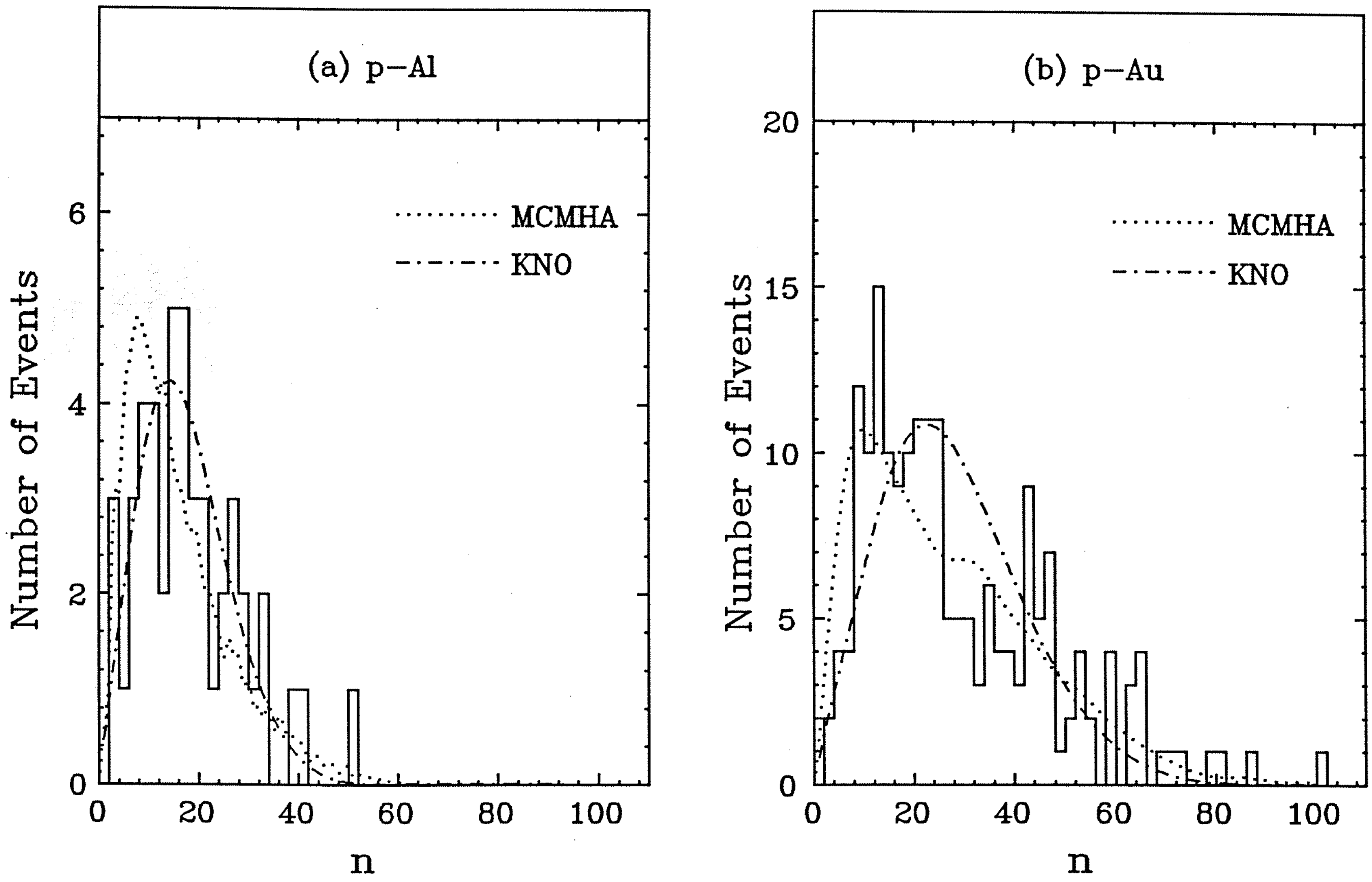
(a) p−Al
MCMHA
KNO
Number of Events
n
(b) p−Au
MCMHA
KNO
Number of Events
n

Fig.5−3

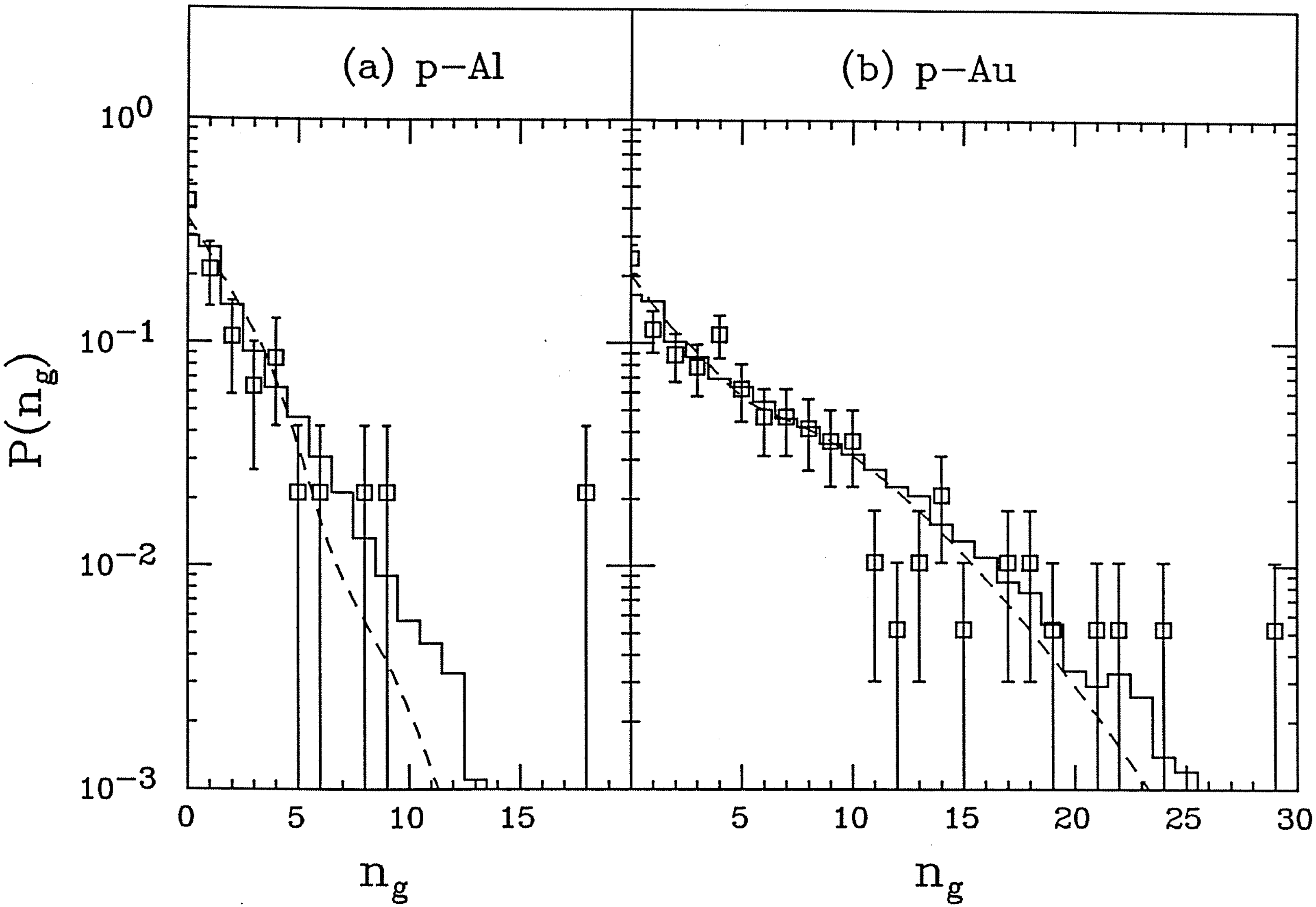

Fig.5−4

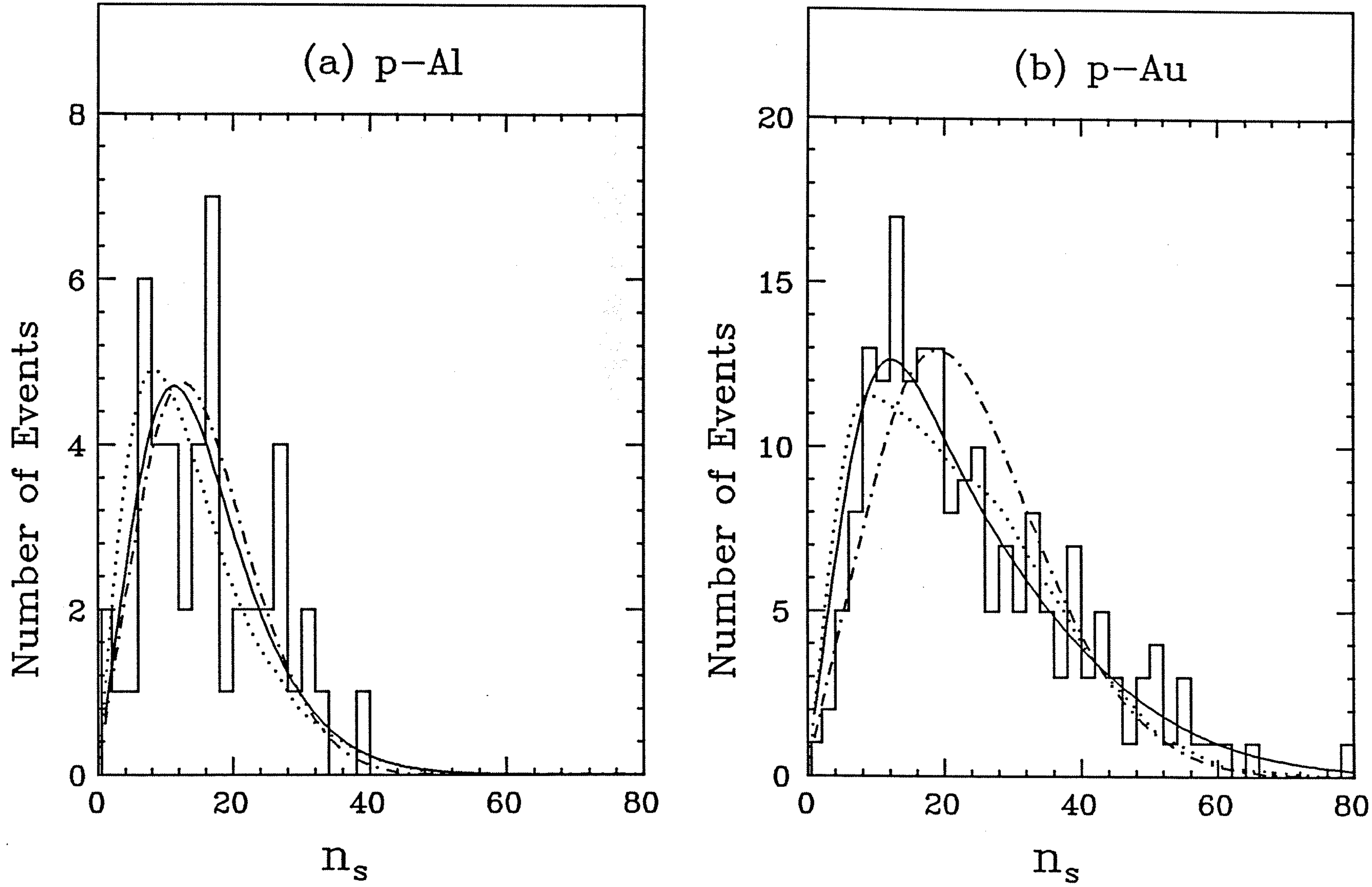

Fig.5−5

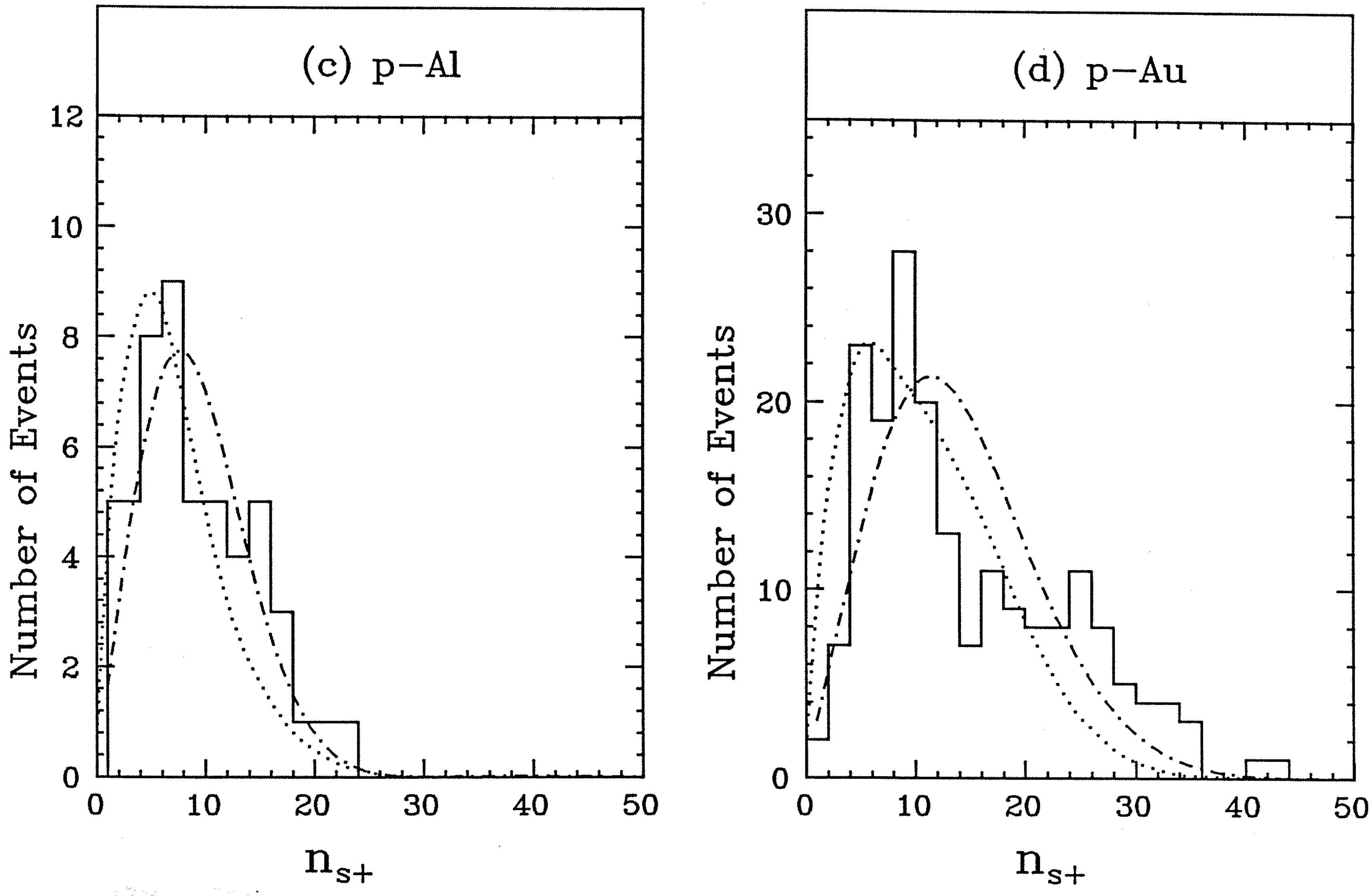

(c) p−Al
(d) p−Au
Number of Events
Number of Events
0
2
4
6
8
10
12
0
10
20
30
0
10
20
30
40
50
0
10
20
30
40
50
n_{s+}
n_{s+}

Fig.5−5

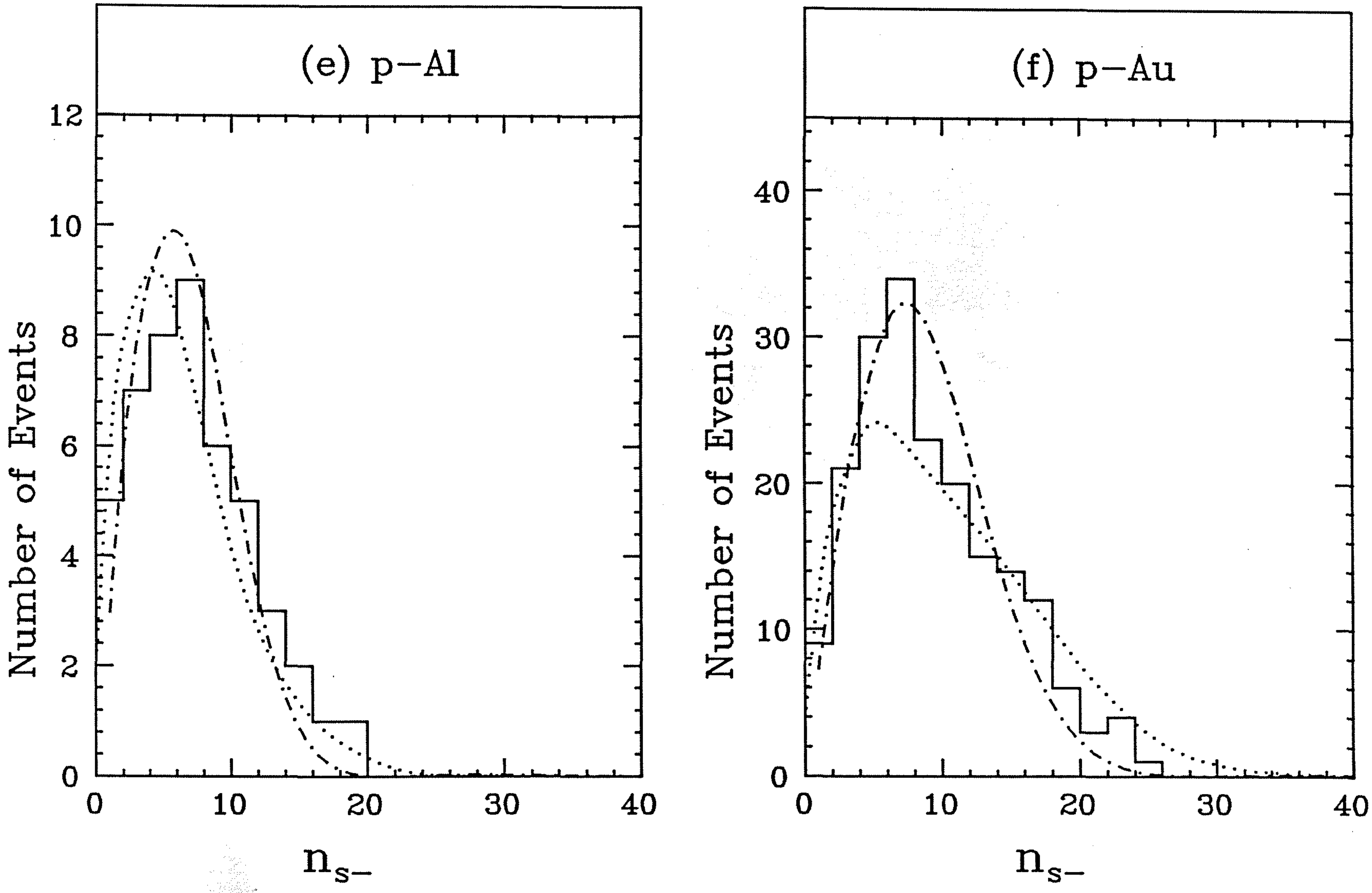
(e) p−Al
Number of Events
12
10
8
6
4
2
0
0
10
20
30
40
n_{s−}
(f) p−Au
Number of Events
40
30
20
10
0
0
10
20
30
40
n_{s−}

Fig.5−5

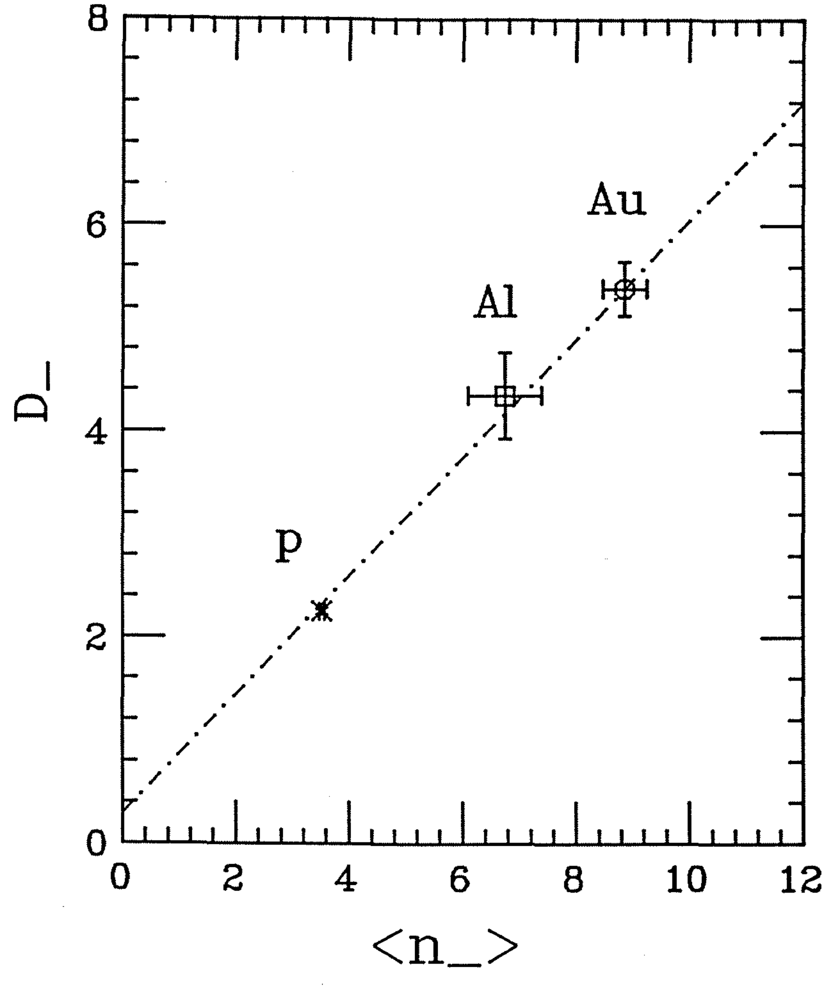

Fig.5−6

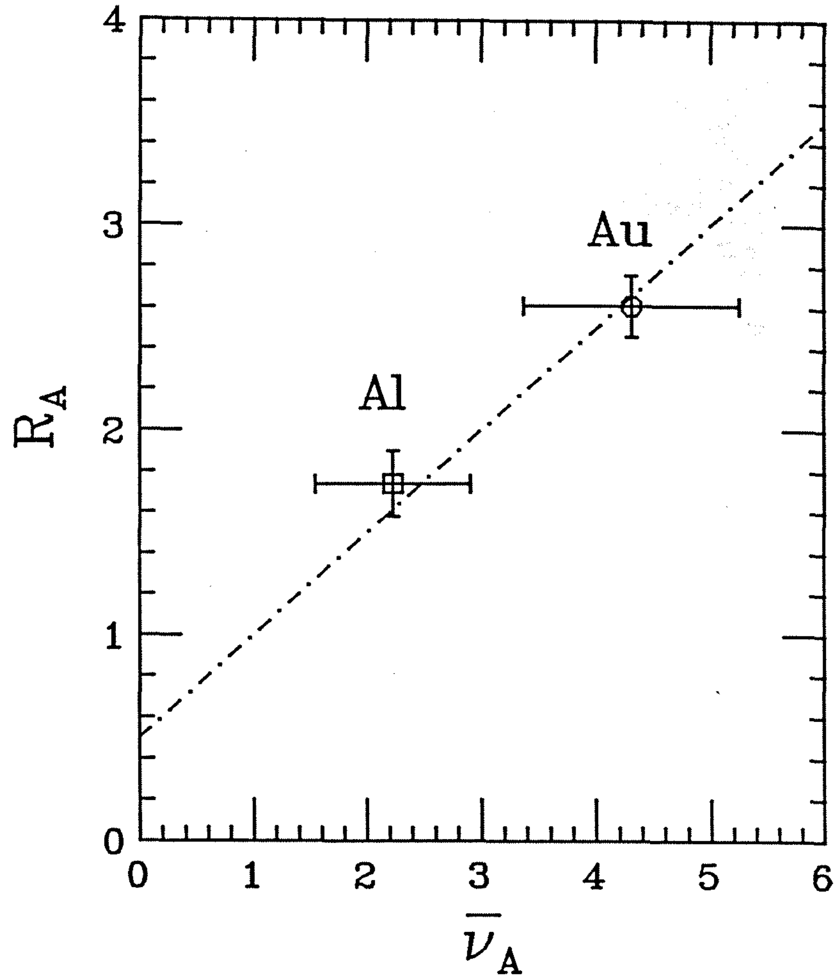

Fig.5−7

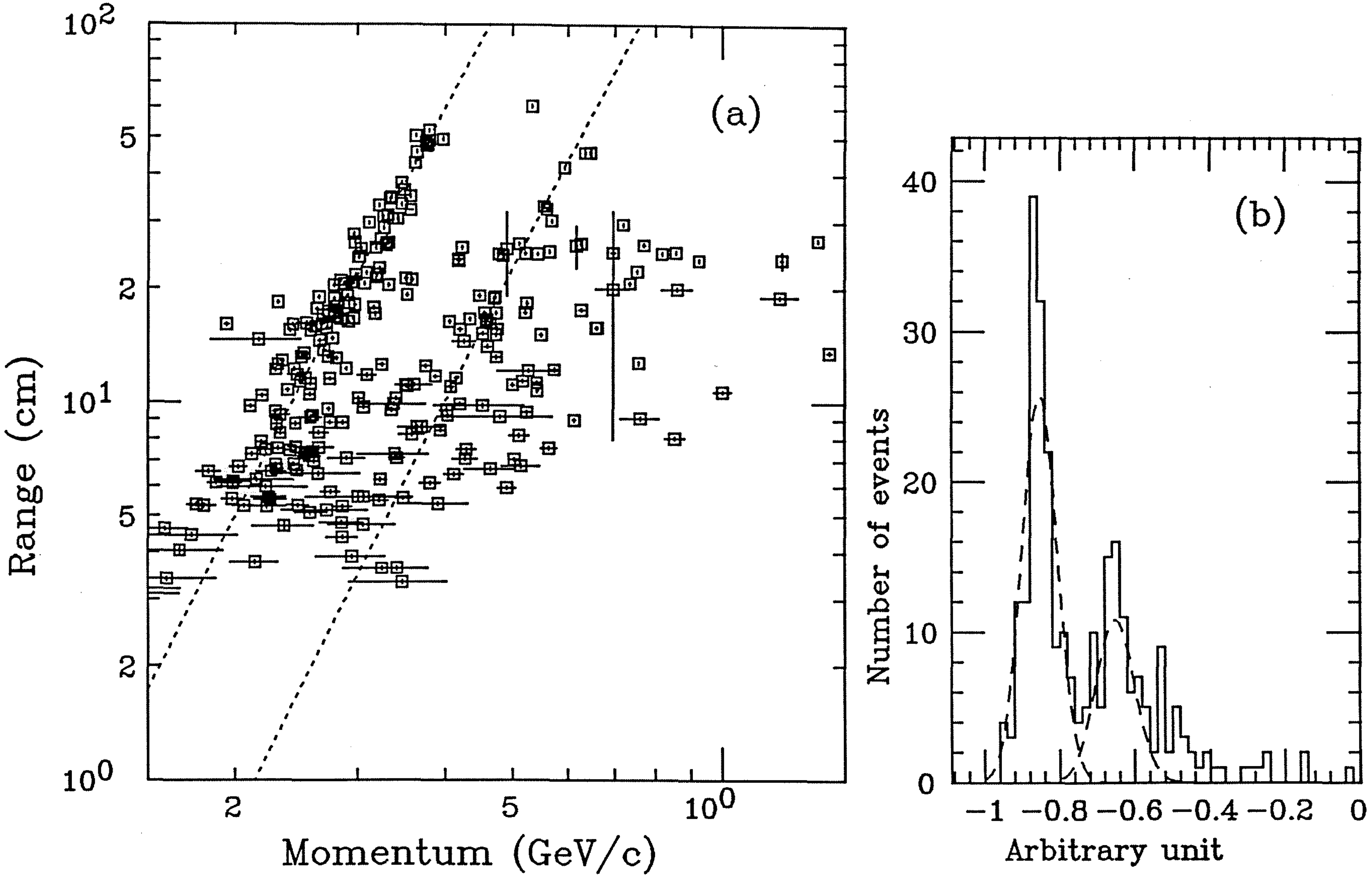

(a)
Range (cm)
10^2
5
2
10^1
5
2
10^0
2
5
10^0
Momentum (GeV/c)
(b)
Number of events
40
30
20
10
0
−1 −0.8 −0.6 −0.4 −0.2 0
Arbitrary unit

Fig.5−8

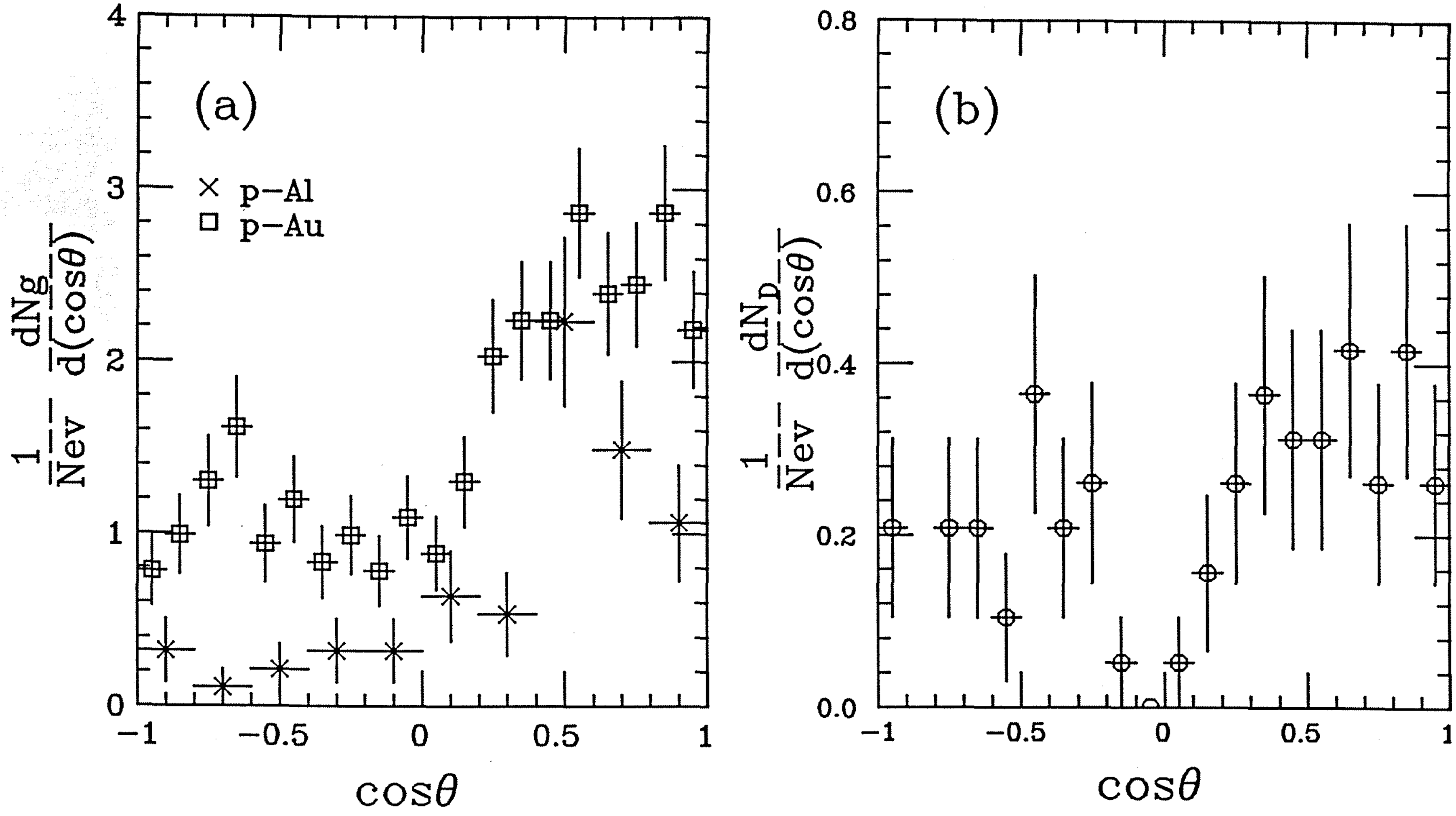
(a)
× p−Al
□ p−Au
$\frac{1}{N_{ev}} \frac{dN_g}{d(\cos\theta)}$
0
1
2
3
4
−1
−0.5
0
0.5
1
cosθ
(b)
$\frac{1}{N_{ev}} \frac{dN_D}{d(\cos\theta)}$
0.0
0.2
0.4
0.6
0.8
−1
−0.5
0
0.5
1
cosθ

Fig.5−9

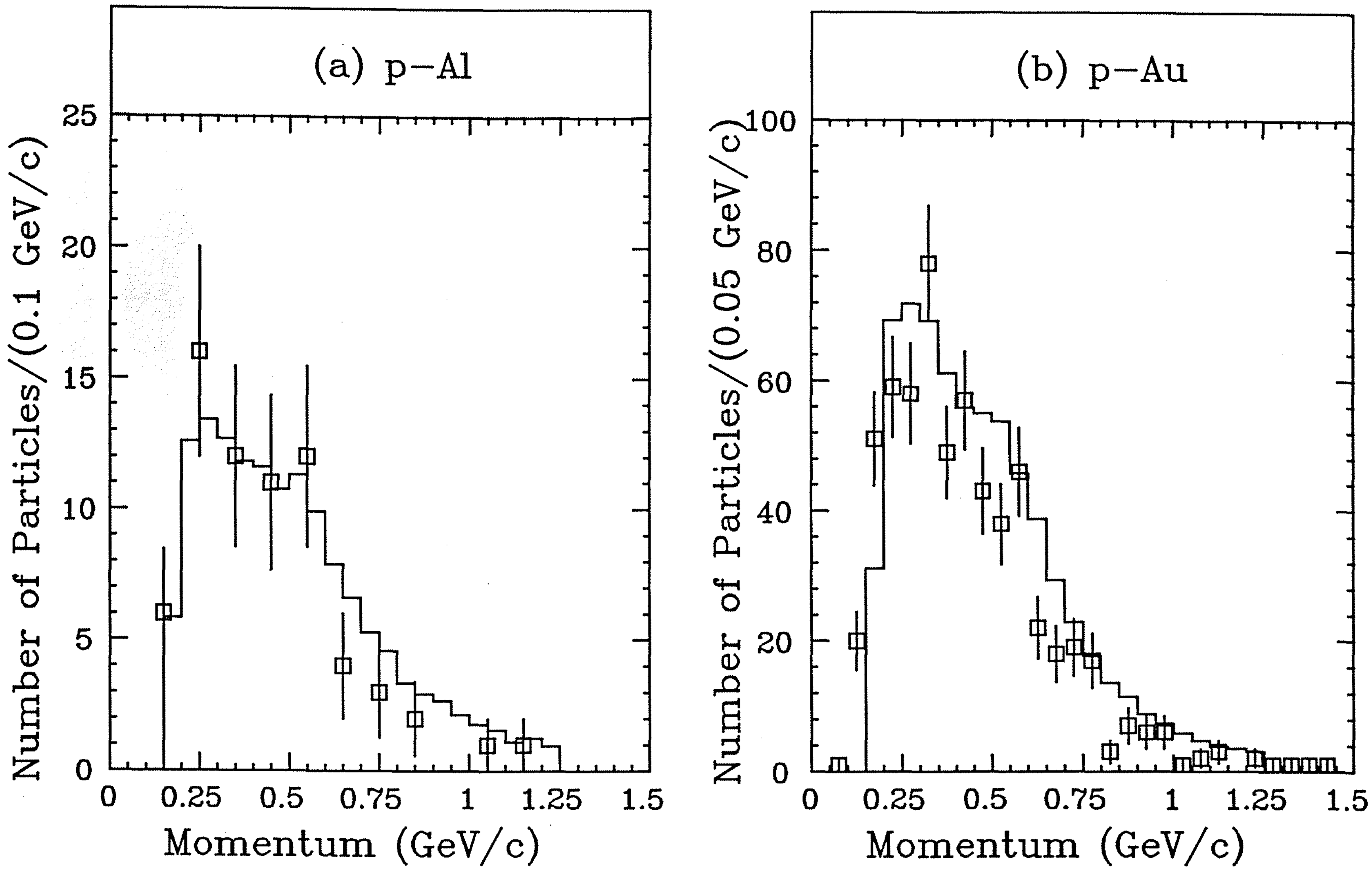
(a) p−Al
(b) p−Au
Number of Particles/(0.1 GeV/c)
Number of Particles/(0.05 GeV/c)
Momentum (GeV/c)
Momentum (GeV/c)
0
5
10
15
20
25
0
20
40
60
80
100
0
0.25
0.5
0.75
1
1.25
1.5

Fig.5−10

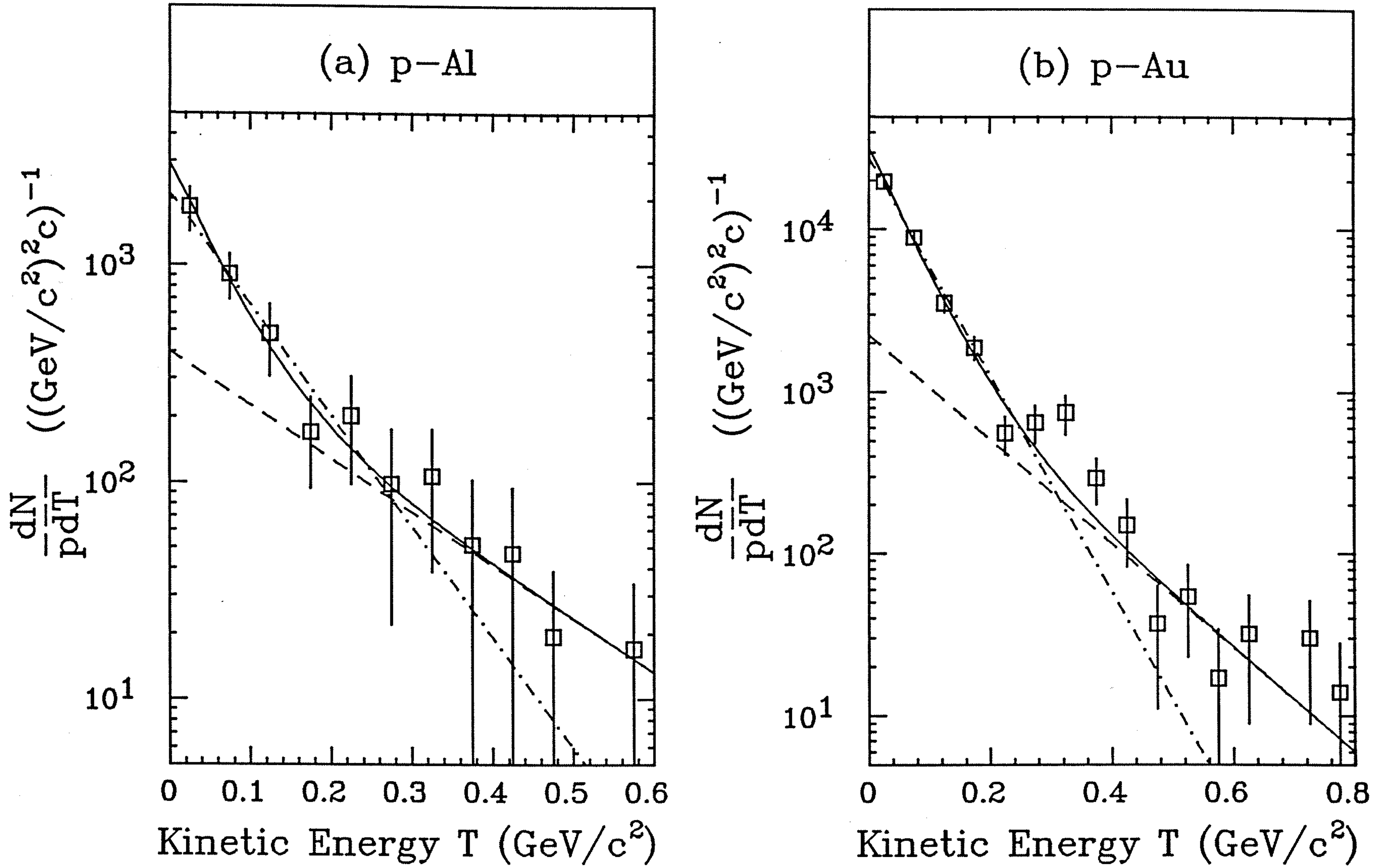
(a) p−Al
(b) p−Au
$\frac{dN}{pdT}$ $((GeV/c^2)^2c)^{-1}$
10^1
10^2
10^3
10^4
0
0.1
0.2
0.3
0.4
0.5
0.6
0.8
Kinetic Energy T (GeV/c^2)

Fig.5−11

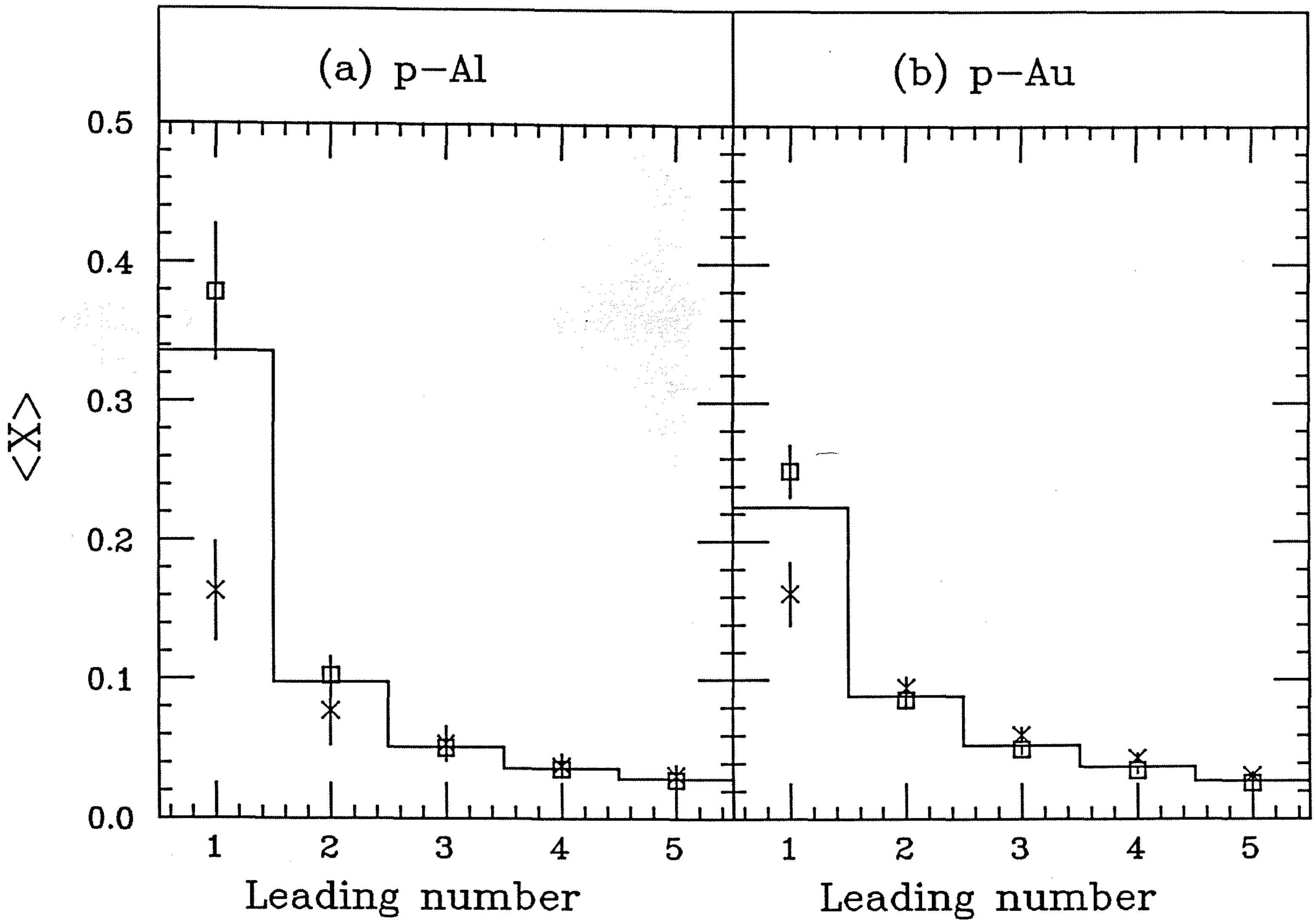
(a) p−Al
(b) p−Au
<X>
0.5
0.4
0.3
0.2
0.1
0.0
1
2
3
4
5
Leading number
Leading number

Fig.5−12

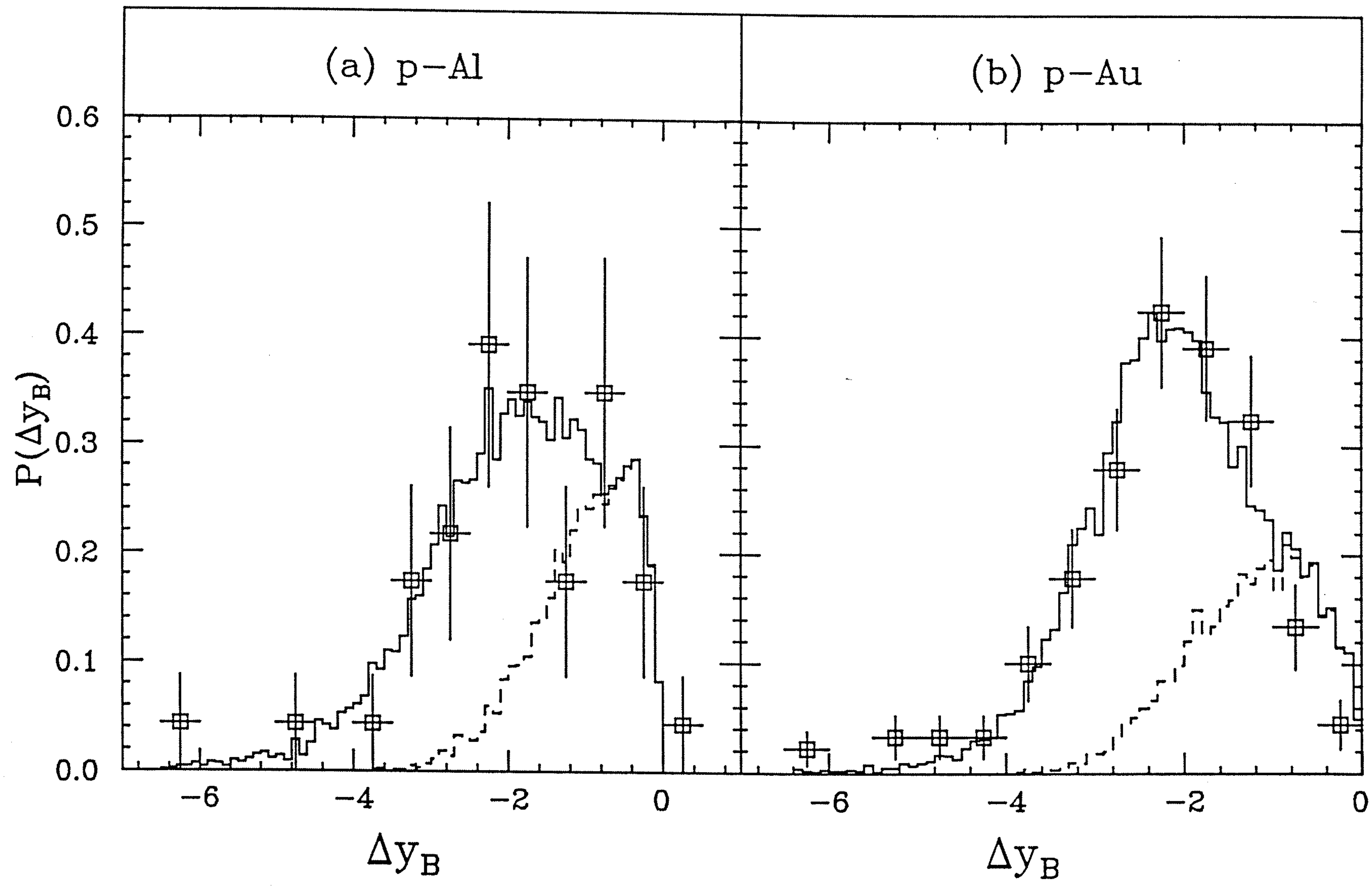

Fig.5−13

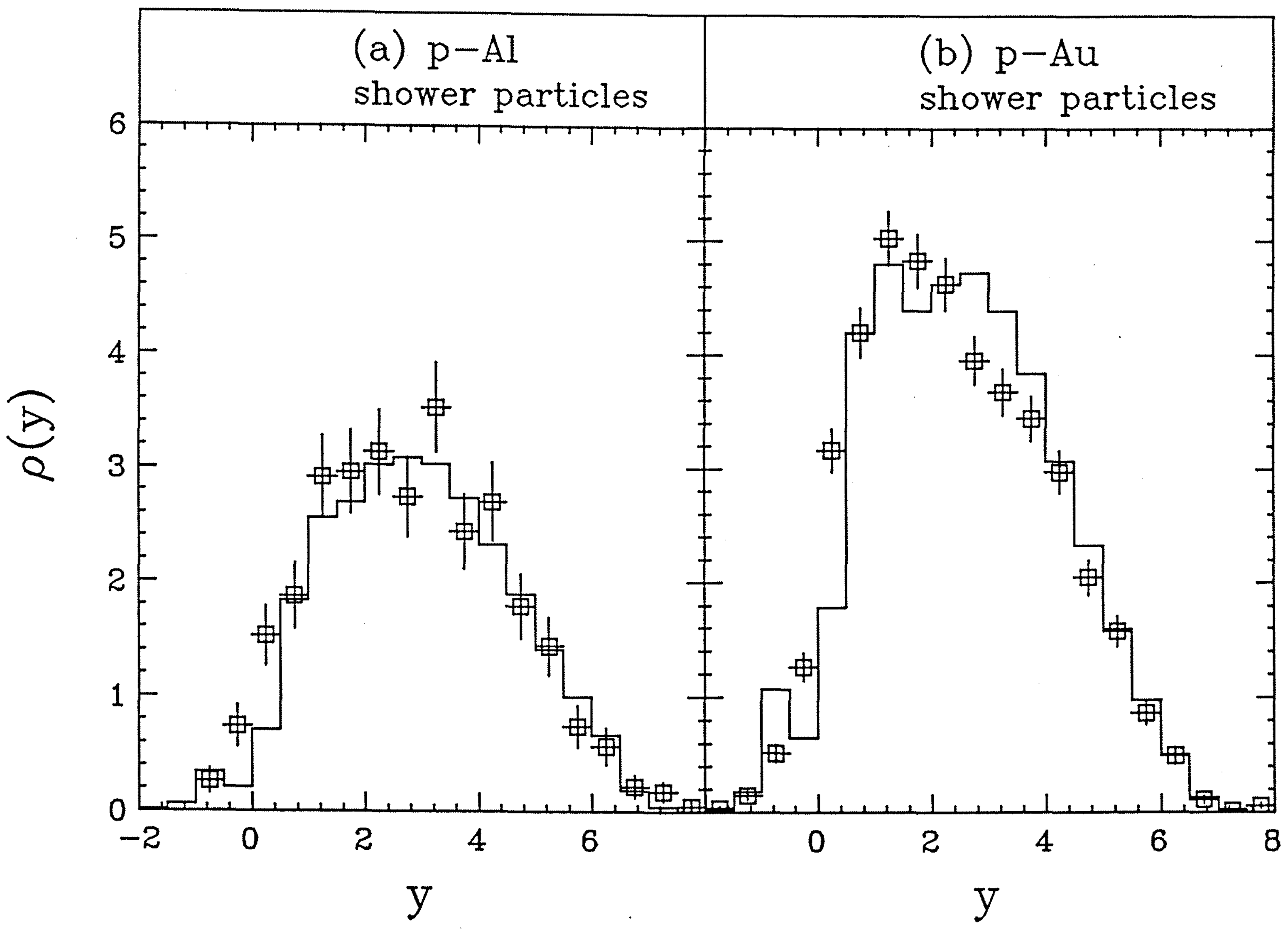

(a) p−Al
shower particles
(b) p−Au
shower particles
ρ(y)
6
5
4
3
2
1
0
−2
0
2
4
6
8
y
y

Fig.5−14

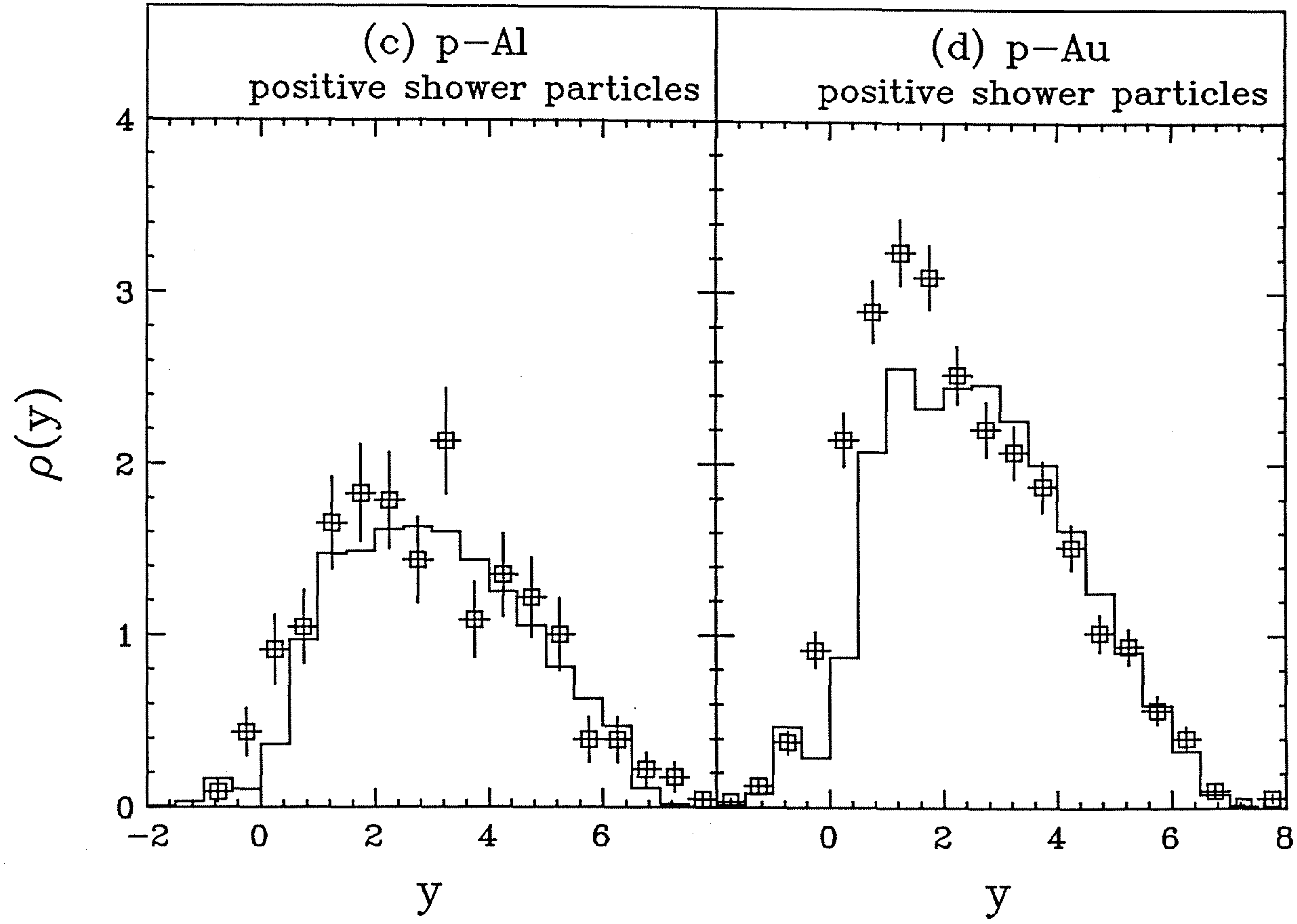
(c) p−Al
positive shower particles
(d) p−Au
positive shower particles
ρ(y)
4
3
2
1
0
−2
0
2
4
6
0
2
4
6
8
y
y

Fig.5−14

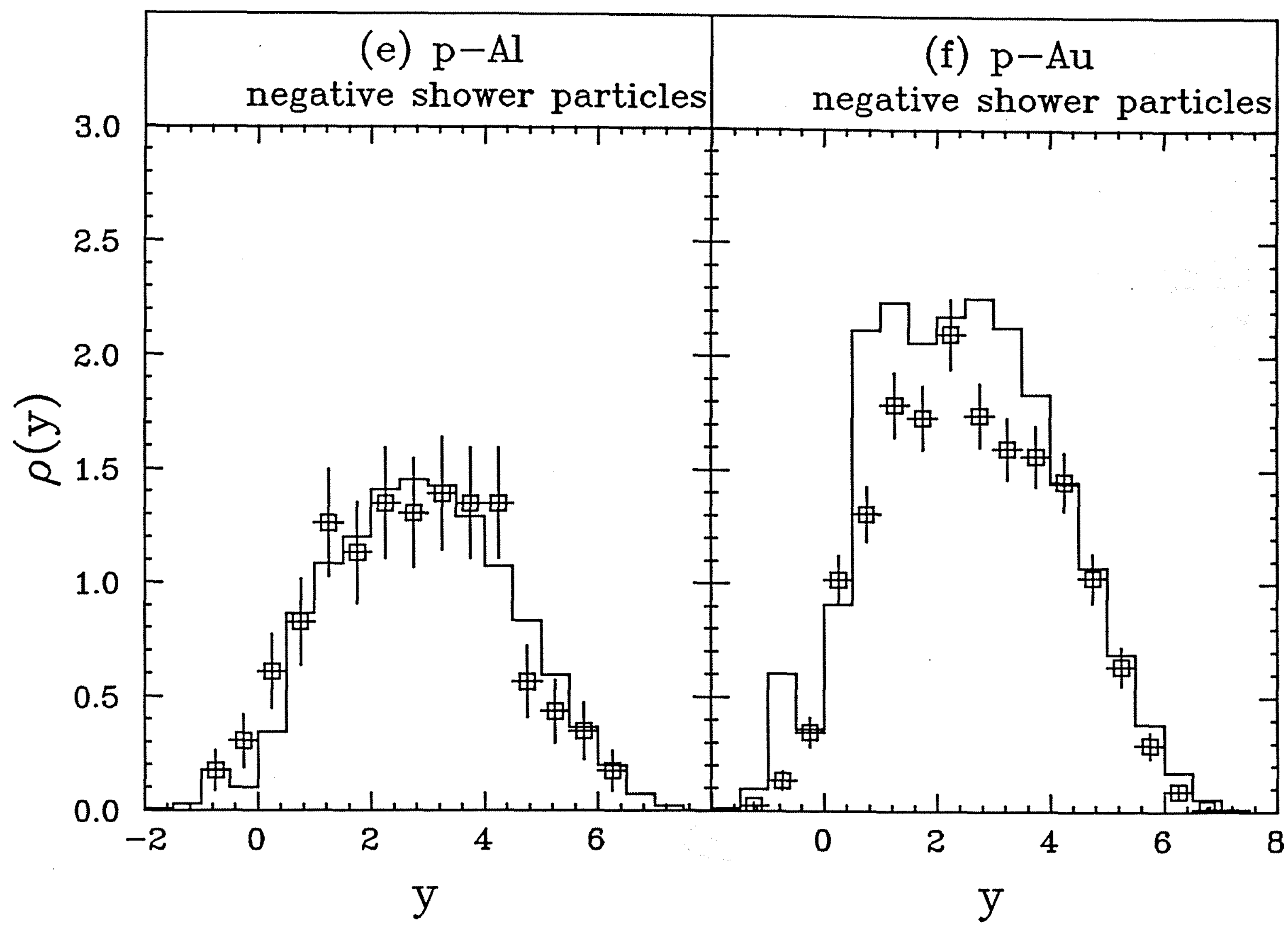
(e) p−Al
negative shower particles
(f) p−Au
negative shower particles
ρ(y)
3.0
2.5
2.0
1.5
1.0
0.5
0.0
−2
0
2
4
6
8
y
y

Fig.5−14

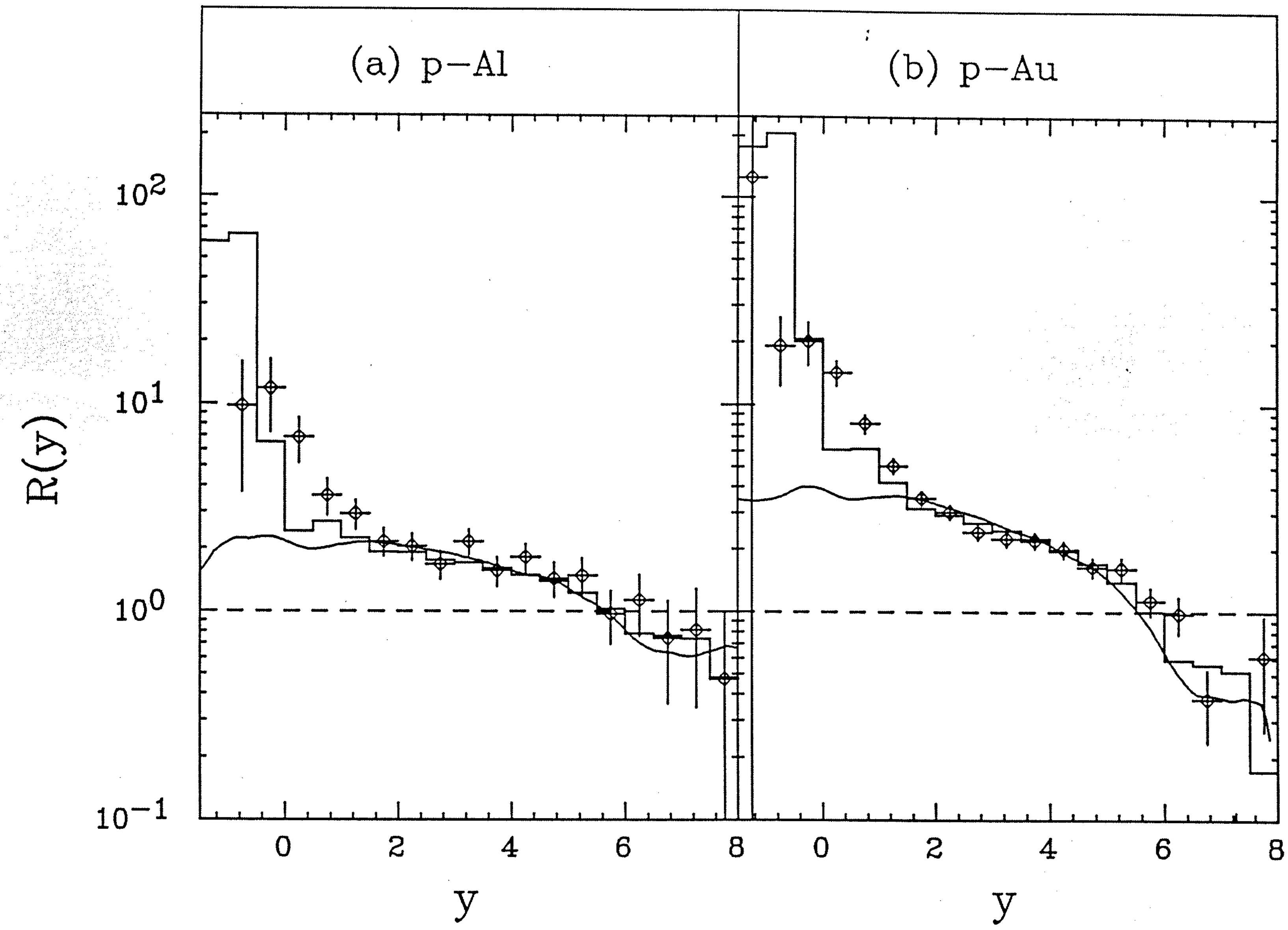

Fig.5−15

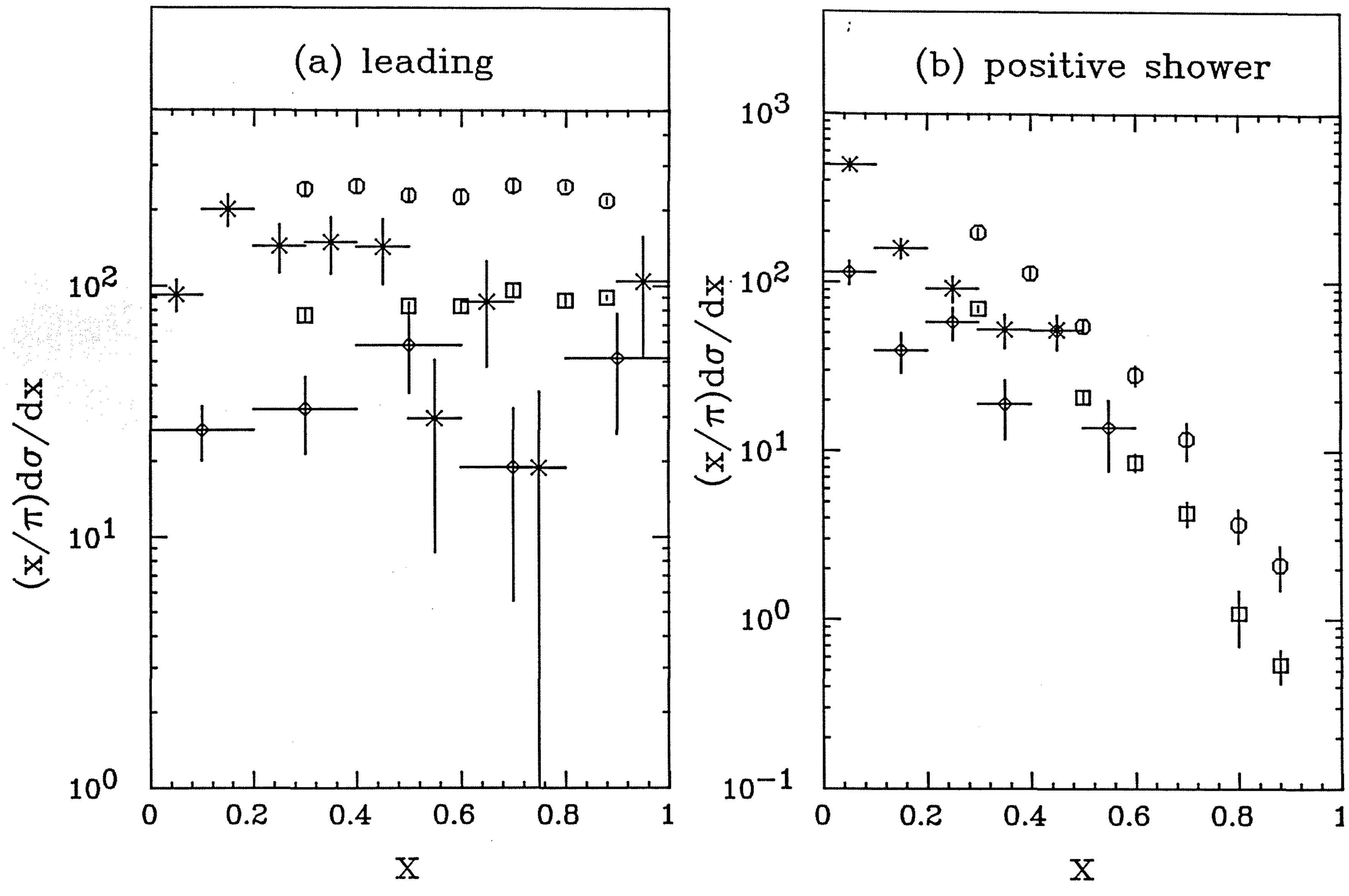

Fig.5−16

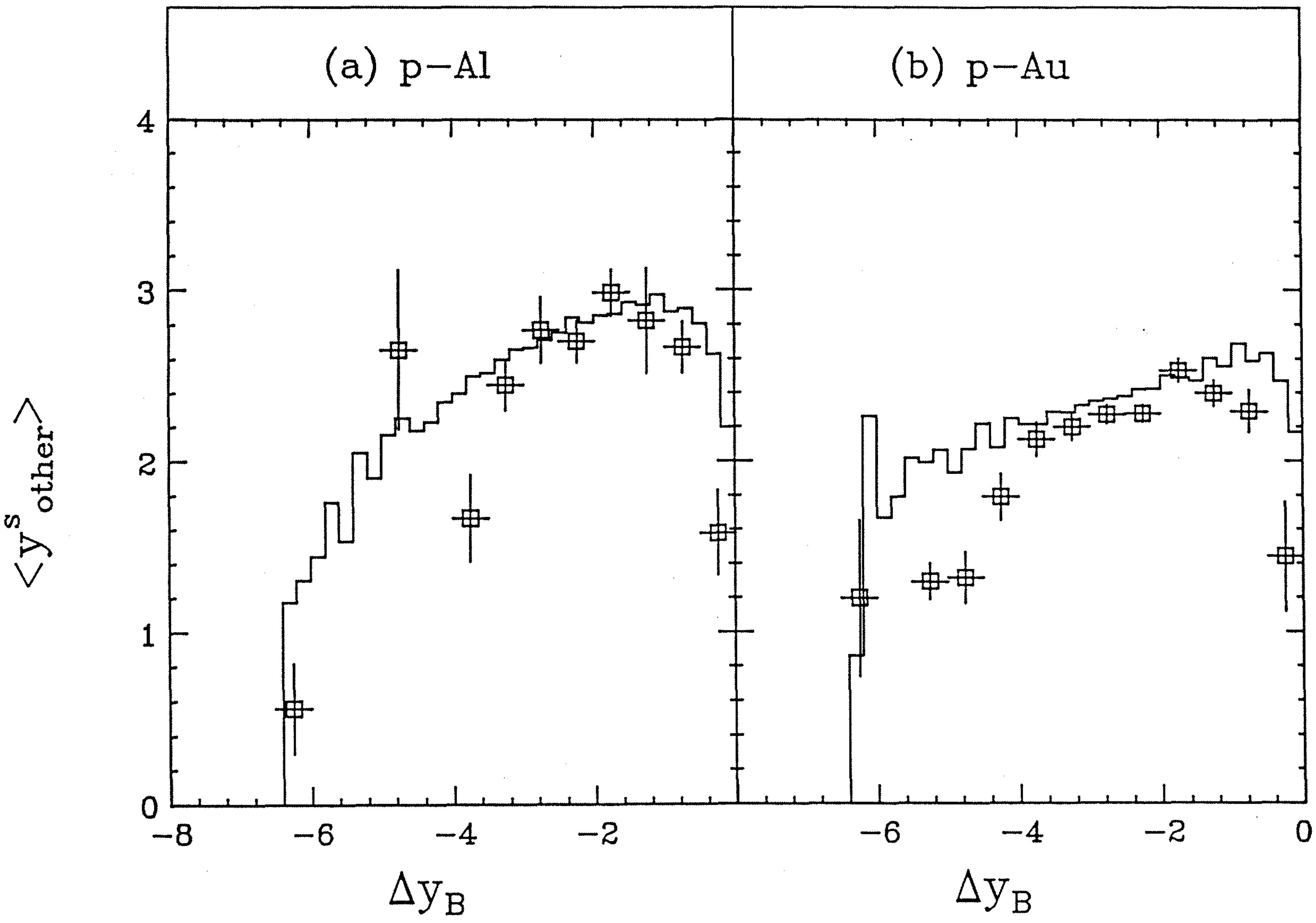
(a) p−Al
(b) p−Au
$\langle y^s_{other} \rangle$
4
3
2
1
0
−8
−6
−4
−2
0
Δy_B
Δy_B

Fig.5−17

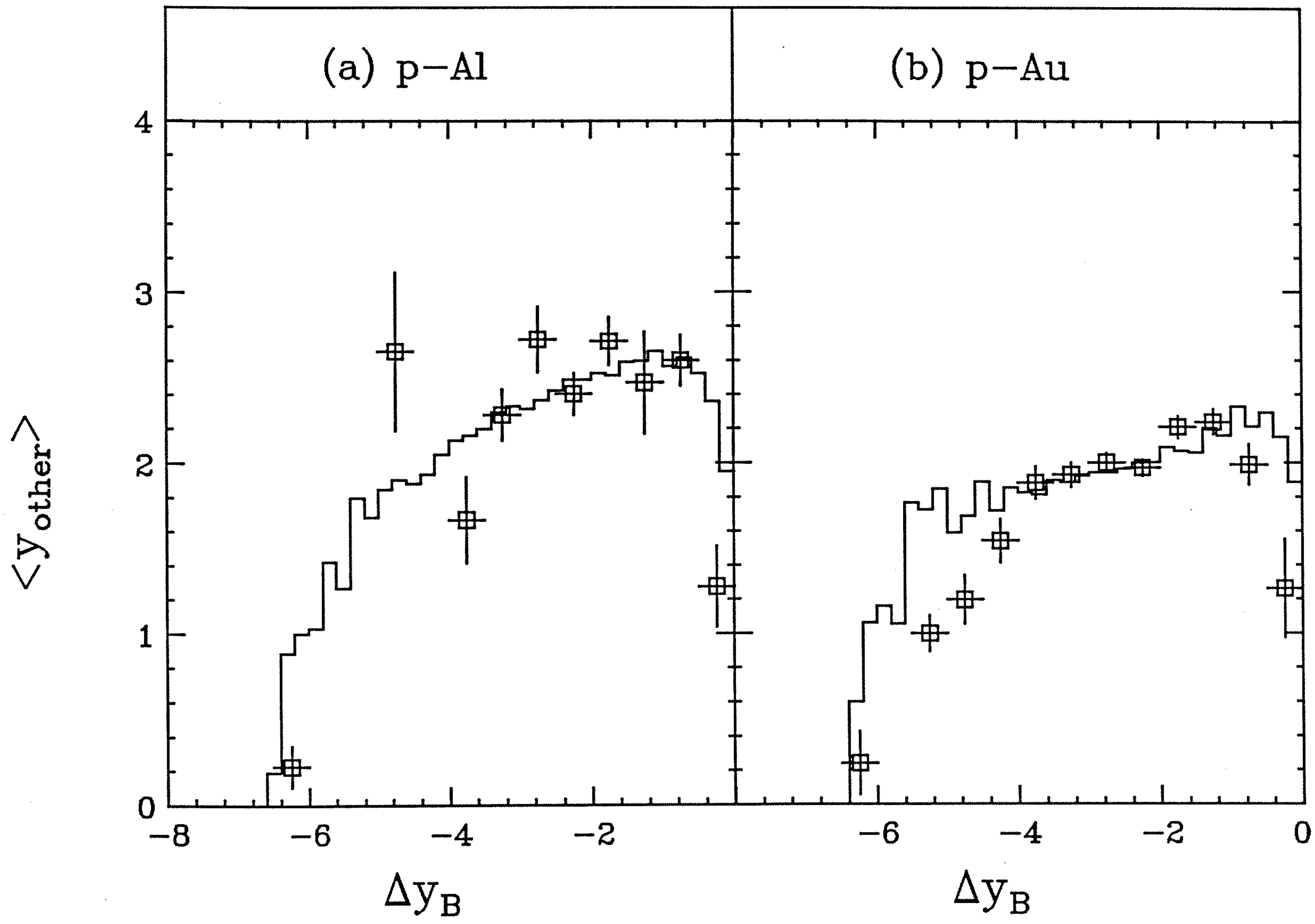

Fig.5−18

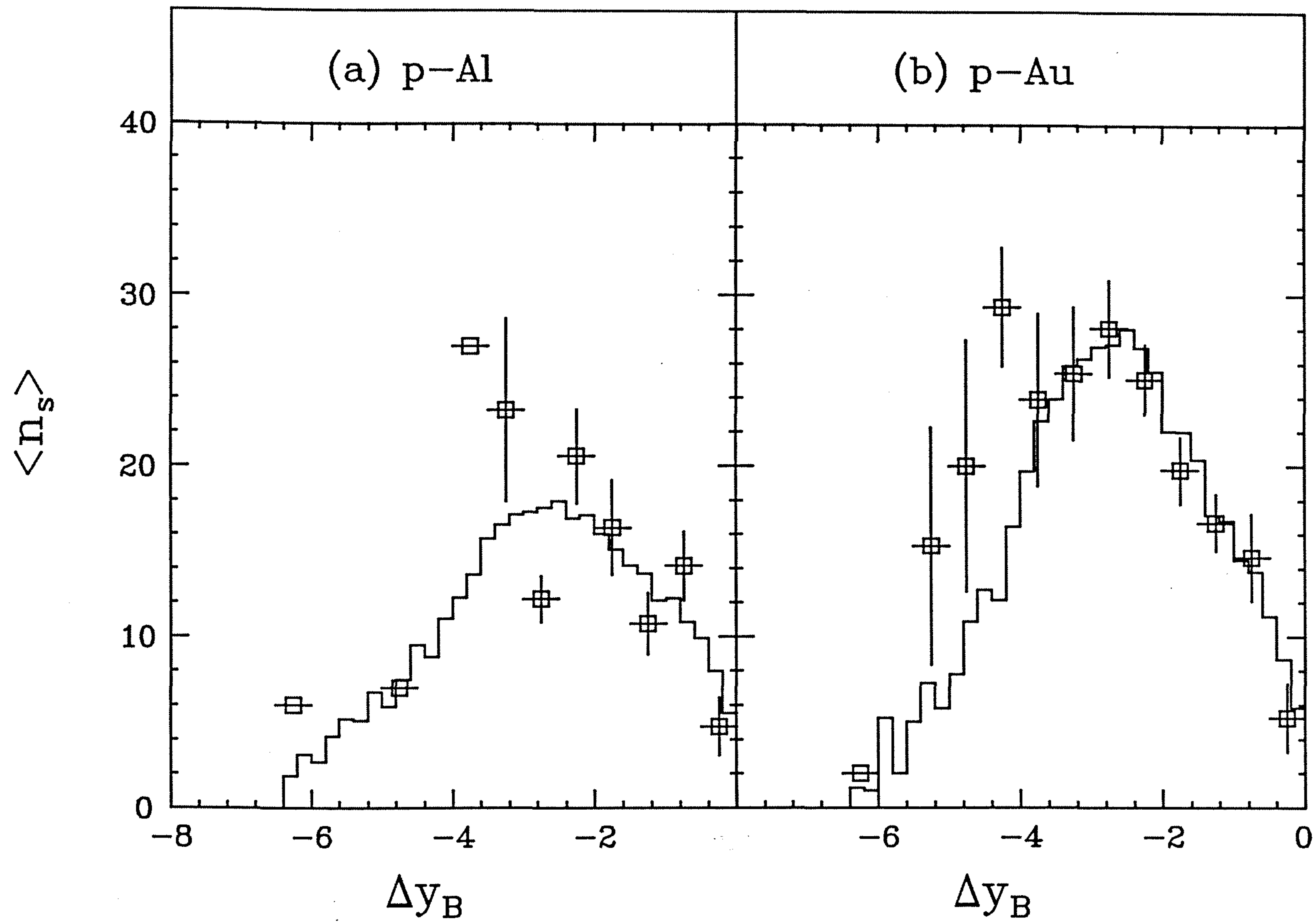

Fig.5−19

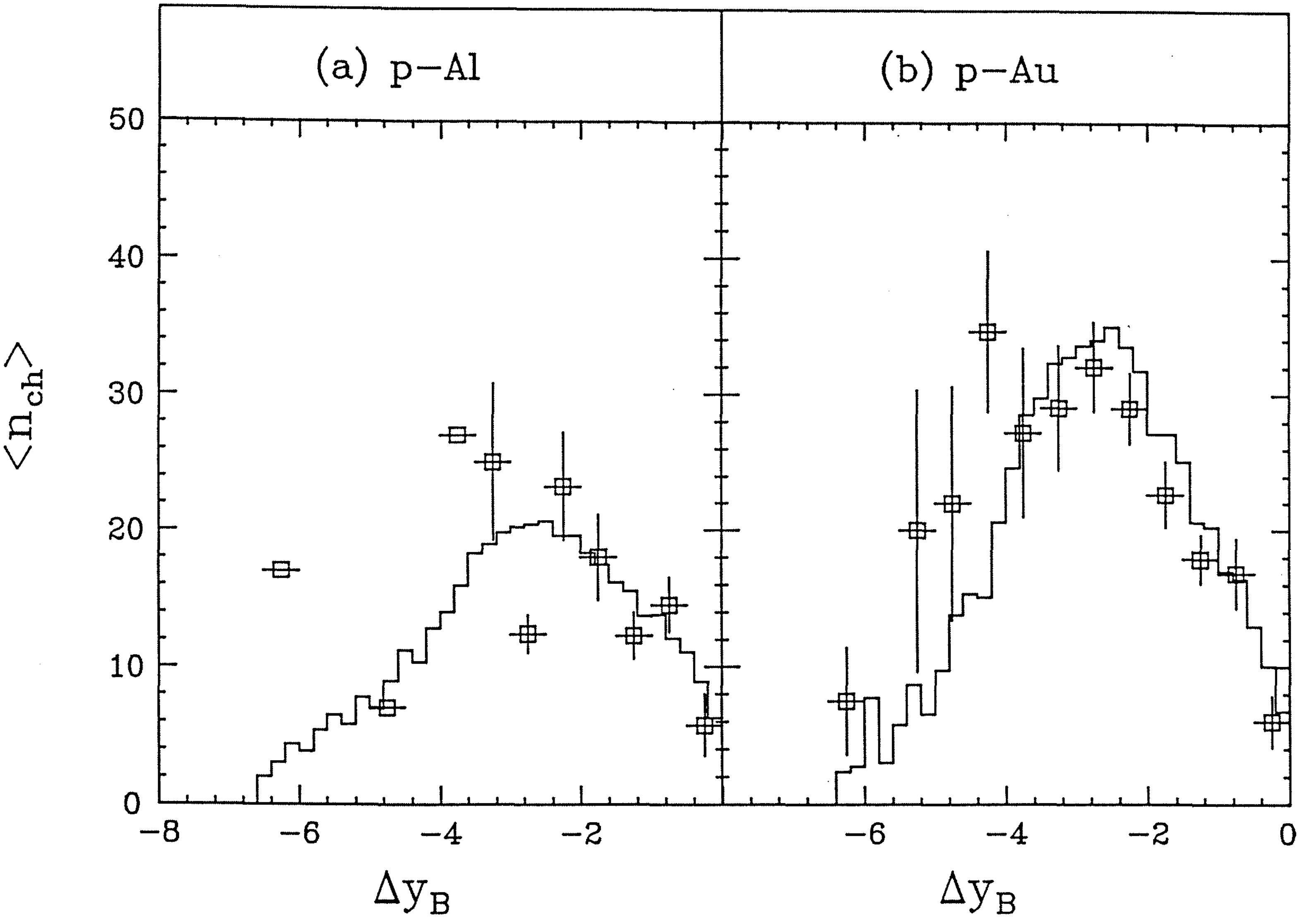
(a) p−Al
(b) p−Au
$\langle n_{ch} \rangle$
50
40
30
20
10
0
−8
−6
−4
−2
0
Δy_B
Δy_B

Fig.5−20

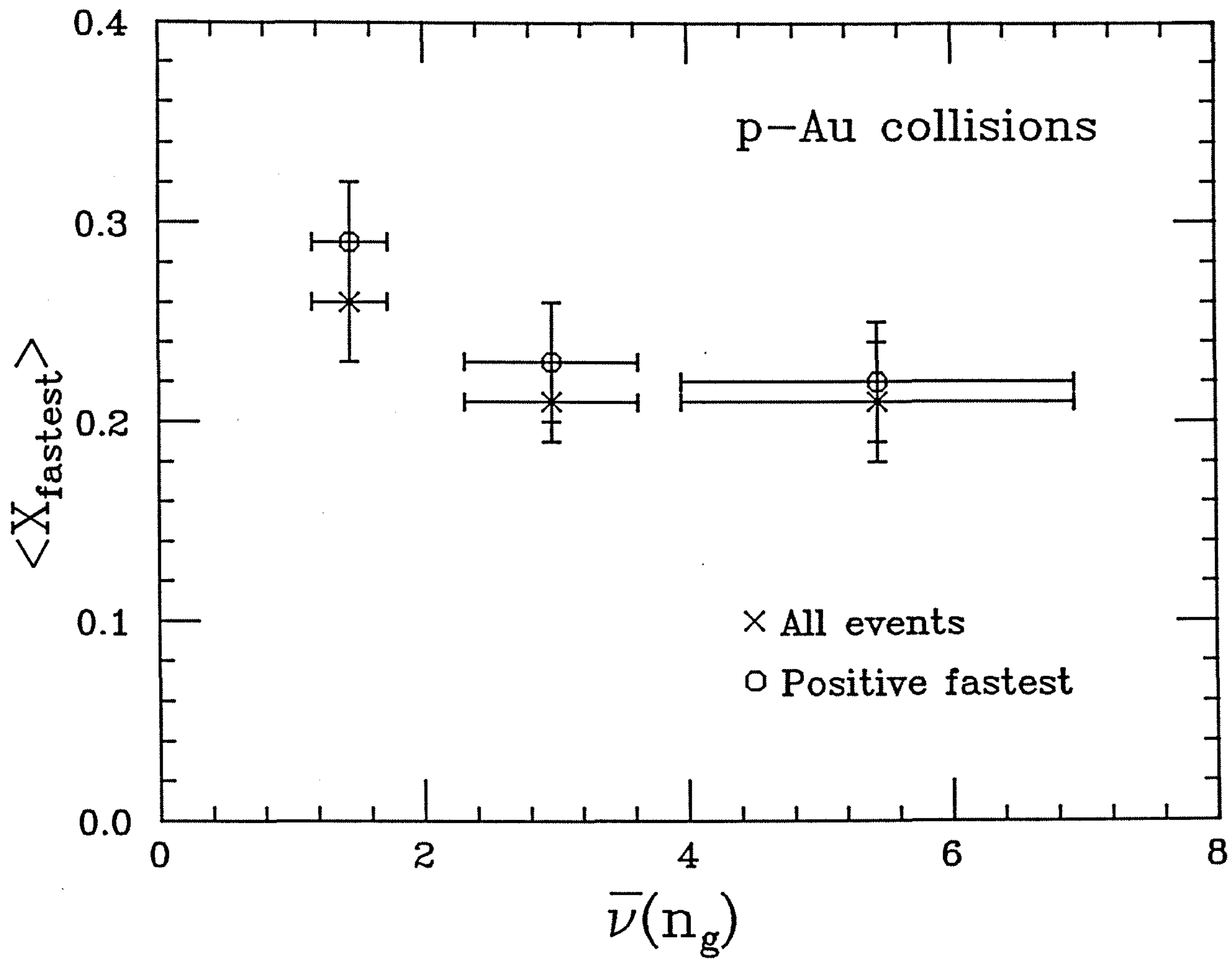
0.4
0.3
0.2
0.1
0.0
0
2
4
6
8
p−Au collisions
× All events
o Positive fastest
<X_fastest>
ν̄(n_g)

Fig.5−21